Study of Excited States in ^{14}C via the ^{4}He(^{10}Be,α)^{10}Be Resonance Scattering Reaction

by

Jonathan Malcolm

A thesis submitted to
The University of Birmingham
for the degree of
Doctor of Philosophy

School of Physics and Astronomy
The University of Birmingham
September 2012

Abstract

A study has been made of the ^{4}He(^{10}Be,α)^{10}Be resonant scattering reaction to explore possible molecular rotation bands in ^{14}C. The experiment was performed at a range of beam energies from 25 to 42 MeV. The recoil particles from the reaction were detected by a set of surface barrier zero degree monitors and two 'lampshade' arrays of silicon strip detectors. A range of new resonances were discovered in the excitation function of ^{14}C between 13 and 24 MeV. Properties of some of these states were identified using angular distribution methods and monte carlo simulations. An R-matrix analysis was performed on the excitation function to provide additional information about the resonances.

Three states, at excitation energies of E_x = 18.8, 19.76 and 20.66 MeV, have been measured and their spins and parities positively determined by angular correlation to be 5^-, 5^- and 6^+ respectively. Two additional states at energies E_x = 17.5 and 17.98 MeV have have had their spins and parities identified by R-matrix analysis to be 3^- and 4^+ respectively.

Acknowledgements

First and foremost I would like to thank my supervisor, Professor Martin Freer. Not only did he allow me the opportunity to undertake my studies for a PhD (a decision he may regret), but he has supported me throughout. Without his continual guidance and his answering of the multitude of inane questions I put forward (despite being the busiest man I have ever known) I very much doubt I would be here today. I thank you very, very much.

Along with Martin there are other staff that have had to put up with my company for the last four years. Garry Tungate, Peter Jones, Victor Ziman (although he luckily escaped), Lee Barnby and Paul Jagpal, I thank you all. A particular mention for Carl and Tzany who not only tolerated me but have become good friends.

A special mention must be made about the two people I have pestered the most over the last few years, Neil Curtis and Nick Ashwood. Not only have they been a massive help but they too have become very good friends. I will miss the fun times we had on experiments, at lunch, climbing and in general.

I have been lucky during my studies and have had the chance to participate in a multitude of different experiments in many countries around the world. During these I have worked with many different people from all over the world. It was a great experience that I will never forget and I thank all of those involved. Whilst studying there have been many other PhD students come and go with whom I have shared an office. They have all become friends and made the time spent in the office enjoyable. In no particular order they are: Peter Haigh, Tom Leadbeater, Tom Munoz-Briton, Simeon Spencer, Tom Burton, Matthew Barr, Joe Walshe, Luke Hanratty, Dan Lambarri and Kit Windows-Yule. Also the basement crew, Richard Powis and Dave Forest whom I could always rely on to keep me company in the pub.

Outside of work there are my friends who have kept me both relaxed and sane. These are: Dave Wooller, Mark Smith, Richard Hanson, James Cox and Richard Jones. You have all been very good friends and I hope you will always continue to be so.

I could not finish without mentioning those people who have contributed the most in getting me to where I am now in my life. My parents have supported me throughout the good and the bad and have always pushed for me to achieve. For their support, not just financially, I will forever be in their debt.

For their financial support I would like to thank the STFC for giving me this wonderful opportunity.

Finally I want to thank my beautiful wife Kym for her love and support. I love you.

To Kym, my love.

Contents

List of Figures

List of Tables

Chapter 1

Introduction

The data and analysis presented in this thesis is part of the continuing study of clustering within nuclei performed by the *Charissa* collaboration. Since the collaboration's inception in 1986 there has been much effort made to analyse the structure of light nuclear isotopes in an endeavour to find evidence of deformation and clustering. In particular, a lot of that effort has gone into the understanding of the cluster structure of the ^{12}C nucleus, especially the Hoyle state [1] and its excitations. As an extension, the current work examines whether the ^{14}C nucleus has an analogous cluster structure, the spins of resonant scattering states in ^{14}C have been determined. In this thesis, resonances in the ^{14}C nucleus were measured by the ^{10}Be + ^{4}He scattering reaction between $E_x = 13$ to 24 MeV.

The *Charissa* collaboration has been studying the effect of clustering on light nuclei for decades and this Chapter discusses some of this previous work and relates it to the current measurements. The following sections introduce the idea of a cluster structure in light nuclei with a review of previous work undertaken by the *Charissa* collaboration.

1.1 History

The structure of matter has been of interest since the Greeks and Indians of 6th Century BCE developed the concept that matter is made from discrete units that cannot be divided endlessly into smaller quantities. Although many theories were produced over the following centuries it was not until the science of chemistry was developed that progress in the understanding of atoms occurred. The French researcher Antoine Lavoisier discovered the law of conservation of mass in 1789 and used it to describe an *element*, something that could not be broken down by methods used in chemistry. Following this, in 1805 the English philosopher John Dalton concluded that elements consisted of a single type of atom that could combine to create molecules and chemical compounds.

In 1897 the physicist J. J. Thomson discovered the electron whilst working on experiments involving cathode rays [2]. He managed to measure the mass of the cathode rays which he measured to be around 1800 times lighter than a hydrogen atom. Thomson determined that all atoms contained electrons in a sea of positive charge, the so called 'plum pudding' model of the atom. It was only two years later that Ernest Rutherford and Paul Villard determined that there were three types of radiation and labeled them alpha, beta and gamma corresponding to increasing levels of penetrability and ionisation potential. In 1909, during the gold scattering experiment, it was determined that the plum pudding model of the atom was incorrect and the Rutherford model was proposed. It was this model which introduced the idea that there was an atomic nucleus within the atom which contained the positive charge and the electrons were in some sort of orbit around the nucleus [3]. In 1920, Rutherford postulated that a neutrally charged particle would be in the nucleus due to the difference in the atomic mass of an atom and its atomic number. It was not until James Chadwick discovered the neutron [4] in 1932 that the two basic building blocks of the nucleus had been determined.

After the discovery of the neutron the nuclear system was generally modeled by treating each nucleon as a single particle in a potential created by the mean interaction of the remaining nuclei. Another approach was to treat certain nuclei as though they were composed of α-cluster subunits [5, 6, 7, 8, 9, 10]. Due to the fact that the α-particle was discovered before the neutron there were already theories in place which postulated that this object was pre-formed before ejection from the nucleus. As early as 1930 there were certain nuclei that had been hypothesised to be constructed of a combination of α-particles [11, 12].

1.2 Clustering in Light Nuclei

Theories, such as the alpha cluster model, suggested that an α-particle could survive in a nucleus due to the α-particle having a very high stability. The binding energy per nucleon of a ^{4}He nucleus is much greater than any of the light nuclei close by in the table of isotopes (Figure 1.1). When combined with the information that the first excited state of an α-particle is at 20.21 MeV it was predicted that α-clusters, once formed, move around inside a nucleus without disintegrating into their constituent nucleons. Indeed the stability of nuclei which have even and equal numbers of protons and neutrons (α-conjugate nuclei, those nuclei that can be decomposed into α-particles), such as ^{4}He, ^{8}Be, ^{12}C and so on, have greater binding energy per nucleon than other isotopes of the same element (Figure 1.2).

The earliest α-cluster models inferred that the ground state of nuclei would exhibit structures that were comprised of geometric arrangements of α-particles. However, experimental results showed that the ground states in most nuclei have a compact nature, generally spherical, and cluster structure is suppressed. In 1968, Ikeda et al.[15] proposed that instead of the cluster configurations being evident in the ground state they would instead manifest at an excitation energy just below the decay threshold of the cluster

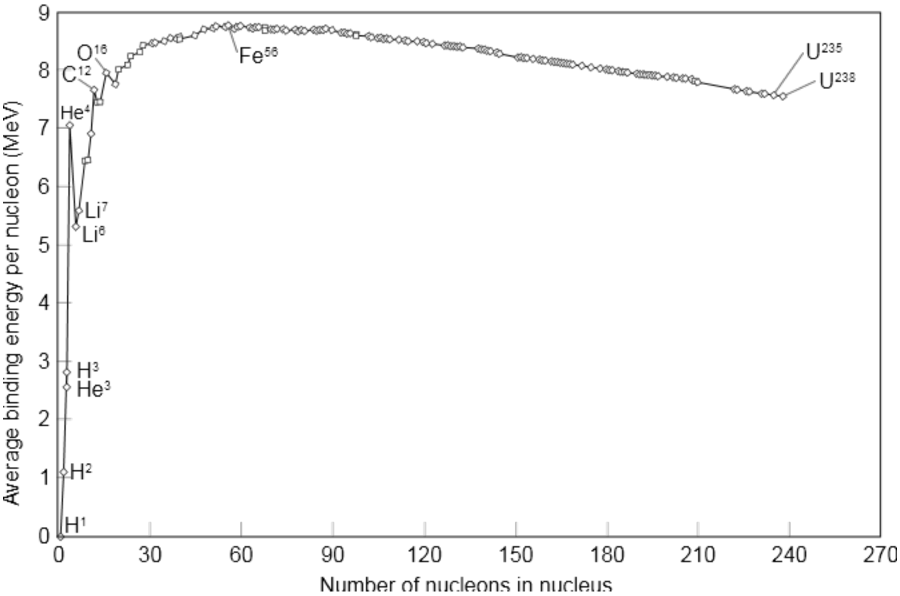

Figure 1.1: The average binding energy per nucleon compared to the number of nucleons in the nucleus. The energy is in MeV. [13]

state [16]. Ikeda proposed that to create the clusters within the nucleus would require energy comparable to the binding energy difference between the core and cluster, and the un-clustered nucleus. Figure 1.3 illustrates for the N = Z nuclei, when N is even, the cluster structures that could arise as the energy of the system approaches the decay threshold for the decay into the constituent component clusters. The theory behind such an arrangement is that as a nucleus acquires energy close to the decay threshold it will adopt a shape that requires the minimum amount of internal rearrangement to eject the cluster. As the excitation energy increases, the structure of the nucleus will change from the spherical ground state to one that comprises of ever increasing number of α-particles.

Physical evidence for Ikeda's theory was available from experiments measuring the total cross-section of the collision between two scattering ^{12}C nuclei. The total cross-section was measured as a function of the beam energy which produced the unexpected result of narrow resonances appearing in the excitation spectrum, shown in Figure 1.4 [18]. The resonances were unexpected as a two nuclei collision should produce a smooth

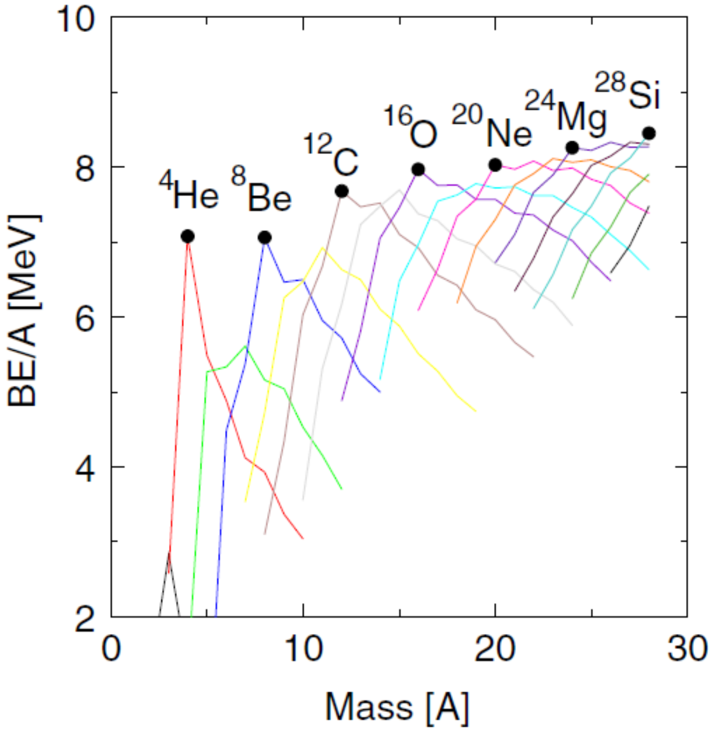

Figure 1.2: Binding energy per nucleon for a range of different isotopes. Note that isotopes which are multiples of α-particles have the highest binding energy per nucleon for that element. From [14].

variation in cross-section as the centre-of-mass energy of the system is increased. When measured the resonances had very narrow widths, typically around 100 keV, which, via the uncertainty principle (Equation 1.1), leads to a interaction time of around 10^{-21} seconds.

$$\Delta E \Delta t \gtrsim \hbar \tag{1.1}$$

The interaction time for a direct scattering process is in the region of 10^{-22} seconds, an order of magnitude less than the interactions observed in the experiments implying that some other mechanism was involved in the interaction. The proposal that was advanced is that the two ^{12}C nuclei were observed in a *molecular resonance* where the two nuclei are in orbit around each other. Further measurements led to the revelation that the ^{24}Mg nucleus exhibited such resonances extending all the way up to 60 MeV [19].

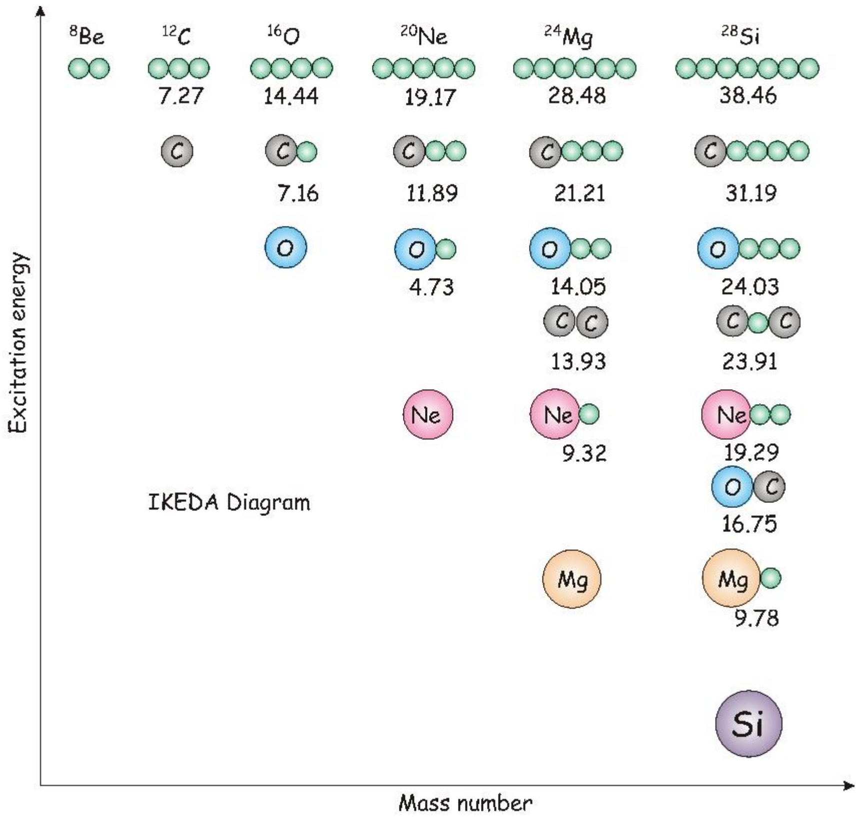

Figure 1.3: The Ikeda diagram [16] which shows the cluster structures and their corresponding threshold energies at which they are predicted to appear. The values stated are in MeV and the diagram is from [17].

The most compelling experimental evidence that supports the theory of a molecular resonance is the fact that a non-spherical body that is under rotation will have greater energy than one that is not. A rotating rigid body will have energy as shown by Equation 1.2, where j is the angular momentum of the body and I is the moment of inertia (from [13]).

$$E = \frac{\hbar^2}{2I} j(j+1) \tag{1.2}$$

In reference to the nuclear case, adding additional rotational energy to the system results in increasing j leading to a series of excited states in the nucleus known as a rotational band. The moment of inertia of the nucleus can be calculated by plotting the

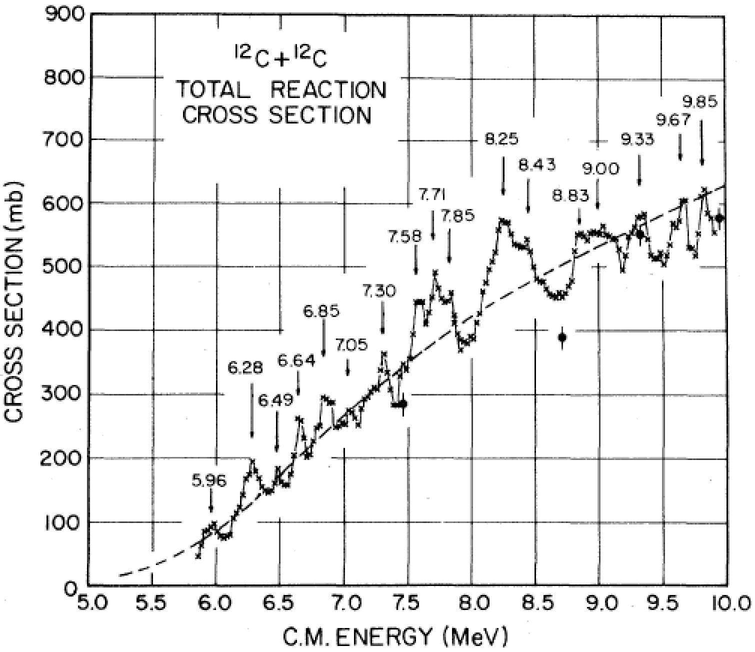

Figure 1.4: Total reaction cross section for $^{12}C+^{12}C$, comparing the cross section in mb to the centre-of-mass energy in MeV. The dashed line represents the theoretical prediction created by an incoming wave boundary condition model. This graph is from [18]

energy of the excited state against *j(j+1)* and measuring the gradient of the curve ($\hbar^2/2I$). In this case a steep gradient correspond to a small moment of inertia, and therefore a small deformation of the nucleus. Conversely, a shallow gradient corresponds to a large moment of inertia and a large deformation.

Cormier [20] measured the spins of the high energy resonances found in the $^{12}C+^{12}C$ scattering experiments and determined that as the energy of the resonances increased so did the spins. Further measurements were performed to ascertain the spins of lower energy states. The results were consistent with the predictions of the moment of inertia for a system in which two ^{12}C nuclei are rotating about each other (Figure 1.5). Experiments, such as those performed by Curtis *et al* [21] on the decay products of the excited ^{24}Mg nucleus via the $^{12}C(^{24}Mg,^{12}C\ ^{12}C)^{12}C$ resonant particle reaction, provided more evidence for the molecular like structure states of the nucleus. In these experiments the excited

^{24}Mg nucleus decayed into two ^{12}C nuclei which were detected in coincidence. The energy and angle of these particles were detected permitting the reconstruction of the energy states within the parent ^{24}Mg nucleus. The results from the analysis of this data provided evidence demonstrating that the break-up states and the scattering resonances were both from the same nuclear excitations. This information implied that molecular resonances had been populated, therefore supporting Ikeda's theory that as the excitation energy of the ^{24}Mg nucleus is increased, it will split into a two ^{12}C clustered state.

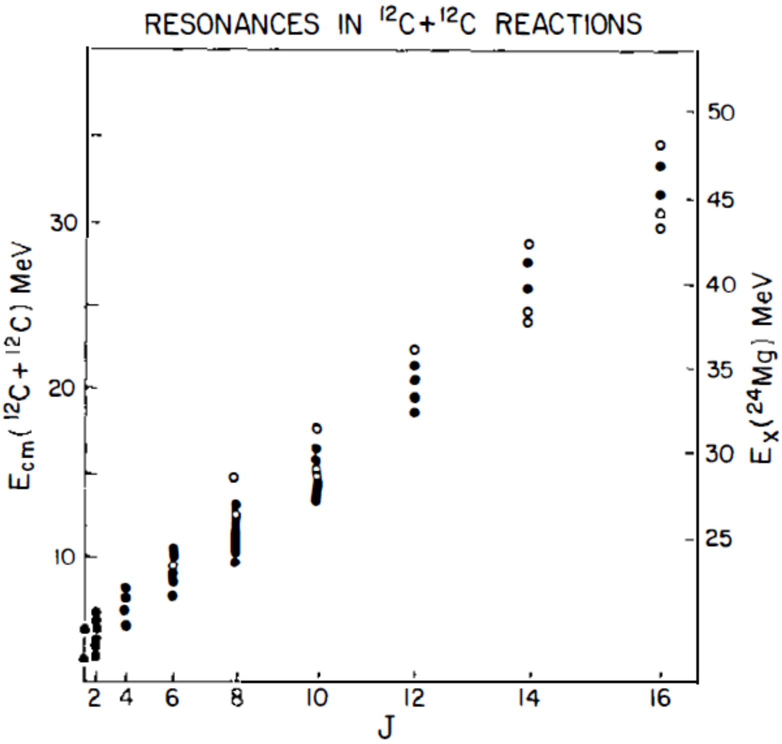

Figure 1.5: The energy spin systematics of the ^{12}C+^{12}C resonances. The higher the excitation energy of a state is the greater the spin of that state. From [20]

While the experiments were being performed various theoretical models were also developed that would help explain the results. Two such models are the Nilsson-Strutinsky method [22] and the Bloch-Brink Alpha Cluster Model (ACM)[23]. The Nilsson-Strutinsky method is a combination containing both macroscopic and microscopic components. The macroscopic element is acquired from the liquid drop model which describes the collective nature of a nucleus undergoing deformation and hence increasing the surface energy of the nucleus. This is combined with a microscopic shell model element which takes into account the single particle energies of each of the individual nucleons. This is in the form of a shell correction.

$$E = E_{LDM} + \Delta E \tag{1.3}$$

where E_{LDM} is the macroscopic part from the LDM and ΔE is the microscopic part from shell corrections. The model uses these effects to create potential energy surface calculations which can be plotted as a function of deformation in the terms of the three shape degrees of freedom (prolate, oblate and octupole). The triangular section and the rectangular box in Figure 1.6 [24, 23] shows the Nilsson-Strutinsky potential energy surface for the ^{24}Mg. The triangular section [24] of the plot shows the potential energy surface of the nucleus under quadrupole deformation, from prolate (γ=0°) to oblate (γ=60°) against the axial deformation ε. The minima that arise in the contour plot are regions of stability and are associated with quasi-stable shapes which the nucleus can take.

Figure 1.6 also displays the results of the calculations made by using the Bloch-Brink α-cluster model [23]. This model assumes that nuclei that consist of $A = 4n$ nucleons are comprised entirely out of α-particles [25], pairs of protons and neutrons that can be represented as 0s states with a total angular momentum of zero. It is possible to determine a wavefunction of a nucleus by calculating the Slater determinant formed by using the spatial part of the wavefunctions for each of the constituent α-particles. To determine the optimal arrangement of the constituents within the nucleus, and thus to minimise the total energy of the system, the α-particle potential widths and locations are varied. Remarkably, Figure 1.6 shows that there is a direct correlation between the shapes predicted by the α-cluster model and the minima in potential surface energy in the Nilsson-Strutinsky model. This shows that the symmetries associated with particular

α-cluster arrangements are also found in Nilsson-Strutinsky calculations. As the two models produce similar results there is evidence that shell structure and clustering are closely linked.

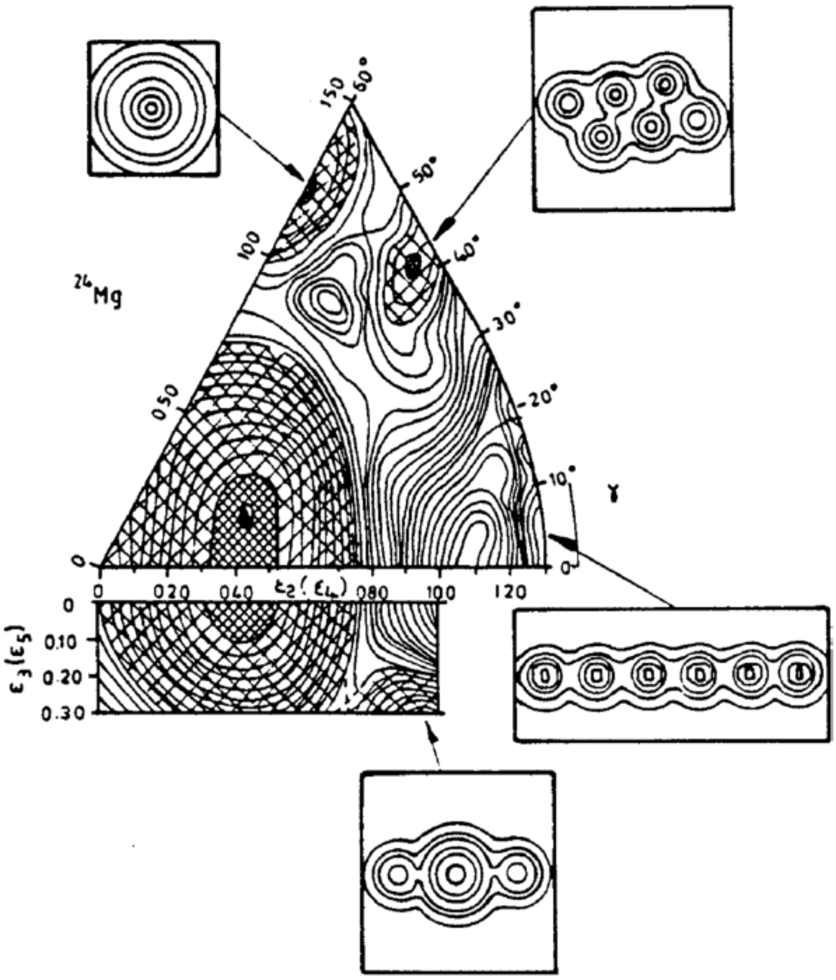

Figure 1.6: Nilsson-Strutinsky and α-cluster model calculations for ^{24}Mg[24, 23]. The triangular section is a contour plot showing the potential energy of ^{24}Mg under quadrupole deformation and the rectangular box below is from under octupole deformation. Around the outside are α-cluster model configurations corresponding to the potential minima in the Nilsson-Strutinsky contour plot. From [26]

The ^{24}Mg nucleus given as an example in Figure 1.6 is just one of many that exhibit the phenomenon of clustering. Indeed calculations have been made using the Nilsson-Strutinsky and the α-cluster models that predict that clustering effects will be exhibited in nuclei up to at least ^{44}Ti [24, 27]. Experimental results have also shown evidence of molecular resonances in the excitation spectra from many other scattering reactions [28], a small collection of these observations is shown in Table 1.1. In this table both the experimentally measured and theoretical calculations for the slopes of the rotational bands are displayed for comparison. The calculations are made assuming that the entrance channel nuclei are in a molecular like state where the nuclei are separated by the sum of their radii. The fact that the experimental data and the calculated values of the rotational band slopes are of good general agreement indicates that many of the collisions in the scattering experiments produce cluster states. More evidence of clustering in nuclei has been found by looking at the excited states of many other heavy nuclei from resonant particle spectroscopy. Yet more evidence of large cluster structures can be found in the resonant particle spectroscopy experiments examining the break-up of ^{28}Si[29, 30] and ^{32}S[31] into ^{12}C+^{16}O and ^{16}O+^{16}O respectively.

Table 1.1: A list of various scattering experiments where the compound nucleus is believed to occupy molecular resonances. The calculated slope is based on classical molecular structures where the two entrance nuclei are separated by the sum of their radii. It is evident that the measured and calculated slopes have a good general agreement indicating that the resonances are based on the entrance nuclei forming molecular states. From [28]

Entrance channel	Composite system	Measured slope of rotational band (keV)	Calculated slope of rotational band (keV)
^{12}C + ^{12}C	^{24}Mg	94.2	69.9
^{12}C + ^{16}O	^{28}Si	65.5	54.2
^{12}C + ^{18}O	^{30}Si	49.2	49.2
^{16}O + ^{16}O	^{32}S	43.3	43.3
^{12}C + ^{24}Mg	^{36}Ar	27.1	38.7
^{16}O + ^{24}Mg	^{40}Ca	30.9	30.9
^{16}O + ^{28}Si	^{44}Ti	27.1	26.7
^{28}Si + ^{28}Si	^{56}Ni	16.7	17.1

Although the earliest experiments to examine cluster structures within nuclei focussed mainly on large clusters within heavy nuclei, there is now a wealth of experimental information pertaining to lighter nuclei. These experiments provide support for the structures proposed in the Ikeda diagram (Figure 1.3) for light, $A = 4n$, nuclei. The most obvious example is that of the light isotope ^{8}Be which has an unbound ground state that is unstable to decay into two α-particles. The rotational behaviour of this state and the measured width reveal that ^{8}Be has an α-α cluster structure [32, 33]. Another well known case is the famous 0^{+} Hoyle state in ^{12}C at 7.65 MeV [34] which can be associated with a triple α cluster state. More recent investigations into ^{12}C have resulted in the potential discovery of both the 2^{+} [1] and 4^{+} [35] states believed to form part of the rotational band for the Hoyle state. In ^{16}O, rotational bands that can be associated with either ^{12}C-α or a 4α cluster configuration, have been discovered [36, 37, 38, 39]. Experimental evidence for the cluster structure of ^{20}Ne is well documented. Multiple experiments have been performed to analyse the composition of ^{20}Ne[40, 41]. These have determined states in ^{20}Ne corresponding to both ^{16}O+α and ^{12}C+^{8}Be clustered structures.

1.3 Molecular Structure and Valence Neutrons

During the mid to late 1990s a number of facilities with the ability to produce radioactive ion beams (RIBs), with great enough intensity to be useful, started to come online. These radioactive beams led to experiments searching for molecular like structures within nuclei, a clustered nucleus that is covalently bound by valence nucleons. Much in the same way that atomic molecules are bound by the sharing of electrons between the atoms, these nuclear clusters are bound by the sharing of nucleons between clusters. It is from the similarity of these two systems that led to the term *nuclear molecules.*

Although the experiments searching for nuclear molecules did not start in earnest until the late 1990s they had been predicted to occur from as early as the 1930s. Hafstad and Teller [9] had created an α-particle model in 1938 which they used to describe the light even-even nuclei, known as $A = 4n$ *saturated nuclei.* The proposed idea was that these nuclei have a binding energy, and hence volume, that is proportional to the number

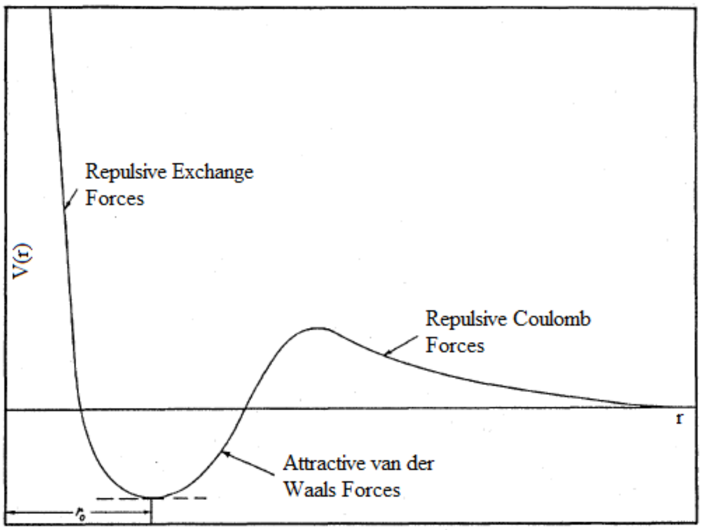

Figure 1.7: The potential that Hafstad and Teller used in their α-cluster model for an interaction between two α-particles[9].

of particles it contains not the square of the number of particles, which is expected if each particle interacts with all other particles. In their model Hafstad and Teller used an α-α interaction potential that combined a short range repulsive force due to exchange forces, a long range repulsive force due to the Coulomb potential and an intermediate attractive potential from *van der Waals* forces. This interaction potential can be seen in Figure 1.7. With these assumptions came the prediction that the α-α interaction potential would maximise the binding energy of the nucleus by confining the α-particles in equilibrium positions. Shapes were predicted for the arrangement of the α-particles that would maximise the binding energy, a dumb-bell arrangement for ^{8}Be, an equilateral triangle for ^{12}C, a tetrahedron for ^{16}O and so on. They then assumed that the binding energy of the system would be proportional to the number of bonds between the α-particles within the nucleus. For example, the ^{8}Be only has one bond between the two α-particles, ^{12}C has three bonds between the α-particles and ^{16}O has six bonds between the α-particles. The actual binding energies of these even-even nuclei matched closely with the predictions made as can be seen in Figure 1.8.

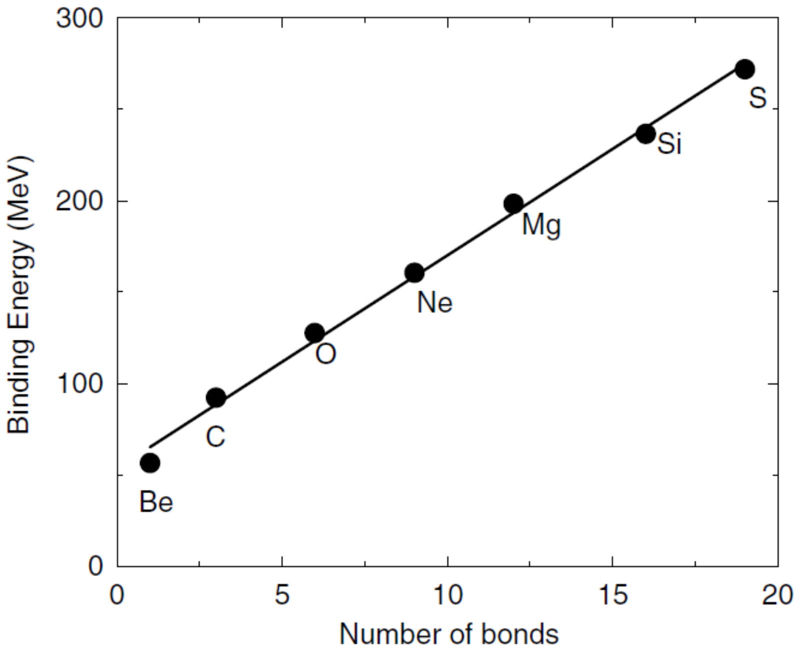

Figure 1.8: Hafstad and Teller postulated that the binding energy of the ground states in A = 4n nuclei is proportional to the number of α-α bonds predicted by their α-cluster model. The graph shows the binding energy in MeV against the number of bonds in the nucleus, ^{8}Be has 1 α-α bond, ^{12}C has 3 bonds, etc. From [14]

Hafstad and Teller then proceeded to extend their model by applying it to nuclear systems that consisted of $A = (4n{+}1)$, for example, nuclei composed of α-particles with an additional neutron (^{5}He, ^{9}Be...). The main assumption made was that the total binding energy of the system would equate to the binding energy of the group of α-particles plus the binding energy of the additional neutron with the α-particle group. The lightest and simplest case to study is that of ^{5}He, a single α-particle with one additional neutron in a p-orbit, as predicted by the independent particle model. When looking at ^{5}He they defined the binding energy of α-particle core with the neutron as B, the mass difference between ^{5}He and its constituent parts, ^{4}He + n. When looking at heavier isotopes it was assumed that the neutron would only interact with one of the α-particles at a time due to the range of the force acting between the α-particles and the neutron being short. Using a quantum mechanical approach for combining wave functions in a linear superposition and determining the lowest energy states, Hafstad and Teller were able to calculate the binding energies of several light, neutron rich, nuclei, for example,

$$\begin{aligned} {}^{5}He - ({}^{4}He + n) &= B, \\ {}^{9}Be - ({}^{8}Be + n) &= B + (R + Q), \\ {}^{13}C - ({}^{12}C + n) &= B + 2(R + Q), \\ {}^{17}O - ({}^{16}O + n) &> B + 3(R + Q) \end{aligned} \tag{1.4}$$

Here the B term refers to the potential and kinetic energy of the neutron due to the α-particle in closest proximity, R is the additional potential energy of the neutron near an α-particle due to the presence of a second α-particle and Q is an exchange term where a neutron at one α-particle can interact simultaneously with two neighbouring α-particles. The assumptions made by Hafstad and Teller agreed very closely with the experimental data that were available at the time, suggesting that they had created a successful α-cluster model that could accurately model the structure of light, even-even nuclei. The model also provided a simple mathematical prediction about the existence of molecular states in nuclei where a neutron is exchanged between α-clusters. The work that Hafstad and Teller performed formed the basis of the interesting field of molecular nuclear physics which can be best demonstrated by the isotopes of beryllium.

As previously mentioned in this chapter, the ^{8}Be nucleus shows a well developed α-α cluster structure [33, 32] and the ground state is unstable to decay into two α-particles. The instability is due to the α-α core repulsion, as a result of the Pauli principle, being greater than the attraction between the α-particles. The addition of a single neutron to create ^{9}Be results in a similar structure, two α-particles and a delocalised neutron which orbits the α-cores. The inclusion of this neutron provides additional binding energy causing the ground state of ^{9}Be to be bound by 1.67 MeV, suggesting that ^{9}Be is composed of two α-particles bound covalently by a valence neutron. The analogy in atomic physics would be the H_2^+ molecule being bound by an electron orbiting in the two centre potential created by the two protons. These principles can not only be applied to higher mass beryllium isotopes but also to neutron rich carbon isotopes (and other α-conjugate nuclei) where the nuclear core is composed of a three α-particle configuration. In this situation the valence neutrons can reside in delocalised orbits around the three α-particles increasing the binding energy and hence the stability of the system. Some of the proposed molecular states that could exist in neutron rich nuclei are shown in Figure 1.9.

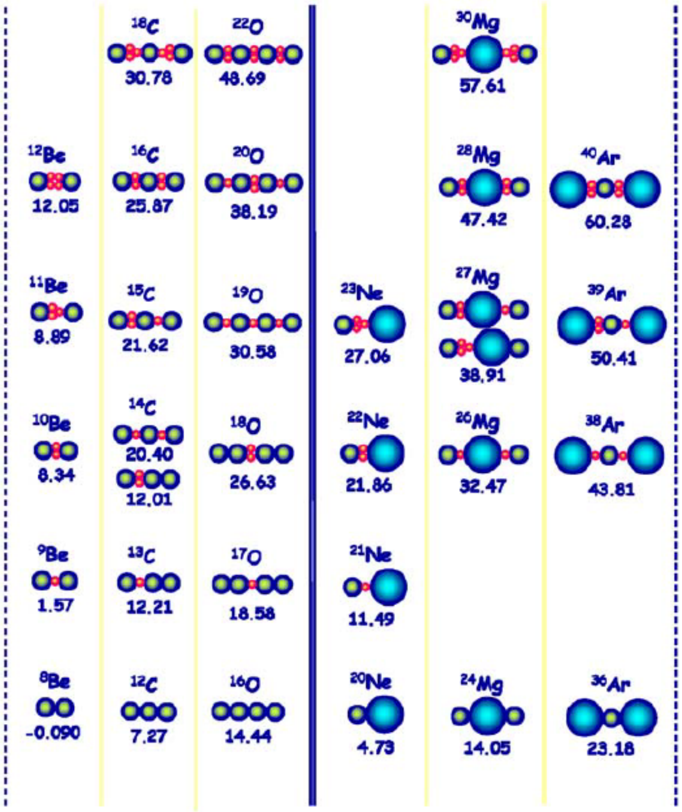

Figure 1.9: An extended Ikeda diagram which illustrates potential molecular structures composed of clusters and valence neutrons. The energies displayed under each figure are in MeV and indicate the threshold for decay into those particular constituents. From [42].

The experimental measurements presented in this thesis were performed to provide additional evidence for the existence of molecular states in ^{14}C.

Chapter 2

Theoretical Details

Due to the experimental evidence of molecular like nuclear structures, much effort has been made to devise models that describe the behaviour of these nuclei. The theoretical models have been used to both reproduce existing experimental results and also in the planning of future experiments. As such, many of the experiments performed by the *Charissa* collaboration have been planned using these predictions. The previous chapter briefly introduced models concerned with clustering in the nucleus and touched on the subject of nuclear molecules. This chapter introduces a more detailed description of theoretical models related to nuclear clustering with a greater emphasis on models concerned with nuclear molecules. At the end of this chapter there is a brief description of the kinematics involved in a two particle resonant scattering reaction and a brief introduction to R-matrix theory.

2.1 Theoretical Models

2.1.1 Deformed Harmonic Oscillator Model

The Harmonic Oscillator (HO) method of describing the nuclear potential is, although unrealistic due to the assumptions made, a good approximation of more sophisticated models. In using the harmonic oscillator model to describe the interactions in a spherically symmetric nuclear system it is assumed that the motion of each nucleon is determined by a parabolic potential. Such a potential is created by the mean interaction of the nucleon with all other constituents in the nucleus. When solving the Schrödinger equation for a three dimensional spherical nucleus the following energy levels are produced,

$$E = \hbar\omega(n + 3/2), \tag{2.1}$$

where n is the number of oscillator quanta and the oscillations can be in any of the three Cartesian co-ordinate axes. If a nucleus is deformed then the potential of the nucleus is also deformed. For example, if the nucleus is elongated along the z-axis the width of the potential in the z-axis is also stretched. To compensate, the potential in the x and y-axes must contract to conserve the nuclear volume. The extension of the potential in the z-direction reduces the oscillation frequency in that direction and, for a potential that is symmetrical about its axes, increases the frequency in the perpendicular direction. This deformation of the potential removes the implicit degeneracy in Equation 2.1 giving rise to new energy levels,

$$E = \hbar\omega_\perp n_\perp + \hbar\omega_z n_z + \frac{3}{2}\hbar\omega_0. \tag{2.2}$$

Here the characteristic oscillator frequencies for oscillations, perpendicular ($\omega_\perp$) and parallel (ω_z) to the deformation axis, are required. The oscillation frequencies are constrained so that $\omega_0 = (2\omega_\perp + \omega_z)/3$ and the quadrupole deformation is given by,

$$\varepsilon = \varepsilon_2 = \frac{(\omega_\perp - \omega_z)}{\omega_0}. \tag{2.3}$$

The overall number of oscillation quanta is the sum total of those on the parallel and perpendicular axes ($n_\perp + n_z$). The calculated energy levels of an axially symmetric deformed harmonic oscillator are shown in Figure 2.1. The numbers in the circles represent the degeneracy of the levels, the number of nucleons (protons or neutrons) that can be placed in the levels at their crossing points. In the case of the spherical harmonic oscillator, where ($\omega_\perp/\omega_z = 1$), the energy of each individual single particle state has a degeneracy which corresponds to the standard shell structure. This provides the normal magic numbers of 2, 8, 20, 28, 50, etc. It is interesting to note here that nuclei which are doubly magic, those where both proton and neutron numbers are equal to a magic number, are especially stable against decay and have a high energy first excited state. Examples are ^{4}He, ^{16}O and ^{40}Ca.

As discussed previously, as deformation is introduced to a nucleus, the degeneracy corresponding to zero deformation is removed. However, when the axial deformation ($\omega_\perp : \omega_z$) is at a ratio of 2:1 and 3:1 the energy levels cross over and regions of high degeneracy occur. These regions of high degeneracy occur at deformations where $\omega_x : \omega_y : \omega_z = a : b : c$ and a, b and c are integer numbers. At these deformations, shell structure is generated along with the corresponding so called *deformed* magic numbers. The magic numbers 4, 10, 16, 28, 40, etc. appear when the deformation ratio is 2:1 (super-deformation), and the numbers 6, 12, 18, 24, 36, etc. at 3:1 deformation (hyper-deformation). Some nuclei can be associated with these *deformed* magic numbers, where the deformation gains the nucleus stability from the additional regions of shell structure.

It has been shown that the magic numbers associated with the 2:1 deformation can be constructed using the spherical magic numbers [44]. For example, 2 + 2 = 4, 2 + 8 = 10, 8 + 8 = 16, etc. In a similar fashion the magic numbers associated with the 3:1 deformation can be fabricated by a combination of three of the spherical magic numbers (2 + 2 + 2 = 6, 2 + 8 + 2 = 12, etc.)[44]. Thus, it has been suggested that each of the magic numbers created as a result of deformation can be linked to a clustered structure. The simplest case to study is ^{8}Be, an isotope linked with the deformed magic number 4

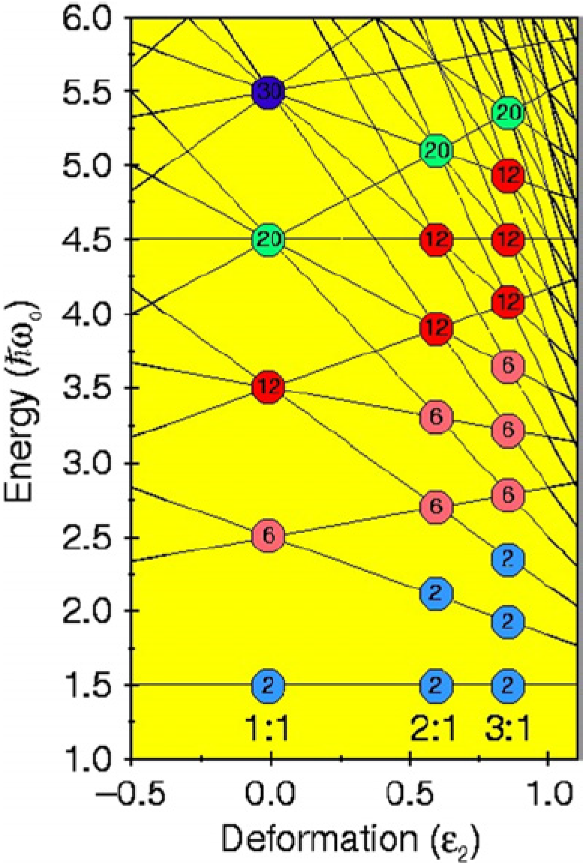

Figure 2.1: Energy levels of the deformed harmonic oscillator plotted as a function of quadrupole deformation. The DHO is deformed axially symmetric. The circled numbers indicate the degeneracy of the energy levels which appear at the crossing of orbitals due to deformation ratios 1:1, 2:1 and 3:1[43].

and, when at an axial deformation of 2:1, this can be expressed as a combination of two spherical magic numbers, 2 + 2. This predicts that ^{8}Be is composed of two α-particles and, available experimental evidence shows good agreement with a super-deformed ^{8}Be ground state [33, 32]. Table 2.1 shows examples of some of the cluster structures that can be associated with the deformed shell gaps and their corresponding magic numbers.

An alternative to looking at the magic numbers is to look at the degeneracies themselves, the numbers in the circles in Figure 2.1. It is clear that the degeneracies 2 ,6, 12, 20, etc. exhibited in the spherical case are repeated at higher deformations. At a deforma-

Table 2.1: A list of various cluster configurations which can be associated with the deformed magic numbers at deformations 2:1 and 3:1. The associated cluster structure for each deformed shell gap is determined by a combination of spherical magic numbers combining to form the relevant deformed magic number[44].

$\omega_\perp : \omega_z = 2{:}1$				$\omega_\perp : \omega_z = 3{:}1$			
Magic numbers at 2:1	Associated nucleus	Spherical magic numbers	Associated cluster configuration	Magic numbers at 3:1	Associated nucleus	Spherical magic numbers	Associated cluster configuration
4	^{8}Be	2 + 2	$\alpha + \alpha$	6	^{12}C	2 + 2 + 2	$\alpha + \alpha + \alpha$
10	^{20}Ne	2 + 8	α + ^{16}O	12	^{24}Mg	2 + 8 + 2	α + ^{16}O + α
16	^{32}S	8 + 8	^{16}O + ^{16}O	18	^{36}S	8 + 2 + 8	^{16}O + α + ^{16}O
28	^{56}Ni	8 + 20	^{16}O + ^{40}Ca	24	^{48}Ar	8 + 8 + 8	^{16}O + ^{16}O + ^{16}O
40	^{80}Zn	20 + 20	^{40}Ca + ^{40}Ca	36	^{72}Kr	8 + 20 + 8	^{16}O + ^{40}Ca + ^{16}O

tion of 2:1 the numbers are repeated twice and at a deformation of 3:1 they are repeated three times. This pattern would indicate that at a deformation ratio of 2:1 the potential of the system is constructed of two interacting spherical harmonic oscillator potentials. Similarly, at a deformation of 3:1 the potential can be assumed to be constructed from three interacting spherical harmonic oscillator potentials.

As the internal binding energy of the α-clusters in the nucleus is high, additional neutrons, which are loosely bound, can be assumed to have little effect on the structure of the nucleus. Thus, the predicted symmetries within the deformed harmonic oscillator will remain, despite the addition of extra neutrons, preserving the α-cluster structure. Hence, a nucleon which is entered into an energy level above a deformed closed shell can be perceived as a nucleon in orbit around a clustered core. This can be regarded as a molecular orbit as the motion of the additional nucleon is dependent on a multi-centered potential.

One method of evaluating these molecular orbits is to use the Hückel approach, constructing the wave-functions from the linear combinations of their multi-centred counterparts (Section 2.1.2). The wave-functions that result from this method are identified in using the same notation as molecular orbital theory, the σ and π nomenclature. These

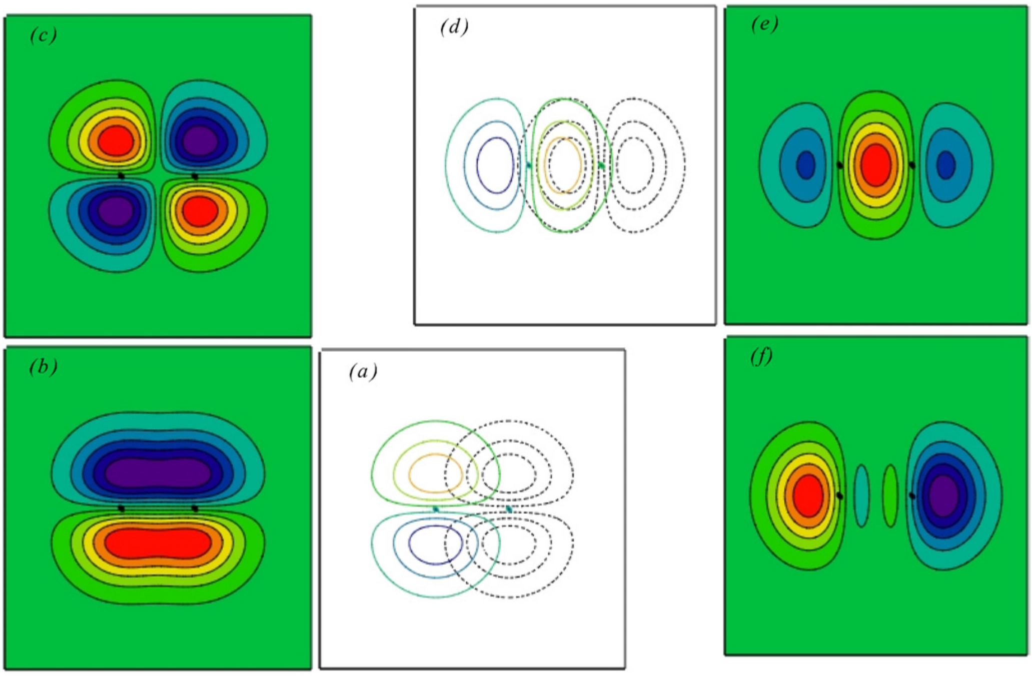

Figure 2.2: The molecular orbitals associated with linear combinations of harmonic oscillator orbitals (n_x,n_y,n_z) = (1,0,0)(left) and (0,0,1)(right) which are equivalent with p-states. The two black dots represent the centres of the potentials and the z-axis is on a line running through both points. Diagram (a) shows the overlap of the two individual wave functions (1,0,0). (b) and (c) are the results of the linear combination of the wave functions which correspond to π binding and anti-binding respectively. Diagram (d) is the overlap of two (0,0,1) wave functions which, when combined, form (e) and (f), σ binding and anti-binding states[45].

notations correspond to the $m_l = 0$ (σ) and $m_l = 1$ (π) angular momentum projections of the molecular orbits onto the symmetry axis of the molecule. This approach requires that the molecular nature of the system being examined is explicitly defined, for example, ^{9}Be is assumed to be a two-centred body consisting of two α-particle cores and a valence neutron. The valence neutron's molecular orbitals can then be constructed by the linear combination of the orbits accessible to the neutron in ^{5}He; i.e. in the harmonic oscillator $(n_x, x_y, n_z) = (1,0,0), (0,1,0)$ and $(0,0,1)$ levels. The density distributions that result from these wave-functions closely resemble those of an electron that binds two ions in a molecular dimer.

Figure 2.2 shows the linear combinations of the (1,0,0) and (0,0,1) HO orbitals in the $z - x$ plane. Within Figure 2.2, (a) displays the overlap of two individual (1,0,0) wave-functions, (b) and (c) demonstrate the linear combinations of these wave-functions which correspond to the π binding state and anti-binding state respectively. Similarly, Figure 2.2(d) illustrates the overlap of two (0,0,1) orbits with (e) and (f) showing the results of the linear combinations of those orbits. Here, (e) corresponds to the σ binding state and (f) relates to the anti-binding state. The last two rows in Figure 2.3 show the π-binding states in both three and four core α-structures, with the lowest energy configurations in the first column. The addition of extra nodes along the centre of the molecule allows for higher energy configurations to be created.

Comparing the density plots created via the Hückel method with the density distributions associated with the harmonic oscillator levels it becomes evident that molecular structures occur in the HO. Figure 2.4 illustrates the density distributions of the harmonic oscillator that can be associated with different energy levels within the deformed HO. At a deformation of 2:1 the first closed shell occurs with an isotope containing four protons and four neutrons, ie. ^{8}Be. Here it can be assumed that the two α-particles that ^{8}Be consists of at this deformation occupy the (0,0,0) and (0,0,1) levels. Adding a neutron to create ^{9}Be requires the neutron to occupy the next available level which is either (1,0,0) degenerate with (0,1,0) or (0,0,2), levels that contain certain symmetries with the molecular orbits (b) π and (e) σ in Figure 2.2. It can therefore be assumed that these two energy levels in the deformed harmonic oscillator contain a molecular character. If considering all linear α structures the next available levels for an additional neutron are the degenerate (1,0,0) and (0,1,0) levels, associated with π-type structures (the first column in Figure 2.3). Hence, the lowest energy molecular state would be that of π-type neutrons in a delocalised region along the entire α-chain.

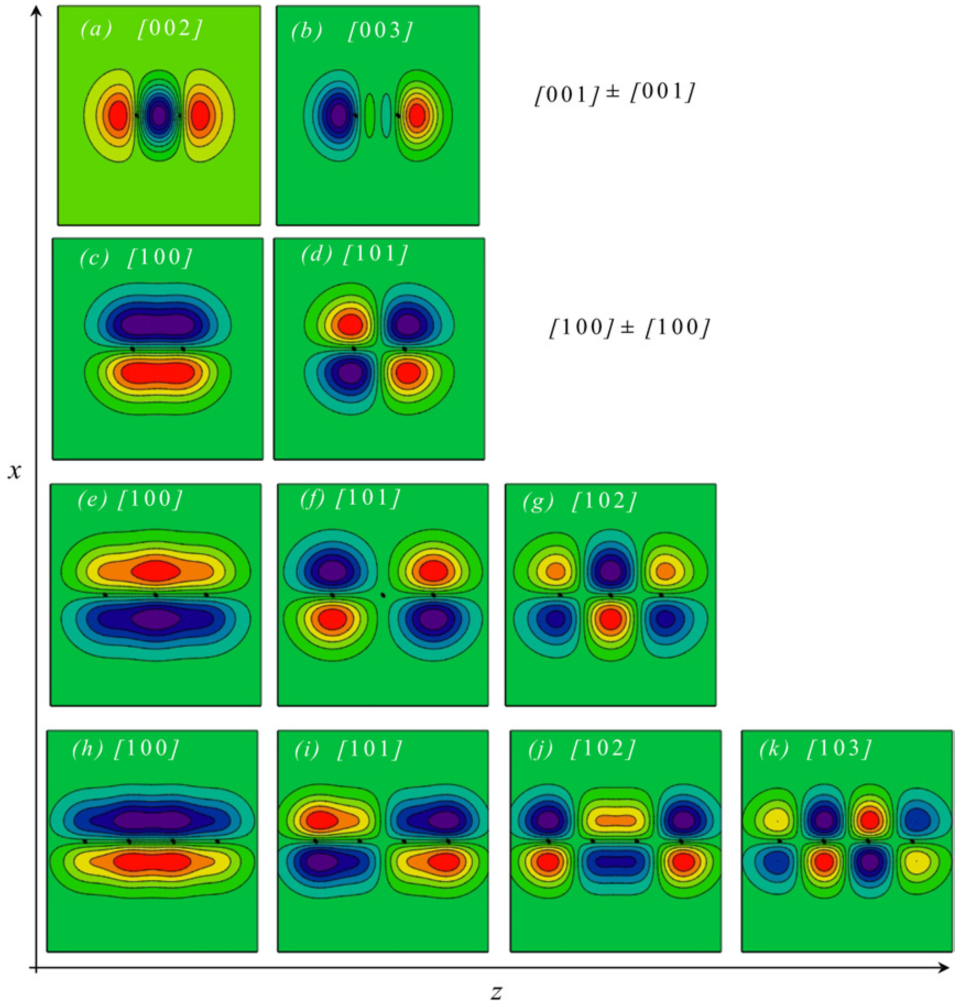

Figure 2.3: Hückel method calculations have provided this series of contour plots of the densities of valence neutrons in a set of chain like α-particle configurations. (a) to (d) are two centred, (e) to (g) are three centred and (h) to (k) are four centred systems respectively. In all cases the black dots represent the positions of the α-particles. All plots show the linear combination of the (1,0,0) orbits yielding π-configurations with the exception of plots (a) and (b) which display the linear combination of (1,0,0) HO orbits. The label in each diagram refers to the DHO level with which each molecular orbit corresponds[46].

2.1.2 Nuclear Molecular Orbital Model

Molecular orbital theory is used in chemistry to describe the behaviour of electrons as they move in potentials created by the underpinning atoms. The most common representation of the molecular orbital is as a linear combination of atomic orbitals (LCAO). The method

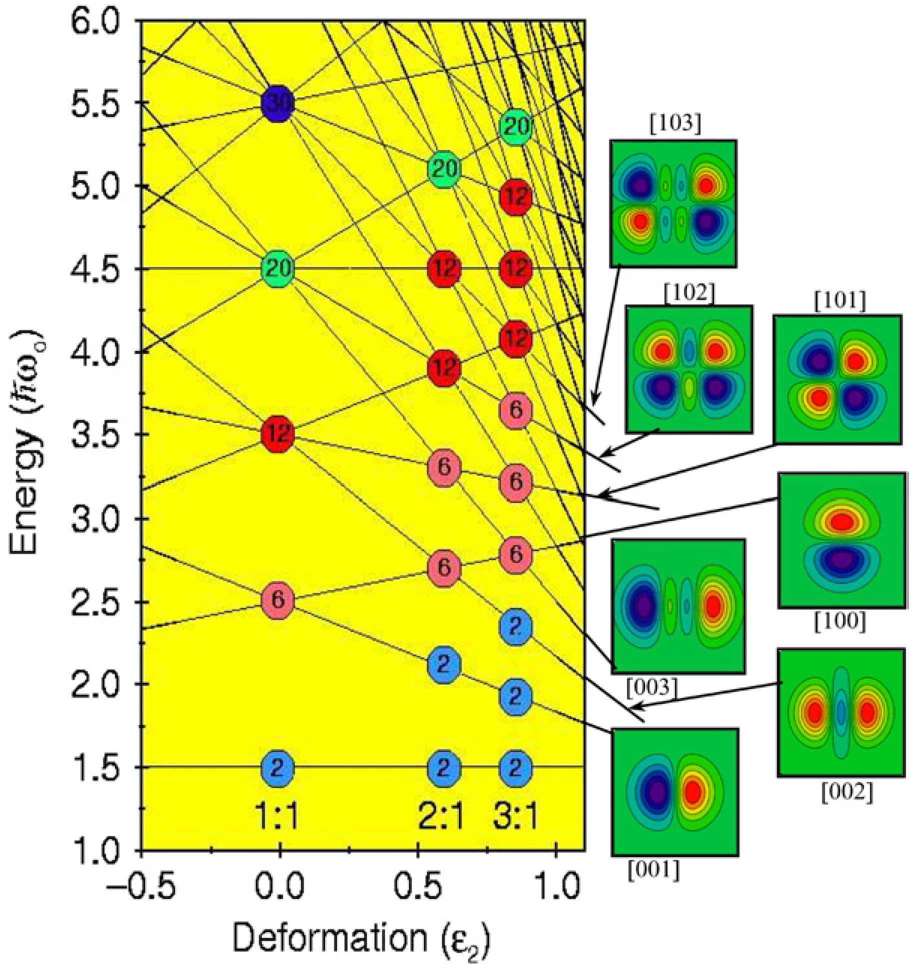

Figure 2.4: The energy levels of the deformed harmonic oscillator compared with the densities of the harmonic oscillator wave-functions for various levels. The plots indicate the molecular nature of the HO levels as there is a strong overlap between the contour plots and those produced by the Hückel method (Figures 2.2 and 2.3)[46].

is simple but it provides an excellent method to describe the role that electrons play in molecular bonding and is indeed the approach characterised by the Hückel method.

The model can be adapted to examine nuclear systems that have a well defined cluster structure combined with valence neutrons. A potential is defined that accommodates the multi-centred structure of the nucleus and contains terms related to the interaction between the cores and valence particles and also the spin-orbit interaction. As with electrons in atomic molecules the valence particles are assumed to move freely in the multi-centred potential created by the multiple cores. The molecular orbitals can then be constructed by the linear combination of nuclear cluster orbitals (LCNO).

Itagaki *et al.* have applied this method to neutron-rich nuclei and have performed extensive studies on beryllium dimers [47, 48, 49] and on chain-like [50, 51] and linear carbon isotopes [52].

2.1.3 Antisymmetrised Molecular Dynamics Model

The Antisymmetrised Molecular Dynamics (AMD) approach, on which a comprehensive review has been completed by Kanada-En'yo and Horiuchi [53], is another method which reveals nuclear clustering and nuclear molecules. It has many advantages over other microscopic cluster models, the greatest being that it does not make assumptions about clusters or relative co-ordinates between clusters, due to the AMD model being based upon the nucleon wave functions.

The AMD wave-function of an A-nucleon system is antisymmetrised via the Slater determinant,

$$\Phi_{AMD}(Z) = \frac{1}{\sqrt{A!}}\mathcal{A}\{\varphi_1, \varphi_2, ..., \varphi_A\}, \tag{2.4}$$

where $\mathcal{A}$ is the antisymmetrisation operator and φ_i are the Gaussian single-particle wave functions described by,

$$\varphi_i = \phi_{X_i}\chi_i\tau_i. \tag{2.5}$$

Here, ϕ_{X_i} is the position in space, χ_i is the intrinsic spin and τ_i is the isospin function of the i^{th} single particle state. The wave-function Φ_{AMD} is parameterized by Z, a set of variables used to describe the spin and geometry of the combined wave-function constructed by the combination of the Gaussian wave packets of individual particles.

By constraining the wave-function, Φ_{AMD}(Z), the minimum energy state of the system can be calculated by varying the spacial locations of the centres of the Gaussian wave-packets. One such constraint that can be applied to the system is the magnitude of the orbital angular momentum. As previously mentioned the AMD model does not rely upon any model assumptions, hence any clustering effects produced by the model are more convincing than other cluster based models.

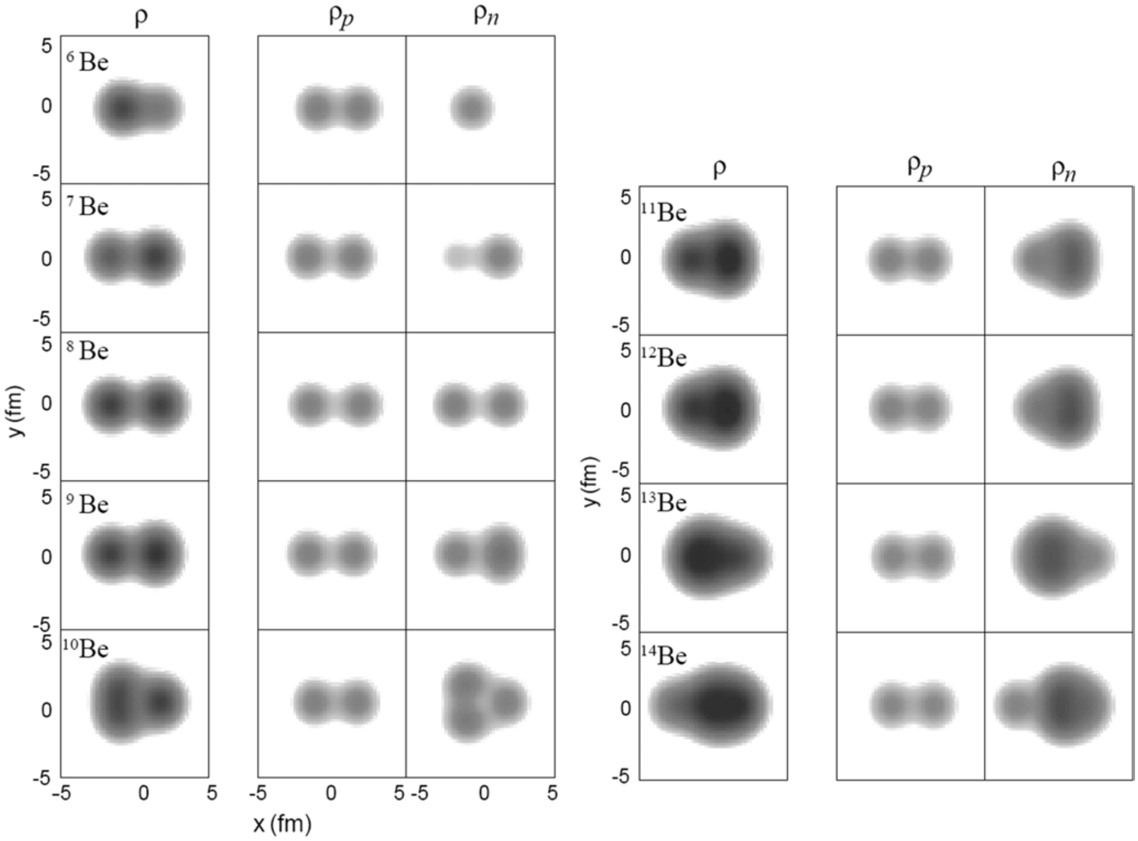

Figure 2.5: AMD calculated density distributions for the ground states of beryllium isotopes. The first column is the total nucleon density, the second and third columns are the proton and neutron densities respectively, from [53].

The AMD approach has been used to model many isotopes, mainly light nuclei, especially those of lithium, beryllium, boron and carbon. The AMD model, in general, reproduces experimental results for the excitation energies, moments, radii and transition rates for these nuclei. Figure 2.5 illustrates the clusters that appear from the nucleon-nucleon interaction within AMD for isotopes $^{6-14}$Be. The figure shows the ground state density distribution of the beryllium isotopes by displaying the overall nucleon density along with the proton and neutron densities. The shapes of the density distributions for the protons clearly demonstrates that each of the beryllium isotopes has a prolate cluster structure. Careful examination of the proton densities reveals that the separation between the proton cores is maximum when the proton and neutron numbers are equal, ie. for ^{8}Be. Furthermore, when the density distribution of the neutrons is more spherical the separation between the proton cores is reduced. Thus the role of neutrons in the nucleus is evident and the AMD calculations can accurately reproduce the ground states of ^{8}Be and ^{9}Be, with $\alpha - \alpha$ and $\alpha - \alpha - n$ structures. ^{10}Be has had detailed AMD calculations performed on the ground state structure of the isotope executed by Kanada-En'yo *et al.* [54, 55].

2.2 Molecular Configurations in ^{14}C

The examples provided in the theory section consider the relatively simple structure of the beryllium isotopes, a clustered state of two alpha particles with valence neutrons. The success of these theoretical models leads to possibility of clustered states created from a three α-particle core, the carbon isotopes. These isotopes could be considered to be beryllium dimers with an additional α-particle. Hence, the molecular structure for ^{9}Be can be used to make predictions about the α-cluster structure of ^{13}C. Similar predictions can be deduced for ^{14}C by examining the molecular properties of ^{10}Be and extrapolating.

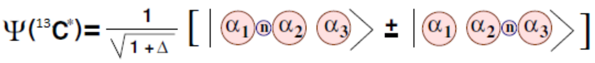

Figure 2.6: Combination of wave functions in ^{13}C due to the asymmetry caused by the valence neutron[56].

Any cluster structure produced in ^{13}C by the three alpha particles and an additional neutron will, intrinsically, be asymmetric. Due to this asymmetry, the overall wave-function of the molecular nucleus will be a combination of wave-functions (see Figure 2.6). This asymmetry causes two molecular bands to arise, one positive parity and one negative parity. As previously stated the molecular structure of ^{13}C is based upon the ground state of ^{9}Be which gives rise to two rotational bands built upon the $3/2^{+}$ and $3/2^{-}$ spin and parity band-head states. Milin and von Oertzen *et al.* performed an extensive analysis of ^{13}C in which they produced a complete spectrum of states [57]. The method they utilised eliminated all the states associated with the single-particle shell model and those remaining were assigned to rotational bands. The properties and population characteristics of the remaining states determined which molecular rotation band they were assigned to. Figures 2.7 and 2.8 indicate the two molecular bands built upon the $3/2^{+}$ and $3/2^{-}$ states. The energy of the lowest state in each of the two molecular bands, or band-heads, correspond with the energies predicted by the three centre molecular orbital model. Similarly, the magnitude of the energy gap between the two bands due to the parity splitting is as predicted. Both of the molecular bands are found to have a large moment of inertia which is consistent with that of a linear chain structure. The reasoning and evidence behind why the band-heads should have J = 3/2 is explored below.

Although the 9.897 MeV $3/2^{-}$ state lies around 5 MeV above the neutron decay threshold it has a surprisingly narrow width, $\mathit{\Gamma} \sim 26$ keV. This would indicate that some mechanism is making this neutron radioactivity mode structurally unfavourable, the daughter state in ^{12}C has a well known shell-model like structure whereas the state in ^{13}C is potentially clustered. As there are no other states within 400 keV of the 9.897 MeV state [58] the spin is assigned with some certainty and since the differential cross-sections for the population of the state are easily obtained. The addition of a neutron to a compact ground state nucleus such as ^{12}C will generally only populate shell-model type states. Hence, if the 9.897 MeV state has a clustered structure then a single nucleon transfer reaction would not be expected to strongly populate the state. This has been

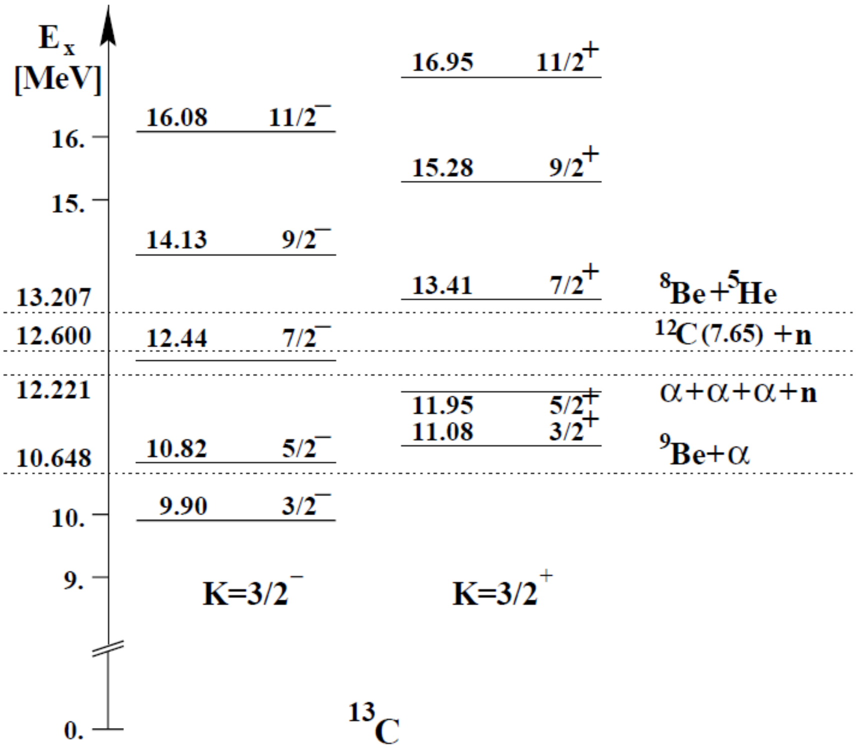

Figure 2.7: These are states in ^{13}C which are proposed to be members of the two rotation bands built upon the $K^{\pi} = 3/2^{-}$ and $3/2^{+}$ band-heads. Shown along side are the decay thresholds into various components of ^{13}C, from [57].

experimentally confirmed [59, 60, 61, 62]. However, the 9.897 MeV state is prominent in two and three neutron reactions [60, 63, 64, 65, 66, 67] and the state is strongly populated by α-transfer reactions [68], which are expected to populate clustered states strongly. Experimental evidence for the reaction ^{9}Be + $\alpha \rightarrow$ ^{13}C shows that the spectroscopic strength is three orders of magnitude [68, 69] greater than predictions made on 1p shell calculations [70]. Further indications that the 9.897 MeV state does not have a spherical shell model like character are that proton [71, 72], electron [73, 74], ^{3}He and α [75] inelastic scattering measurements only weakly populate the state. These arguments, along with the vicinity of the state to the threshold for decay into ^{9}Be + α and ^{12}C[0_2^+] + n, indicate that the 9.897 MeV state has a well defined cluster structure.

The state lying at 11.080 MeV is the proposed $3/2^{+}$ band-head which again lies close

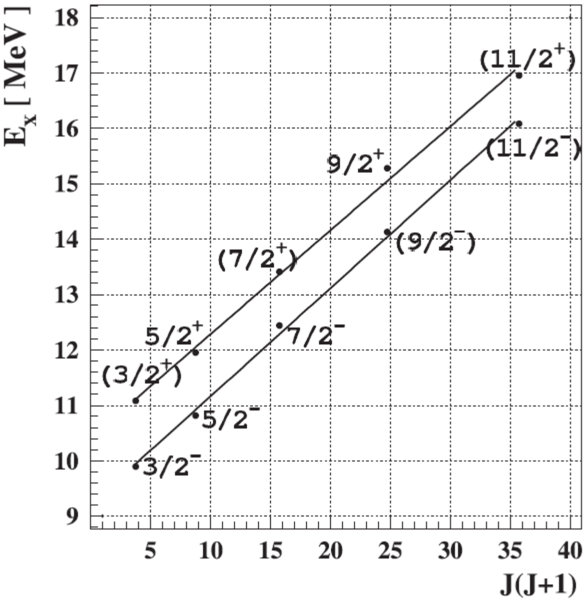

Figure 2.8: The two parity molecular bands in ^{13}C. Here the energy of the state is plotted against the spin of the state. The strong correlation indicates a molecular like structure. From [57].

to both the ^{9}Be + α (10.648 MeV) and ^{12}C[0^+_2] + n (12.600 MeV) decay thresholds. The proximity of the state to the ^{12}C[0^+_2] + n threshold is deemed to be important as it is believed that the second 0^+ of ^{12}C has a structure resembling a three alpha chain that is bent, or slightly angled. Similarly to the $3/2^-$ band-head, the $3/2^+$ state has a very small width, around 4 keV, and is weakly populated by one nucleon transfer reactions [60, 61, 62] but strongly populated in two and three nucleon transfer reactions [60, 63, 64, 66, 67]. This indicates a very small overlap with the shell-like structure of ^{12}C. The population of the state is seen very strongly in the ^{7}Li(^{9}Be,^{13}C→ α+^{9}Be)t breakup reaction [76] but is only weakly populated via proton [71, 72], electron [73, 74], ^{3}He and α inelastic scattering [75]. The most conclusive evidence that the 11.080 MeV $3/2^+$ state exhibits a ^{9}Be+α cluster structure is that in measurements of the ^{9}Be$(\alpha, n)^{12}$C reaction the state appears as a very strong and sharp resonance. The evidence provided indicates that the 11.080 state does indeed have a well defined cluster structure and is the obvious choice as the

$3/2^+$ band-head.

The ^{9}Be$(\alpha, n)^{12}$C reaction also provides evidence for the excited states in both of the molecular bands as all of those states are populated by the reaction. Furthermore, this reaction does not strongly populate any other state apart from the 10.0996 MeV state. The ^{9}Be$(\alpha, \alpha)^9$Be reaction also provides similar results along with α-transfer reactions. It is from this evidence that we can deduce that all of the states in the proposed molecular bands likely consist of a ^{9}Be+α or 3α+n cluster structure.

For the molecular states in ^{14}C there are three predicted configurations, two prolate and one oblate, based upon the ^{10}Be+α and ^{13}C+n structures [56, 42]. These predicted structures can be seen displayed in Figure 2.9. The first arrangement in the figure (a) corresponds to the $\alpha - n - \alpha - n - \alpha$ chain like structure which is intrinsically symmetric as the neutrons are equally spaced between the α-particles. In the symmetrical chain like structure the valence neutron density distributions will differ depending on the type of bonding, π or σ-bonds. In the situation where π-bonds are formed the density distributions will be outside of the axis of symmetry, the opposite is true for σ-bonds [57, 56]. It is also possible that a combination of the two bond types can exist [50]. It is expected that the band-head for the π-state configuration exists below the 3α+$2n$ decay threshold due to the additional binding effect created by the two valence neutrons. Alternatively, the two valence neutrons can both be positioned between the same two α-particles (Figure 2.9b) creating an intrinsically asymmetric configuration, $\alpha - 2n - \alpha - \alpha$, causing a gain in binding energy due to the n-n pairing energy. As with the asymmetric configuration in ^{13}C, this asymmetry will cause a parity inversion doublet, the band-heads are believed to exist below the decay threshold for ^{10}Be+α (12.01 MeV). Figure 2.9c demonstrates the possible oblate cluster structures that could exist based upon a triangular configuration of the α-particles. In this configuration the valence neutrons are in σ-bonds between the α-particle cores. In the oblate structure, π-bonds would penetrate the α-particles and as such are thought to be hindered by the Pauli principle [57]. There have been discussions [46] about the valence neutrons occupying a delocalised posistion above and below the α-particle plane.

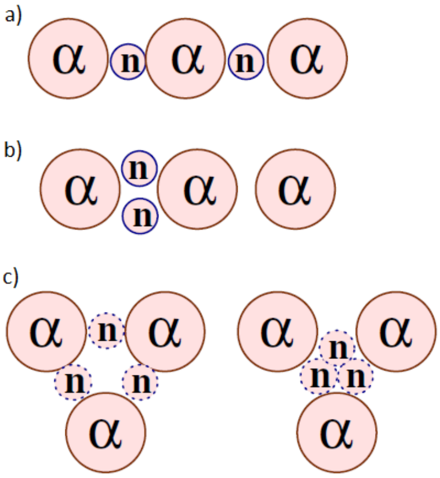

Figure 2.9: A schematic diagram of the possible molecular configurations of ^{14}C. In the triangular configurations the two valence neutrons can occupy two out of the three possible locations [56].

A complete spectroscopic analysis has been performed on ^{14}C [56] which resulted in four molecular rotational bands, shown in Figure 2.10, being proposed. Two of the rotational bands correspond to an oblate structure, built upon a 0^+ and 3^- band-heads, whilst the other two bands correspond to the parity split doublet built upon 0^+ and 0^- band-heads. However, some of the properties of the states within the molecular bands, such as total and partial widths, are unknown. Hence, the present experiment performed for this thesis is aimed at improving our understanding of the resonant states above the ^{10}Be+α decay threshold.

2.3 Thick Target Inverse Kinematics Reactions

During the early 1990s the Thick Target Inverse Kinematics (TTIK) technique was developed to improve the efficiency of experiments exploring the excitation functions of

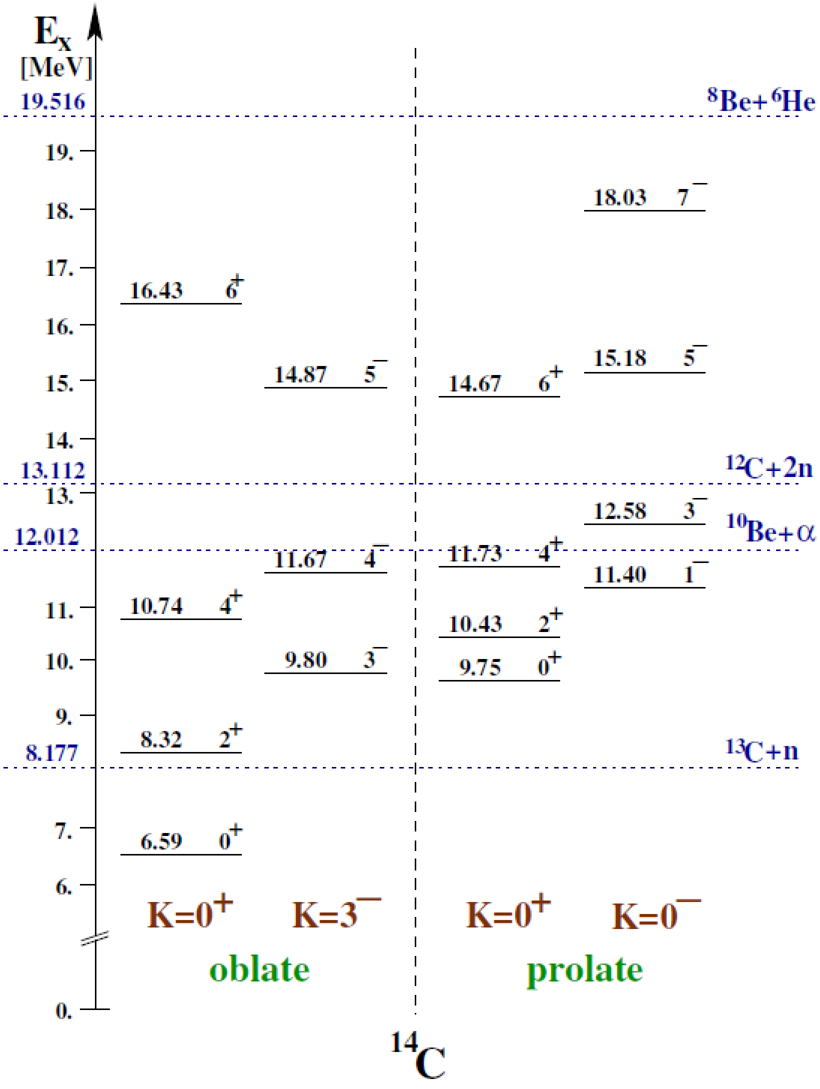

Figure 2.10: The energy level scheme for those levels in ^{14}C which are proposed to form rotational bands. The two oblate bands are built upon the $K^\pi = 0^+$ and 3^- band-heads. The two prolate bands are proposed to lie on the $K^\pi = 0^+$ and 0^- band-heads. The decay thresholds for the decay of ^{14}C into various components is also shown. From [56].

resonant elastic scattering reactions [77, 78]. Normally excitation functions are built up over many measurements by accelerating a light beam into a heavy target, and varying the beam energy (heavy and light referring to the relative masses not the absolute masses of the particles). However, this is very time consuming as each beam energy will provide only one data point in a function therefore many beam energies are required to build a complete picture. Conversely, using a heavy beam and a light target, it is possible to measure a range of excitation energies with only one beam energy. A description of the main principles of TTIK including the techniques advantages and disadvantages follows.

The beam of heavy ions enters the reaction chamber filled with a target gas, usually helium, whereupon it will start to decelerate due to the loss of energy via ionisation of the gas (Section 4.2). The pressure of the gas inside the chamber is large enough to bring the ions in the beam to a complete stop. Hence, the gas in the chamber acts not only as the α-target but also the beam moderator and absorber. When an interaction, elastic scattering for example, occurs between an ion from the beam and the nucleus of the target gas then the light recoil gas particle will gain kinetic energy. As the lighter particle will lose less energy via collisions in the gas it will travel further through the gas and can be picked up by detectors. In addition to the elastic scattering, any resonances in the compound nucleus will produce a peak in the excitation function and, as the beam is slowing down in the gas, a range of excitation energies can be scanned with a single beam energy. It is this scanning that is the greatest advantage of the TTIK technique. A second advantage is the ability of this technique to allow measurements of the reaction at a lab angle of 0°due to the beam stopping before the detectors. This is advantageous as at this point the elastic scattering cross section is a minimum and the resonances are readily resolved.

An additional advantage of the inverse kinematic geometry (i.e. α-target) over the traditional geometry is the ability to reach lower excitation energies, as shown below. Here E_{beam} is the beam energy in the conventional kinematics and E'_{beam} is the beam energy in the inverse geometry, and M and m are the masses of the heavy and light particles respectively.

$$E_{c.m.} = E_{beam}\frac{M}{m+M} \tag{2.6}$$

and

$$E_{c.m.} = E'_{beam}\frac{m}{m+M} \tag{2.7}$$

are the equations which relate the centre of mass energies of the two geometries to the beam energy. The energy of the recoil particle in the lab frame can be expressed as,

$$E_m = E_{beam}\frac{m^2}{(m+M)^2}\left[cos\theta_{lab} + \sqrt{\left(\frac{M}{m}\right)^2 - sin^2\theta_{lab}}\right]^2, \tag{2.8}$$

and

$$E'_m = E'_{beam}\frac{4mM}{(m+M)^2}cos^2\theta_{lab}. \tag{2.9}$$

Where E_m is the energy of the recoil particle in conventional geometry and E'_m is the energy of the recoil particle in the inverse kinematic geometry. Setting the lab angle of the recoil particle to $\theta_{lab} = 0$ and then dividing Equation 2.9 by Equation 2.8 produces the following relation between the centre of mass energies for the two geometries,

$$E'_m = 4E_m\frac{\left(\frac{M}{m}\right)^2}{\left(1+\frac{M}{m}\right)^2} \sim 4E_m. \tag{2.10}$$

It is evident from this equation that if $M \gg m$ the energy of the recoil particle is four times greater for the inverse kinematic geometry than the normal geometry for the same centre of mass energy. This permits lower energies of the excitation function to be probed with the inverse geometry compared to normal.

A disadvantage of this TTIK method is the achievable resolution of both energy and angle of the detected particles. Factors including energy spread, cross sectional area and spread of the beam and energy straggling of the recoil particles in the target can all affect the resolution. Overall, the energy and angle resolution of the detected particle deteriorates with lab angle.

2.4 Charged Particle Interaction

This section will briefly describe the interaction of a charged particle with matter. This affects not only the energy loss of the beam through the window and gas, but also the energy loss of the recoil in the gas and the particle detection system. In the resonant scattering reaction, described in the section above, charged particles are the reaction products. These products, along with their energies and angles of emission, are the objects of interest which need to be detected.

When an ion passes through a material it will interact mostly electromagnetically with the electrons in the atomic lattice due to the charges of the ion and electrons. This is typically a Coulomb interaction between the ion and electron. The electrons will absorb energy from the ion, either by ionisation or excitation, causing the ion to lose energy and slow down. To calculate the energy loss an integration must be made between a head on collision to a glancing blow. This integration produces the Bethe-Bloch equation [13],

$$\frac{dE}{dx} = \left(\frac{e^2}{4\pi\varepsilon_0}\right)^2 \frac{4\pi z^2 N_A Z\rho}{mc^2\beta^2 A}\left[ln\left(\frac{2mc^2\beta^2}{I}\right) - ln(1-\beta^2) - \beta^2\right], \tag{2.11}$$

with,

$$\beta^2 = \frac{v^2}{c^2}, \tag{2.12}$$

where z and Z are the charges of the incoming particle and the collision material respectively, v is the velocity of the particle. Also, A and ρ are the atomic mass and density of the material and m is the electron mass. Finally I is the average ionisation potential of the material.

Here, for any specific material, the energy loss of the ion is proportional to,

$$\frac{dE}{dx} \propto \frac{z^2}{\beta^2}, \tag{2.13}$$

where,

$$\beta^2 = \frac{v^2}{c^2}. \tag{2.14}$$

At non-relativistic energies, where $v \ll c$, $E = \frac{1}{2}mv^2$, then

$$\beta^2 = \frac{2E}{mc^2}, \tag{2.15}$$

hence, for a given material,

$$\frac{dE}{dx} \propto \frac{mz^2}{E}, \tag{2.16}$$

Figure 2.11 shows a typical energy loss curve, the example provided is for the energy loss of an α-particle in silicon. Over most of the curve the general trend of dE/dx is proportional to $1/E$, however at low energies dE/dx begins to fall. This decrease is due to the ion picking up electrons as it reduces in velocity causing a reduction in charge (z).

The information provided in this chapter is used to calculate the energy loss of the beam and recoil particles through the window, target gas and the detectors.

2.4.1 R-Matrix

First introduced by Lane and Thomas [80] the R-Matrix theory is a powerful tool for the examination of resonance reactions. In the study of a resonance reaction of the form $a + A \to C^* \to b + B$, R-Matrix theory can be utilised to extract the parameters of the states populated in the compound nucleus from the experimental excitation functions and angular distributions. R-Matrix theory was developed in the 1950s making it an extremely well developed theory which, when reduced to into its simplest form, produces

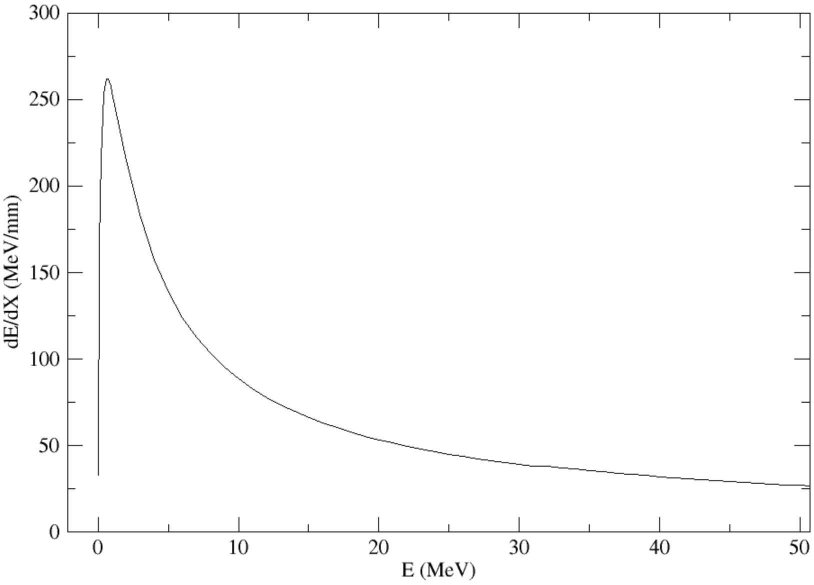

Figure 2.11: The energy loss curve of an α-particle passing through silicon. Note how the general trend of the curve is that of 1/E up to high energies where dE/dx starts to fall. This graph was produced using data provided by *dedx.*[79]

the Breit-Wigner expression for a single resonance [81],

$$\sigma_{if} = \frac{\pi(2J+1)}{k^2(2S_i+1)(2S_f+1)} \frac{\Gamma_i \Gamma_f}{(E_i - E_c)^2 + \frac{\Gamma^2}{4}}. \tag{2.17}$$

Here Γ_i and Γ_f are the partial resonance widths of the incoming and outgoing channels respectively whilst Γ is the total width of the resonance. Also, E_i is the centre of mass energy, E_c is the resonance centre of mass energy and k is the wave number. Finally, S_i and S_f are the spins of the incoming and outgoing channels respectively and J is the spin of the resonance.

The partial resonance widths can also be represented by,

$$\Gamma_i = 2P_i\gamma^2, \tag{2.18}$$

where P_i is the penetrability factor and γ is the reduced width. Thus for a given value of the reduced width, the partial width depends strongly on the penetrability through the barrier. This implies that the resonances get narrower as the spin increases and the cross section gets smaller. Conversely, for the higher spin states the cross section scales as (2J+1) and hence the cross section increases. Correspondingly it is important to perform a careful R-matrix analysis which takes into account both the width of the resonances and their magnitude. For an in depth description, a full derivation and further details see [80]

Chapter 3

Experimental Details

The experiment presented in this thesis was performed by the Charissa collaboration at the Holifield Radioactive Ion Beam Facility (HRIBF) [82] at Oak Ridge National Laboratory (ORNL), USA in April 2009. A schematic of the facility is shown in Fig. 3.1.

The ^{14}C nucleus was investigated via the ^{4}He(^{10}Be,^{10}Be)^{4}He resonance scattering reaction. A chamber filled with helium gas was exposed to a beam of ^{10}Be of varying energies, 25, 27, 29, 32, 34, 38, 40, 42,44 and 46 MeV, provided by a tandem Van de Graaff accelerator. The Q-value for this reaction is Q = 0 MeV but produces ^{14}C nuclei that have excitation energies in excess of the 12.011 MeV threshold for decay into ^{10}Be and an α-particle.

The details of the experimental set up are split into four main sections; the accelerator, the reaction chamber, the charged particle detectors and the data acquisition system and associated electronics.

3.1 Accelerator Facility

The Holifield accelerator facility contains both a tandem accelerator and the Oak Ridge Isochronous Cyclotron (ORIC) but, for this experiment, only the tandem accelerator

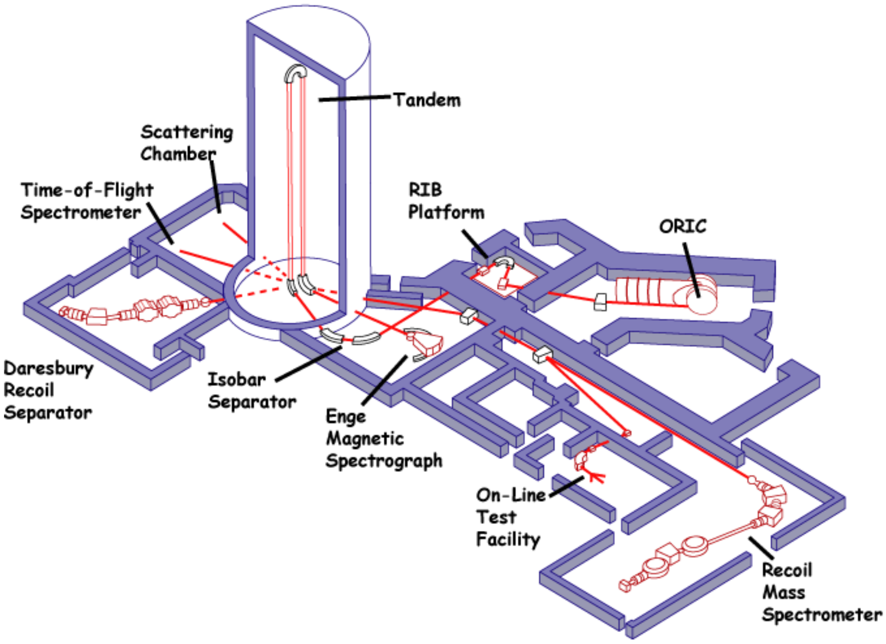

Figure 3.1: Schematic of the layout of the Holifield Radioactive Ion Beam Facility at ORNL, US. Note that the tandem acellerator is positioned vertically. This schematic was acquired from [83].

was utilised. As the name suggests, the purpose of a particle accelerator is to impart kinetic energy to a chosen beam of nuclei. At different energies different interactions between nuclei can take place, for example, additional energy can be used to overcome the Coulomb barrier. By selecting the specific energy of a beam of nuclei it is possible to tailor an experiment to have a greater yield of one type of reaction over unwanted reactions. If an electrostatic accelerator maintains a constant potential difference V, between the terminal and the grounded surroundings, and the chosen isotope holds a charge q then as the charged particle passes through the accelerating field it will acquire kinetic energy qV. These accelerated particles are then directed to a target chamber where the interactions will take place.

The tandem accelerator is an example of an electrostatic Van de Graaff generator which maintains a single high voltage terminal. Each of the main components of the accelerator facility is described in detail in the following sections.

3.1.1 Ion source

To create the *negative* ions that are required for injection into a tandem accelerator a specialised ion source is necessary. The type of ion source required is dependent on the element that is to be accelerated. For the studies made in this thesis a caesium sputter source is used to create these negative ions. A schematic of a caesium sputter source can be seen in Fig. 3.2.

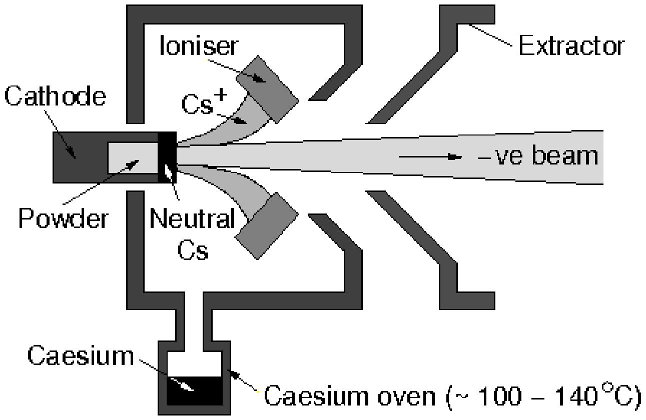

Figure 3.2: A schematic diagram of a caesium sputter ion source of the type that was used in the experiment. The powder shown in the diagram is formed of the isotope to be accelerated. Adapted from [84]

The reservoir of caesium is heated to around 120°C causing caesium to vaporise, the vapour then travels through a vacuum into the main body of the source. The cathode in the main chamber is cool in comparison to the oven and a quantity of the caesium vapour will condense onto it. Additionally, the ionisers are heated causing any caesium coming in contact with them to heat up and ionise. These *positively* charged caesium ions are accelerated towards the cathode where, upon impact, they will sputter atoms out of the source material from within the cathode. This material, or ’pill’, is a powder form of the element to be accelerated which, when sputtered away from the cathode, will gain electrons by passing through the *neutral* caesium coating on the cathode, forming a *negatively* charged beam. The entire source is maintained between 100 and 150 kV below ground, therefore repelling the negative ions out of the source, to be injected into an accelerator.

Most of the ions exiting the source will have only picked up one extra electron, however there is a probability that some may have more. To select only the -1 charge state and to remove impurities such as hydrogen and oxygen from residual water vapour in the source, a bending magnet is placed between the source and the accelerator. The principles of the bending magnet are explained in the upcoming analysing magnet section.

^{10}Be **production**

For the purpose of this experiment it was necessary to use a ^{10}Be source pill. However this isotope is not naturally occurring therefore it requires synthesising. In this particular case the isotope is created by placing ^{13}C into a high neutron flux facility to create the beryllium via the ^{13}C(n,α)^{10}Be reaction. ORNL have the facility to create ^{10}Be in one of their on site nuclear reactors and then chemically separate it from contaminants.

Beryllium is very easily oxidised into the molecule beryllium oxide, BeO, therefore the powdered form of this material was used in the source causing the ions exiting the source to be negatively charged Be^{-}O molecules.

3.1.2 Tandem accelerator

A tandem accelerator is an electrostatic Van de Graaff generator which accelerates negative ions using a very high positively charged electrode known as the terminal. It differs from a normal (single ended) Van de Graaff as the isotope is accelerated towards the terminal as well as away from it. The negative ions, produced by the ion source, are injected into the accelerator where they are attracted to the positive terminal. The ions accelerate as they travel down the beam tube, which is under vacuum, until they enter the terminal where they impact upon a jet of low pressure gas. This impact will strip the ions of some or all of its electrons causing it to become positively charged, therefore accelerating it away from the terminal. The energy imparted to the particle under acceleration depends on both the voltage of the terminal and the final charge state of the particle, as shown by Equation. 3.1. Here V_T is the terminal voltage, q is the charge state after the electron stripper and V_{inj} is the ion source injection voltage.

$$E = V_T(1 + q) + V_{inj} \tag{3.1}$$

To accumulate charge onto the terminal, high voltage power supplies induce a charge onto one or more Pelletron chains. Pelletron chains are links of metal pellets connected with a nylon insulator. The metal parts of the chain are charged using induction, the method of which does not utilise coronal discharges or rubbing contacts. A negatively charged inductor pushes electrons off the chain whilst it is in contact with the grounded drive pulley. As the chain leaves the drive pulley it is still inside the inductor field therefore it retains a net positive charge. The chain transports this charge to the terminal where the reverse process takes place. A schematic of a typical tandem accelerator is shown by Fig. 3.3, which also shows that the accelerator tank is filled with SF_6, a gas with a greater dielectric strength (the maximum electric field strength the gas can withstand before breaking down and losing its insulating properties) than that of air or nitrogen. This gas allows the terminal to accumulate a greater charge without discharging (sparking) along the column or to the tank wall.

The support columns holding the terminal in place are comprised of metal plates which are electrically insulated from each other by glass blocks.

The metal plates are connected in series by a set of resistors and the columns are surrounded by a set of metal rings in an effort to create a smooth voltage gradient from the base of the column to the terminal, Fig. 3.4. This leads to a uniform acceleration of the ions as they travel through the accelerator.

A large powerful spring at either end of the column compresses the column holding it

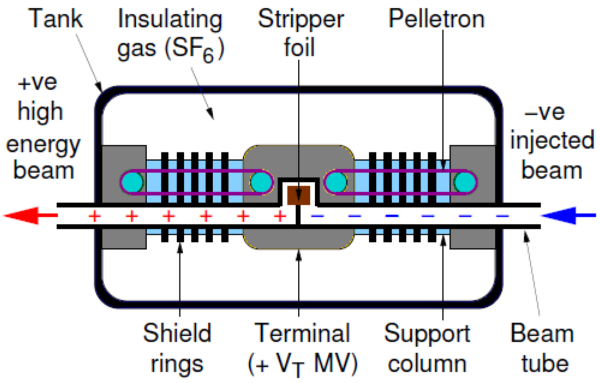

Figure 3.3: A simplified schematic diagram showing the internal components of a typical tandem accelerator. Adapted from [84]

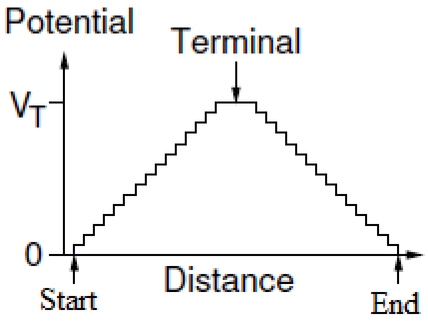

Figure 3.4: The gradient of the voltage with respect to distance along the beam path in the accelerator. The gradient is tailored to be as smooth as possible in order to uniformly accelerate ions through the accelerator.

suspended in the pressure vessel. This negates the need for supports holding the terminal in place which could provide a path to ground for the high voltage at the terminal. Very large tandems are generally positioned vertically (so they do not sag under their own weight), or they bend the beam by 180° at the terminal as shown by Fig. 3.5.

Stripping Gas

Whilst in the high-voltage terminal it is necessary to strip the negative ions of their electrons to create a positive ion that can be accelerated away from the terminal. As up until the terminal the BeO molecule was being accelerated, a foil stripper was unsuitable

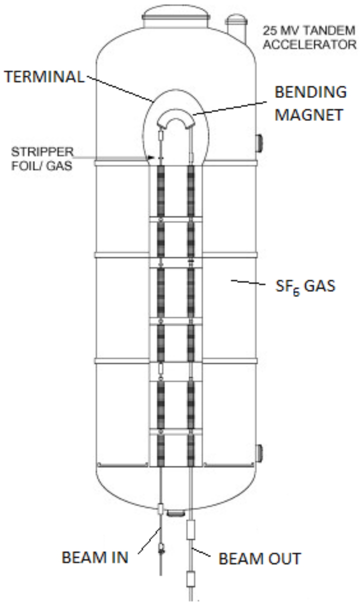

Figure 3.5: Schematic diagram of an up-down tandem accelerator. The only difference between the operation of this type of tandem and a normal tandem comes from the bending magnet. This magnet curves the path of the beam by 180° in the terminal. Adapted from [85]

as this would cause the beam to scatter. Instead, the stripping is achieved by producing a canal of low pressure gas in the beam path which creates an electric field barrier that strips the electrons from the beam (the less dense gas has less of a scattering effect). Additionally the barrier will tear apart the molecule leaving ions of beryllium and oxygen.

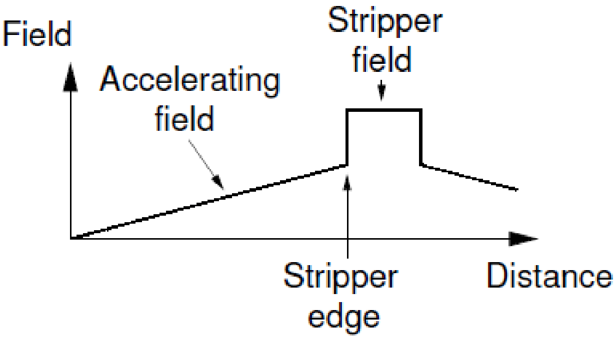

Figure 3.6: A plot of the electric field in the vicinity of the stripper gas within the terminal. It is the rapid increase in the electric field at the edge of the gas that causes the stripping of the electrons from the ion. From [84]

As evident in Fig. 3.6, the electrical field experienced by the particles exhibits a large increase around the edge of the stripping gas. This large increase causes a sudden impulse which results in the ions being stripped of their electrons. The more electrons that are removed from the ion the greater its positive charge, and the greater the acceleration away from the terminal.

Analysing magnet

As the positively charged ions emerge from the tandem accelerator they pass into an analysing magnet where a uniform magnetic field bends the beam into a circular path. The radius of curvature of the beam is given by Equation 3.2, where m, v, and q are the mass, velocity and charge of the ion, and B is the strength of the magnetic field. Therefore, if the magnetic field is a constant, particles with different masses and charges will curve at differing radii separating them into different paths. By specifying the magnetic field strength and placing a thin slit at the exit of the magnet it is possible to select only those particles with the correct energy, mass and charge required. By using this method it is possible to remove unwanted contaminants and charge states and also to fix the beam energy.

$$r = \frac{mv}{qB} \tag{3.2}$$

The analysing magnet can also be used to control the terminal voltage. If the voltage is too high or low the beam will be deflected in the magnet too much or too little. By measuring the current of the beam between the slit at the exit of the analysing magnet it is possible to identify if the terminal voltage is correct. If the terminal voltage is incorrect there are three methods of rectifying; altering the charge on the chain, changing the corona probe position or changing the corona probe current. Changing the charge on the chain and the coronal probe position are slow methods. Changing the coronal probe current is an electronically controlled system with feedback from the terminal charge and is a fast changing system.

Beam Optics

To maintain the integrity of the beam it travels through evacuated pipes in an effort to reduce scattering collisions as these would cause energy loss in the beam. As the beam consists of positively charged ions it has a natural tendency to deform and diverge, due to electrical repulsion from the ions from the beam path but for the purpose of this experiment a narrow, well collimated beam was required. Along the beam line are a number of focussing magnets called quadrupole lenses. A quadrupole lens creates a hyperbolic magnetic field shape as shown in Fig. 3.7. If the beam axis is along the z axis then a single quadrupole lens will force the beam towards the centre of the beam line in either the x or y axis, but away from the axis in the y or x direction. To solve this problem a series of pairs, or triplets, of quadrupole lenses are place along the beam line at varying orientations to keep the beam focussed.

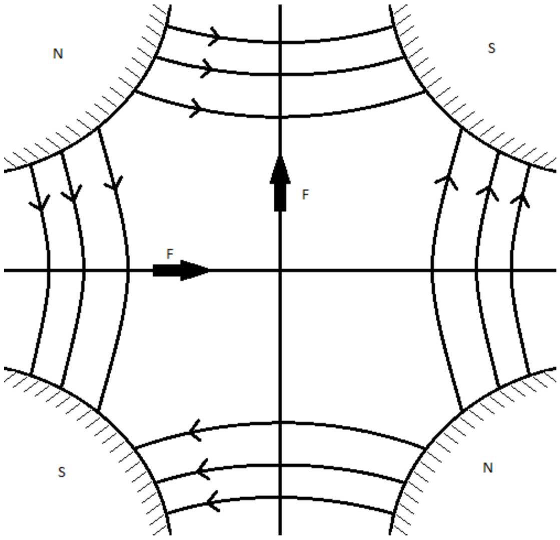

Figure 3.7: The magnetic field created by a magnetic quadrupole lens. The forces, F, are those applied to a particle moving perpendicular to the plane of the figure. These are used in pairs or triplets to focus a particle beam.

Not only are there quadrupole magnets along the beam line but to assist in guiding the beam into the reaction chamber there are also dipole magnets (single electromagnet to steer in one plane) and steering magnets (pairs of adjustable electromagnets to steer in any direction). The dipole magnets are used when the beam is required to bend at a large angle, such as around a corner, and are used to make large adjustments. The steering magnets are orders of magnitude weaker and are used to fine tune the trajectory of the beam.

3.2 The Reaction Chamber

A schematic displaying the arrangement of the components inside the reaction chamber is shown in Figure 3.8. As the chamber was filled with gas and the beam line was under vacuum, a 5 micron Havar® window was positioned between the two maintaining the pressure in the chamber. Havar® is a high strength non-magnetic alloy that comprises of Co/Cr/Ni/Fe/W/Mo/Mn.

The two silicon detector arrays each consisted of six wedge shaped detectors arranged in a lampshade configuration around the beam axis. This configuration is shown in Figure 3.9. The silicon detectors are mounted in the array so that the angle θ is at 46° from the beam axis, the centre of the array closest to the window is 160 mm from the window and the downstream array is 439 mm from the window. The polar angle subtended by the detectors in the array closest to the window, measured from the window, are between 13.5° and 42.2°. The angle subtended by the array further from the window is between 4.9° and 13.9°, slightly overlapping with the first array. A target ladder, at a distance of 336 mm from the window, could be inserted for calibration purposes and it is this ladder that held the silicon p-i-n diodes used as a zero degree monitor. Depending on the energy of the beam there were either two or three monitor detectors in a telescope on the ladder.

To prepare the chamber for use it was first brought down to vacuum before being filled

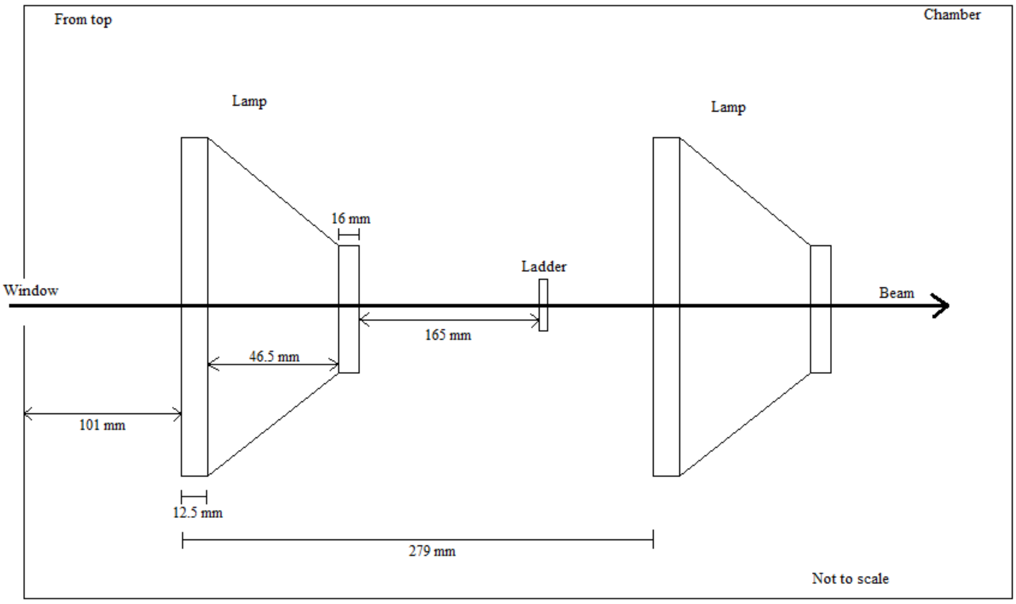

Figure 3.8: Schematic diagram of the reaction chamber setup. The silicon arrays (lampshades) are 160 mm and 439 mm from the window (measured from the point furthest from the window). The target ladder, on which the zero degree monitors were mounted, is at 336 mm from the window. The lampshades are at an angle of 46°from the beam line.

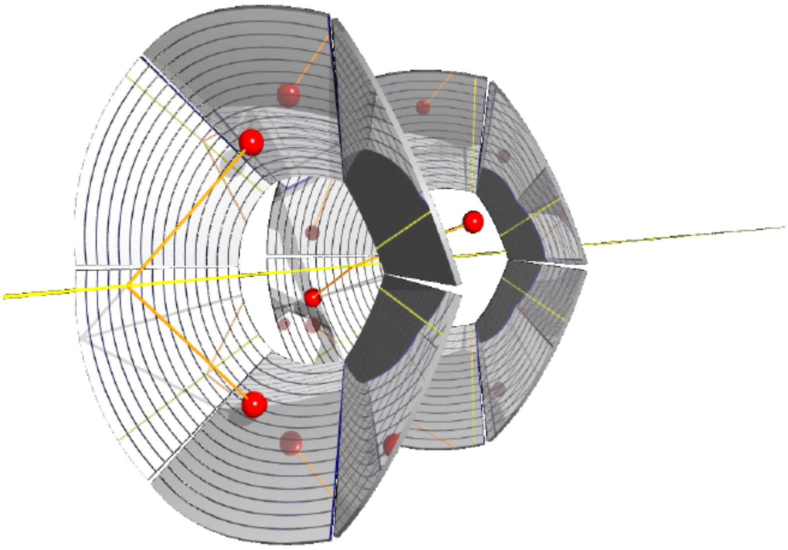

Figure 3.9: Configuration of the silicon wedge detectors in the 'lampshade' array. This view is from the window side of the chamber. The target ladder (not shown) is positioned in between the two arrays.

with helium gas to a pressure of 730 Torr. This pressure was maintained to ensure that the resonances were at the appropriate positions within the chamber. A greater pressure would have increased the number of resonances in front of the array, but at a risk of destroying the thin Havar® window containing the gas.

3.3 Detectors

An integral part to the experiment are the detectors. To reconstruct the resonance scattering events it is necessary to detect both the energy and scattering angle of both reaction products.

There are many forms of detectors that are used for nuclear physics, however, due to the type of reaction and the particles that are needed to be measured in this experiment only one type was utilised; the semiconductor detector. This choice was determined by the reasons stated in both Sections 4.2 and 2.3. The features of a semiconductor detector and the different types that were utilised in the experiment are explained in this section.

3.3.1 Semiconductors

It is known that every solid material has a specific set of energy bands that electrons can occupy and regions where they are forbidden. At lower energy is the valence band, the region where electrons are bound to individual atoms, and at higher energies there is the conduction band. The conduction band is an energy region where the electrons are not bound to a single atom and are free to move about the atomic lattice of the material. An electron can move between the regions if it gains enough energy to cross the band gap, the region between the two bands.

Semiconductors have a small, non-zero, band gap which allows few electrons into the conduction band by thermal excitation alone. In contrast, a conductor may have the two bands overlapping, or a partially full valence band, and an insulator will have a large energy gap between the bands. Figure 3.10 shows the band structure for the three types of material.

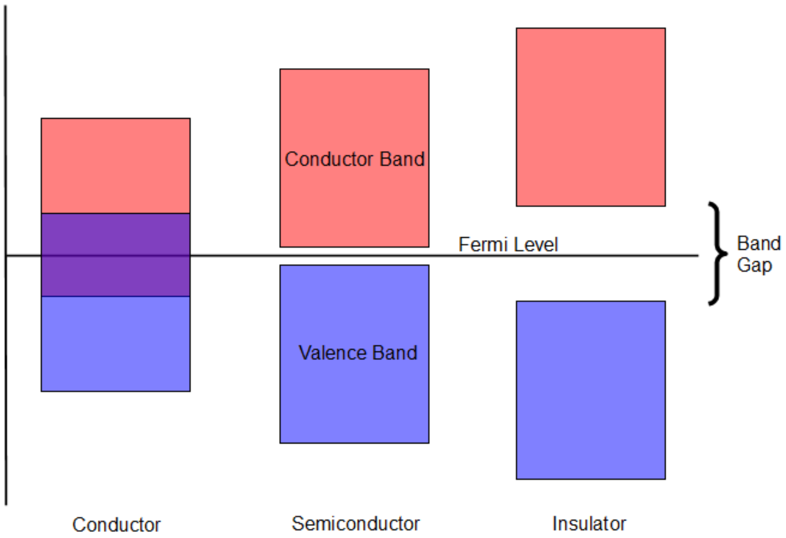

Figure 3.10: The band structure of a conductor, semiconductor and an insulator. Note that a conductor has overlapping bands and and an insulator has a large band gap. The diagram is not drawn to scale.

As previously mentioned the experiment utilised silicon detectors to measure the energy of the charged particles in the reaction. Silicon is a Group IV element therefore it has four valence electrons available which form covalent bonds with surrounding atoms. As all electrons in silicon are in covalent bonds the valence band is filled and the conduction band remains empty. The band gap in silicon is 1.11eV, small enough to allow a few (one in a billion) electrons to cross the gap using energy from thermal excitation at room temperature. This transfer of the electron into the conduction band leaves a vacancy in the valence band known as a hole. Electrons from the surrounding atoms can move into the hole which causes the appearance of the hole migrating through the lattice.

To create a viable detector it is necessary to control the electrical conductivity of the semiconductors which is achieved by introducing small amounts of dopants into the silicon. If a Group V element (e.g. P) is introduced into the silicon lattice, four of the valence electrons will form bonds with the silicon and the fifth is allowed to move freely through the lattice. This creates a new state for the electrons slightly below the conduction band called a *donor state*, the gap being around 0.05eV for silicon. This type of silicon will then have an excess of negative charge carriers due to the additional electrons in the lattice leading to the name n-type semiconductor.

Alternatively, if a Group III element (e.g. B) is introduced into the silicon lattice the three electrons will covalently bond with the surrounding silicon but a hole will be left. Again this creates a new state which in this case is just above the valence band, about 0.05eV for silicon. This leads to an excess of positive charge carriers, the holes, in the system causing this type of semiconductor to be call a p-type semiconductor. Figure 3.11 shows a schematic of the structure of a silicon lattice and the two types of doping. Both types of doping leave the material charge neutral.

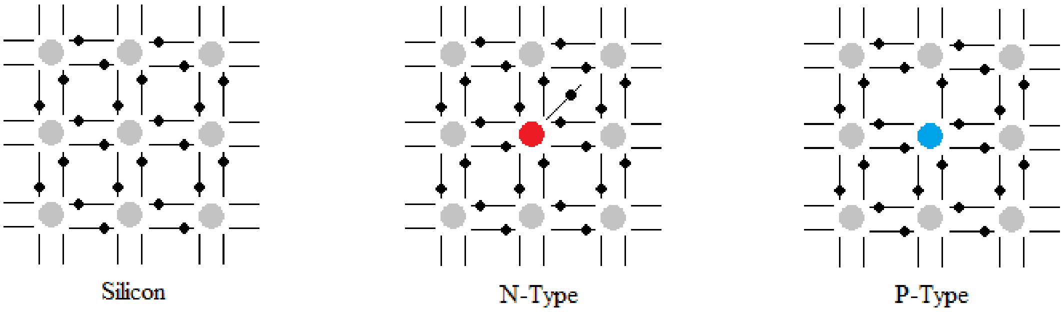

Figure 3.11: The structure of the atomic lattice in silicon along with n-type and p-type doped silicon. The red atom is a Group V element and the blue atom is a Group III element. Notice that the introduction of a Group V element in the n-type introduces an additional electron into the lattice. Alternatively the Group III element removes an electron from the lattice in the p-type. Adapted from [84].

When p-type and n-type semiconducting materials are brought into good thermodynamic and electrical contact they create what is known as a p-n junction. In this case the electrons in the n-type material will traverse the junction into the p-type material combining with the holes. Therefore, around the region of the junction all charge carriers are neutralised leaving a region known as the *depletion region*. Schematically this depleted region will appear to look like the silicon diagram in Figure 3.11.

The migration of the electrons from the *n*-type material into the *p*-type will leave behind positively charged donor atoms in the *n*-type material. Similarly, the movement of the holes from the *p*-type to the *n*-type material will leave negatively charged acceptor sites in the *p*-type material. These charges will create an electric field, around 1 volt, which halts any further migration of the charge carriers.

To improve the efficiency of a silicon detector a reverse bias (positive voltage on the *n*-type and negative on the *p*-type) is applied to the p-n junction which has a two fold effect. It forces more of the charge carriers into the opposite type material increasing the depth of the depletion region therefore increasing the working volume of the detector. It also increases the electrical field in the depletion region which allows for more efficient charge collection after an interaction has taken place.

As a charged particle enters the depletion region it will interact with the electrons to cause electron-hole pairs. As there is an electric field these will flow in opposite directions and the total number of electrons from the interaction can be collected. These electrons will form an electrical pulse which is directly proportional to the energy of the incident particle.

In the experiment two types of semiconductor detector were used, the surface barrier and the silicon strip detector. More detail on the configuration of these detectors can be found in the following sections.

Silicon Surface Barrier Detectors

As mentioned in Section 3.2, a set of surface barrier detectors were used as zero degree monitors during the experiment. This type of semiconductor detector is created by allowing one side of a thin sheet of *n*-type silicon to oxidise creating a layer of silicon dioxide which behaves like a *p*-type material. As shown in Figure 3.12 the two types of material then create a p-n junction. To allow a bias to be applied to the detector and to collect the signal a contact has to be applied to both sides of the detector. This is achieved by evapourating a very thin layer of gold or aluminium onto the surfaces of the p-n junction. The reverse bias is then applied to the p-type silicon which forces the depletion region into the n-type material.

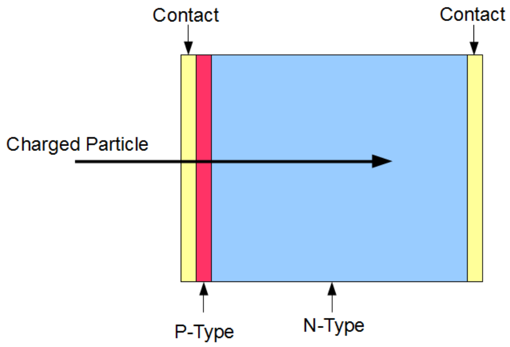

Figure 3.12: Schematic of a typical composition of a surface barrier semiconductor detector. When a reverse bias is applied to the detector the depletion region will move into the n-type silicon.

Depending on the beam energy during the experiment, there were either two or three monitors, in series, due to the recoil particles having greater energy at higher beam energies. For the beam energy range 25 - 38 MeV two surface barrier detectors were mounted in series on the target ladder. During this stage of the experiment 46 μm of Mylar foil was positioned in front of the detectors to absorb the beam and prevent damage to the detectors.

For energies 40 - 46 MeV a third monitor was attached in series as the recoil α-particles had gained enough energy to penetrate the two detectors alone. At these beam energies it was necessary to place additional Mylar in front of the detectors to stop the beam. Additional foils were added bringing the total thickness of the Mylar up to 144 μm. As the zero degree monitors were ΔE detectors the α-particles had to pass through each detector, therefore the detector mountings could not interfere with the path of the particle and, due to this, the detectors were mounted as shown in Figure 3.13.

The characteristics of the three monitor detectors are shown in Table 3.1. The detector

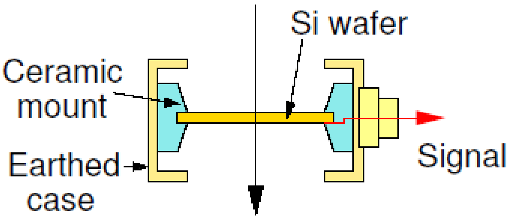

Figure 3.13: Diagram of the positioning of a silicon wafer within its mount. This type of mounting was required for this experiment due to the surface barrier detectors being used as zero degree monitors. Multiple detectors were placed in a telescope and this mounting allowed particles to pass through a detector into the one behind. From [84].

that was closest to the beam entrance window is labeled ΔE_1, the detector behind is ΔE_2 and when the third detector was added it was labeled ΔE_3. It is noticeable that although the detectors are all very similar in thickness the voltages applied to them are very different. Intrinsically a detector will have some leakage current and, as a detector is used it becomes radiation damaged also increasing the leakage. To compensate for the leakage current and maintain the depleted region the voltage applied to the detector is increased.

Table 3.1: Details of the zero degree monitor detectors used in the experiment. Detector ΔE_1 is the closest to the beam entrance window and ΔE_3 is the furthest. (Note, the voltage applied to detector 3 was not recorded.)

	Thickness / μm	Voltage / V	Average Leakage Current / μA
ΔE_1	157	70	2.20
ΔE_2	160	30	1.17
ΔE_3	150		1.83

Silicon strip detectors

The two lampshade detector arrays previously mentioned consisted of two sets of 6 Micron Semiconductor Ltd YY1 silicon strip detectors. This detector was chosen as, when placed into the array, the set of six cover almost the full 360 degrees azimuthally and a large polar angular range. Figure 3.14 is an example of one of the detectors used in the lampshade arrays.

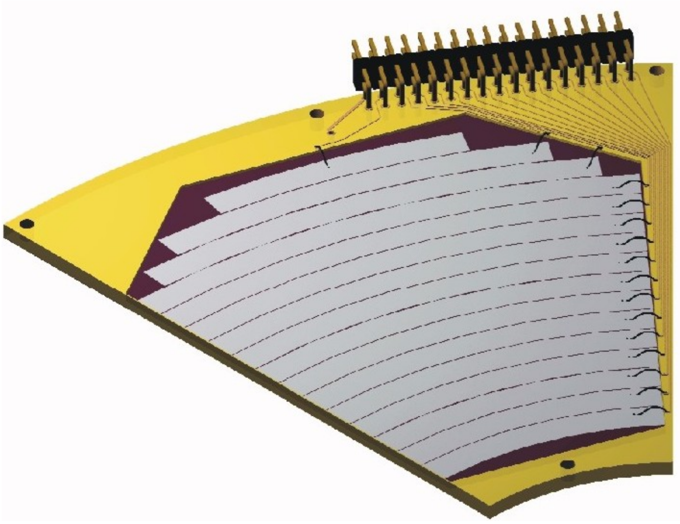

Figure 3.14: A Micron Semiconductor YY1 wedge shaped silicon strip detector, six of which were used in each lampshade detector array. There are 16 semiconductor strips on each detector mounted on PCB. Each strip is connected to the circuit on the board by a bond wire. The board leads to a connector with 16 pins, one for each strip, which will be attached to a preamplifier. From [86].

There are three main steps to create a detector which are shown diagrammatically in Figure 3.15. The first stage is to allow a crystal of n-type doped silicon to oxidise creating a layer of silicon dioxide around the crystal. The second stage is to etch out channels using lithography in the silicon dioxide creating a path to the silicon underneath. The third stage is to bombard the silicon with a Group III element, such as boron, which implants into the n-type silicon turning it into p-type. Using this method the areas covered by the silicon dioxide are not affected. For example, in Figure 3.15 two separate channels have been created. The detectors used in the experiment had 16 separate strips on a single silicon wafer.

Each single detector had 16 silicon strips which were around 3 mm in width. They range from 55mm in length to 130mm and for the purpose of this experiment they were 300 microns in thickness. As with all semiconductor detectors a reverse bias was placed

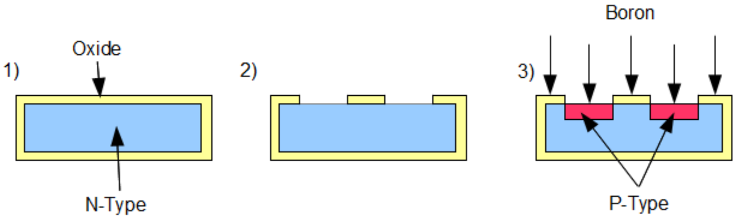

Figure 3.15: Schematic of the three steps involved to create a semiconductor detector. 1) A crystal of n-type doped silicon is allowed to oxidise. 2) Channels are etched into the silicon dioxide. 3) The silicon is bombarded with a Group III element.

on the silicon strip detectors to fully deplete the p-n junction which, in this case, was 50 Volts for all twelve detectors. As the back face of the silicon strip detectors have a single contact only one bias per detector has to be applied.

3.4 Data Acquisition System

The data acquisition (DA) system is the system via which the raw signal data from the detectors is converted into a digital format for storage on a computer for later analysis. It is used to convert the charge pulse from the detectors into digital information that can be analysed by a computer. A schematic diagram of the electronic system and the DA is shown in Figure 3.16.

Each lampshade detector strip was connected to a pre-amplifier which collected the charge pulse when a strip fired and converted it into a proportional sized voltage pulse. Each detector had 16 strips therefore has 16 outputs. The pre-amplifiers were in self contained pre-amplifier modules with a 16 channel input and 16 channel outputs, therefore one pre-amplifier module was used per detector. This 16 channel signal was passed to the main amplifiers modules which shape the pulse and increases the amplitude further. The amplifiers had internal leading edge discriminators which could set thresholds to be used as a common signal for all channels within the module. The main amplifier modules available were 8 channel amplifiers (of Edinburgh/RAL design) so the signals from the 16 channel pre-amplifier modules had to be split into two amplifier modules (24 amplifier modules were used for the lampshade detectors). The 8 channel signals from the main amplifiers were then split into two paths, the first going into the analogue to digital converter (ADC) to be digitised and recorded if the event is accepted (these were Silena 9418 VME ADCs). The ADC is connected to a Silena ADC controller (SAC). The second MA output signal was from the internal leading edge discriminator signal which enters into the main trigger logic system where it was passed through a CAMAC module then an ECL/NIM converter to allow the signal to enter a FIFO unit. Two 16 channel main amplifier modules fed into each 16 channel input on the CAMAC modules. The CAMAC modules were the logic unit which OR'ed the signals from the main amplifiers. The CAMAC units only had inputs for 64 channels (four 16 channel inputs) so 3 CAMAC units were used. The ECL/NIM converter combined the signals from 2 of the CAMAC units and fed the signal into the FIFO. The FIFO unit OR'ed the signals from the CAMAC units and if any two strips from all of the detectors fired then the system was triggered. The logic system is finally connected to the SAC (trigger) which allows the system to determine which events to record. The main trigger was thus a singles trigger which activated the acquisition for every particle that entered the detection system.

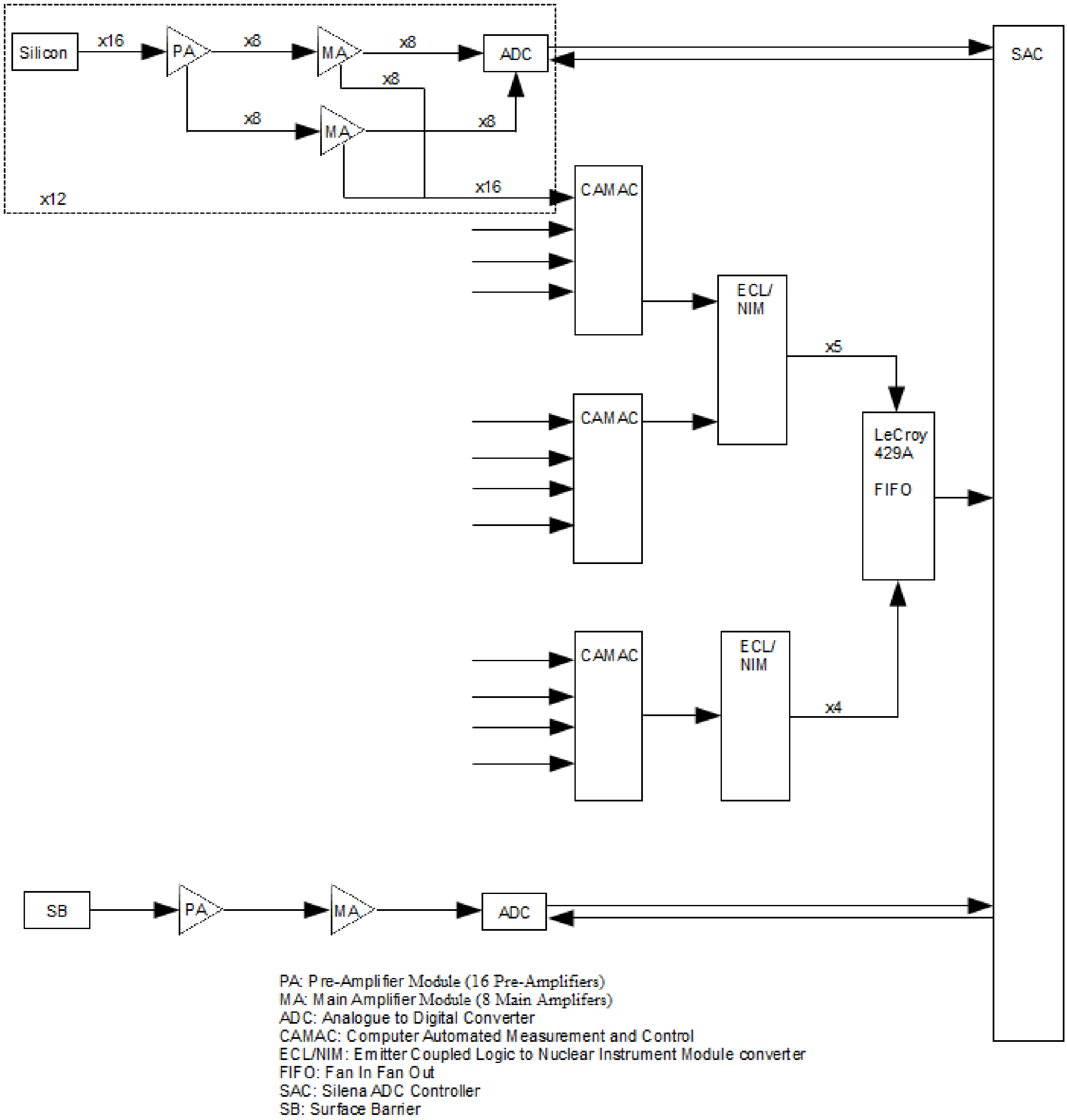

Figure 3.16: A schematic diagram of the electronics and data acquisition system set up for the experiment.

Chapter 4

Data Analysis and Results

The analysis of the data taken in the experiment was performed using the software package SUNSORT [87]. The software extracts the ADC output values from the raw data on an event-by-event basis. The events are then manipulated via a *sortcode* which is written in FORTRAN 77. Sunsort has a graphical user interface that allows the user to create 1 and 2 dimensional spectra using the data manipulated by the sortcode.

The analysis was performed in various stages which are presented in this chapter in the order they were enacted.

4.1 Calibration of Detectors

As shown in Section 3.4 the surface barrier detectors and each individual strip on the silicon strip detectors are connected to their own pre-amplifier, amplifier and ADC. Every channel in the amplifiers had their own gain settings and each ADC had an associated offset. These offsets meant that a zero voltage input would not always correspond to a zero voltage output. These two factors meant that two particles of equal energy entering separate strips on a detector or two different surface barrier detectors would produce a different output in the ADCs. Consequently, the first stage of calibration was to correct for the zero offsets and match the gains to ensure a uniform response across the detectors. The calibration of the two types of detector, zero degree and lampshade, are described below.

4.1.1 Calibration of PIN Silicon Wafers

To calibrate the zero degree monitors an ^{241}Am source, producing a 5.4856 MeV α-particle, was positioned in front of the detectors producing a single peak in the one dimensional spectra for each of the detectors. However, to calibrate properly and to calculate the offsets, two calibration peaks are required. The second calibration peak for the three zero degree monitors was provided by the analysis of the $E\Delta E$ particle identification curves. These two dimensional graphs are produced by plotting the energy deposited in one detector against the energy deposited in the detector behind. As there were only three zero degree monitors only two particle identification plots could be produced, the first (a) compares detectors ΔE$_1$ and ΔE$_2$ the second plot (b) comparing detectors ΔE$_2$ and ΔE$_3$.

From these plots it is possible to identify the tracks caused by protons, tritons and α-particles. As the thicknesses of the detectors are known (Table 3.1) the energy at which the protons, tritons (it was determined that the middle set of tracks were tritons as the association of the particle identification line with deuterons was completely inconsistent with a linear energy calibration linked with protons, ^{4}He and what was known from the α-source calibration) and α-particles breakthrough the second detector in each pair can be calculated using the equations stated in Section 4.2. This provides three additional peaks for energy calibration for detectors ΔE$_2$ and ΔE$_3$ but not ΔE$_1$. However, three additional points can be extracted from plot a) by extrapolating the traces back to the zero point on the x-axis. This was achieved by taking multiple points along the trace and plotting a polynomial line through the points in the software *xmgrace*. The software

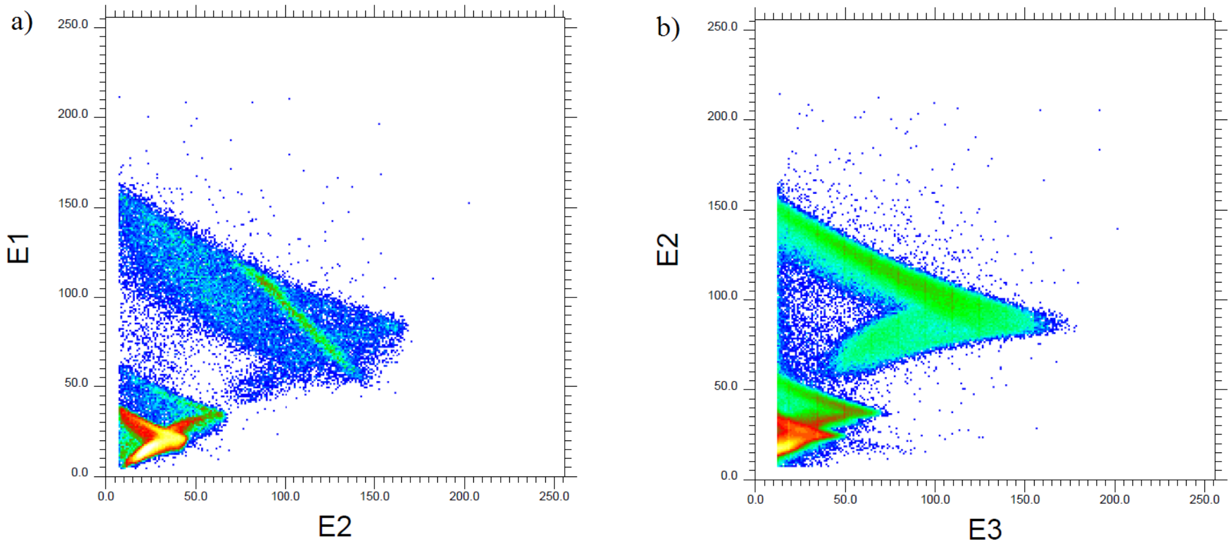

Figure 4.1: Particle identification (PID) plots for zero degree monitors. The plot on the left compares the energy deposited in the first monitor (closest to the window) on the y-axis with the energy deposited in the seconde detector on the y-axis. The plot on the right is the PID plot for the second and third detectors. The units are the channel number.

then extrapolated to provide the three calibration points. The breakthrough positions along with where the extrapolation took place are plotted by the red lines in Figure 4.2. From this plot we also see that the detectors, particularly detector 1, had a very non-uniform thickness, hence the broad α-particle trace. The mono-energetic α-particles, from the calibration source, will lose varying amounts of energy through different thickness silicon on the same detector, hence the energy spread in the plot. It is also believed that the detectors were not cut correctly and the detector wafer does not lie along the correct crystal lattice of the silicon, which would cause varying energy loss in the detector (channeling). The diagonal line which can be seen in the α-particle trace for detectors 1 and 2 is from break through α-particles. This line is making a 45° angle on the plot and is caused by the previously mentioned faults with the detector, hence the particle is depositing more energy in detector 1 than a uniform thickness detector. If the line was rotated it would match up with the point from where the calibration was taken. For calibration purposes the thickest part of the detector was used hence the position of the red line in the plot.

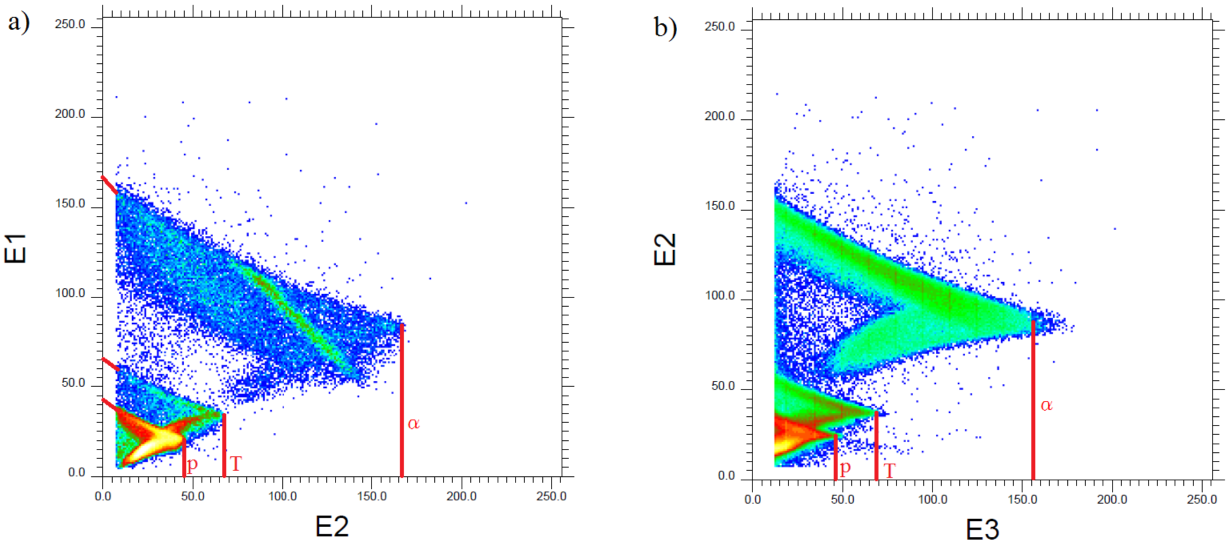

Figure 4.2: This plot indicates the positions at which the energy calibrations were taken for the zero degree monitors. The traces in the plot are from protons, tritons and α-particles. Units are the channel number.

The total of four points were plotted to produce a straight line graph of the form $y = mx + c$ where m, the gradient, is the gain and c, the intercept, is the offset. The gain and the offset were applied, using Equation 4.1, to the ADC output values, ADC(i), to convert the channel numbers into energy in MeV.

$$E(i) = ADC(i) \times gain(i) + offset(i). \tag{4.1}$$

Figure 4.3 is the straight line fit for one of the zero degree monitors (the example is for monitor 2). Each of the individual channels for the lampshades and each zero degree monitor had their own calibration fit.

As mentioned in the previous chapter, different thicknesses of Mylar were placed in front of the zero degree monitors dependent on the beam energy in use. To account for the energy lost in the Mylar an energy loss polynomial was created using the program

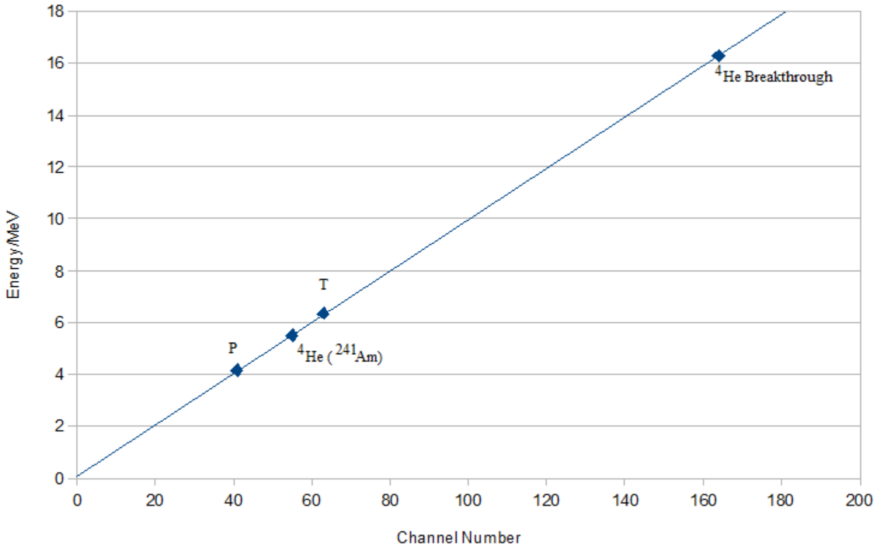

Figure 4.3: Straight line fit for the calibration for one of the zero degree monitors. This example is for monitor 2.

dedx.

4.1.2 Calibration of the Silicon Strip Detectors

The calibration of the lampshade detectors was in principle very similar to that of the zero degree monitors. However in this case the lampshade closest to the window had the ^{241}Am source positioned in front producing the 5.4856 MeV α-particle whereas the lampshade further away from the window had a ^{244}Cm source providing a 5.8048 MeV α-particle.

A 100 μgcm^{-2} gold target was positioned on the target ladder between the lampshades and a 32 MeV ^{10}B beam was produced by the accelerator to enter the chamber. The energy loss of the beam through the Havar window was calculated by *LISE++* [88] to be 6.422 MeV therefore the beam energy on impact with the gold target would be 25.578 MeV. Then the beam elastically scatters from the heavier gold target to provide a second calibration point for the downstream set of detectors. The small kinematic fall off effect due to angle was ignored in this calibration for reasons explained below.

A second calibration point for the upstream lampshade was to be provided by a background radon count, however, the counts were too low to be of statistically significant. Therefore, only a simple energy calibration could be performed on the upstream detectors in which it was not possible to extract offsets. The calibration for the downstream detectors was sufficient for the current analysis, where it is only necessary to trace the angular dependence of the data and matching the energy response of the strips is the crucial feature. Due to these complications the lampshade detectors were only utilised for angular correlation analysis. As the downstream detectors had two calibration points they were calibrated and the upstream detectors were cross calibrated with them. This was achieved by utilising two-body kinematics which tells us that the energy and angle of the two particles are linked. In this situation the two particles entered detectors in different arrays, as the energy of one of the particles is a known (as it enters the calibrated detector array) the other particle can be calculated by assuming the interaction point and iterating until the angles match. This method of calibration was not accurate enough to provide precise energy calibration for the lampshade detectors which is why they were only used for angular correlations. Figures 4.4 and 4.5 display the un-calibrated and calibrated lampshade data for the α-particle and the elastic scattering data from the ^{10}Be beam scattering from the gold target.

4.2 Beam-Gas Interaction

An important aspect in the analysis of the data was to determine where along the beam path within the chamber the actual interaction between the beam and target gas took place. This information is important as it allows the precise calculation of the excitation energy of the ^{14}C isotope.

For the zero degree monitors it is possible to calculate the energy loss of the beam

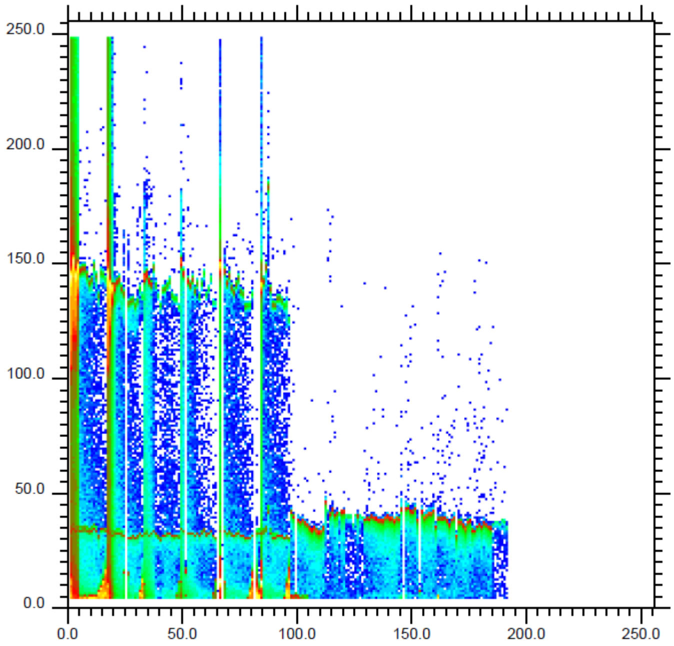

Figure 4.4: A plot of the uncalibrated data from all 196 channels of the lampshade silicon arrays, channel number on the x-axis and energy on the y-axis (units are arbitrary). The gap on the second half of the channels is due to a lack of gold elastic scattering data.

at each distance through the chamber. This allows the centre-of-mass energy at each distance, for the ^{10}Be+α system, and the excitation energy to be calculated, through two body kinematics. Once the emission energy of the α-particle is known the energy loss of that particle through the remainder of the gas can be calculated. There is a direct relationship between the energy of the particle detected and the excitation energy, the approach is to fit a polynomial which can be used to look up the excitation energy.

The calculations for determining where the interaction locations occur for the lampshade detectors is more complicated as there are many paths from which a particle can scatter into the detectors. Therefore, from the measured α-particle energy it is not possible to know the path length, therefore the energy loss in the gas is also unknown. The approach was to take an average interaction location as an estimate then use kinematics to deduce the distance the interaction took place in the gas. This allows a better estimate of the distance the α-particle had to travel therefore a more accurate estimate of the

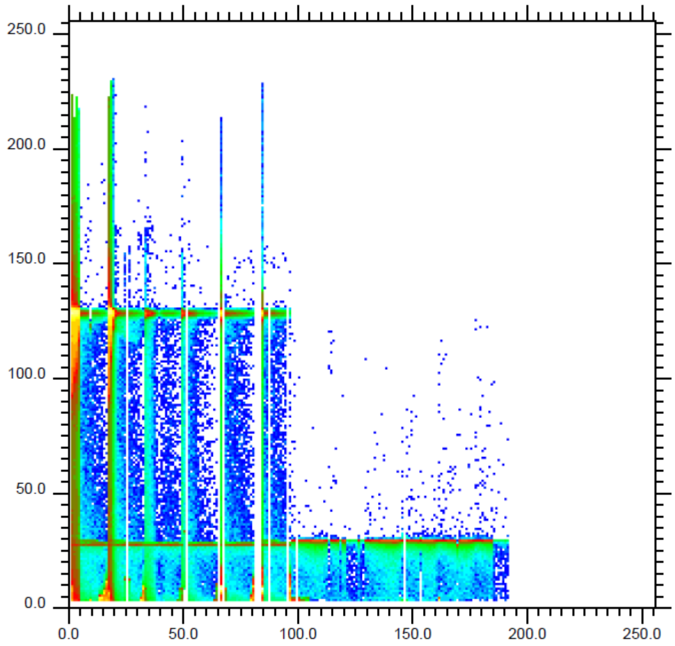

Figure 4.5: A plot of the calibrated lampshade detectors. The lower lines are the calibrated data from the α sources. The higher energy line in the first half of the detectors (downstream detector array) is data from the beam scattering elastically from the gold target.

energy loss. This was an iterative process that was repeated until the interaction location had been found.

This process allowed for the identification of the location along the beam path where the beam interacted with the target gas. Once the location had been identified for each event, a ^{10}Be and ^{4}He pair, could be assigned a specific energy corresponding to the excitation energy of the ^{14}C.

4.3 Calculation of the Excitation Energy Spectra

All data used to create the excitation function for ^{14}C comes from the zero degree monitors, the lampshades were only used for angular correlations. As multiple runs were performed, at multiple different beam energies and durations, the data sets had to be normalised to produce a single energy spectrum. Figure 4.6 shows the data sets before normalisation.

The graph indicates that there is not an inelastic component from the first excited state of ^{10}Be (3.3 MeV) as the spectral lines from the different beam energies overlap in terms of the cross section. If there were strong inelastic components then there would be additional components in the spectra when comparing higher energy beam measurements with that corresponding to a lower energy. From this it is assumed that there is only an elastic reaction channel for creating the spectrum. The different beam energy data sets, above 21 MeV in the spectrum, do not agree with each other as these were created by the highest energy beams. It was at these beam energies that the third zero degree surface barrier was utilised in the experiment. The third surface barrier detector may have been in an inefficient region which, it is believed, is the origin of the discrepancy between the results using only the two surface barrier detectors and using three detectors.

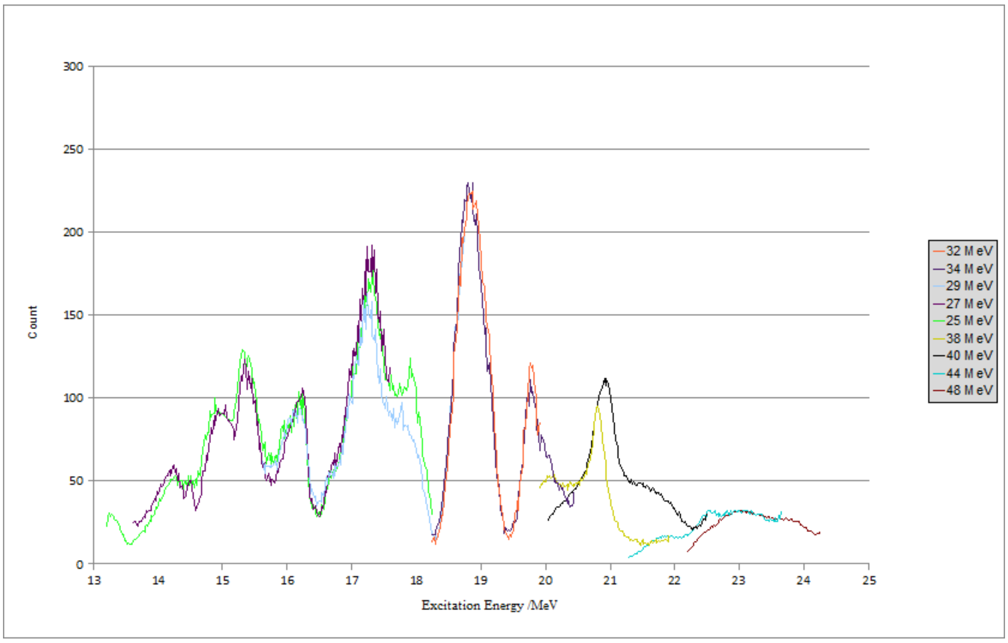

Figure 4.6: The spectral data from the zero degree monitors before normalisation. The different colour lines represent the data from the different energy beams. Excitation energy is plotted on the x-axis in MeV and the counts are on the y-axis.

4.3.1 Normalisation

During the experiment the duration of each run was recorded along with the beam intensity and the number of records created during the run. This allowed the data to be normalised creating one complete spectrum from the many different spectra created from the many different runs. The excitation energy spectrum from the zero degree monitors can be seen in Figure 4.7.

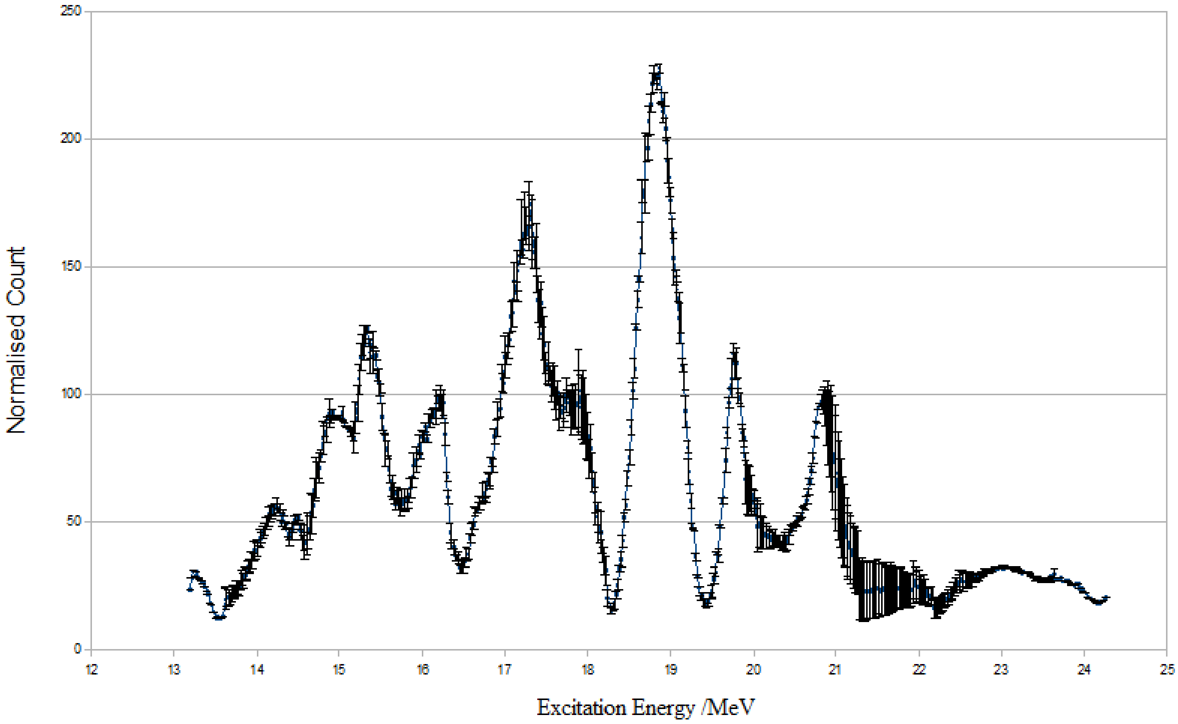

Figure 4.7: The normalised excitation function for ^{14}C from the zero degree monitors. The excitation energy on the x-axis is in MeV and the count is on the y-axis. The error bars in this graph are systematic errors introduced by the detectors not statistical errors.

The Q-value for the decay of ^{14}C into ^{10}Be and α is -12.011 MeV. Therefore to calculate the excitation energies for the states of ^{14}C 12.011 MeV must be added to the calculated centre-of-mass energy to determine the excitation energy of ^{14}C*.

The following table (Table 4.1) contains information about the excitation peaks in the spectrum for ^{14}C. The full width half maximum (FWHM) values were obtained by fitting the peaks with the software *Buffit*.

Table 4.1: Information on the excited states of ^{14}C as discovered in the spectrum created by the zero degree monitors.

Excitation Energy / MeV	Excitation Energy - Q-value / MeV	FWHM / MeV
14.54 ± 0.03	2.53	0.92 ± 0.08
15.11 ± 0.02	3.10	1.98 ± 0.28
15.35 ± 0.01	3.34	0.37 ± 0.07
15.51 ± 0.04	3.50	0.36 ± 0.10
15.91 ± 0.09	3.90	0.64 ± 0.22
16.22 ± 0.01	4.21	0.75 ± 0.07
17.50 ± 0.01	5.49	0.59 ± 0.04
17.98 ± 0.03	5.97	1.23 ± 0.23
18.80 ± 0.02	6.79	0.56 ± 0.04
18.86 ± 0.03	6.85	0.48 ± 0.01
19.76 ± 0.01	7.75	0.37 ± 0.02
20.66 ± 0.01	8.65	0.37 ± 0.04

4.4 Angular Distributions

As mentioned in Section 4.2 the interaction location for each event was been identified which permitted a plot of energy versus angle for each event in the lampshade detectors. Only data from events where two back-to-back detectors fired were analysed, a ^{10}Be particle in one detector and a ^{4}He particle in the detector 180° around the lampshade. The energy deposited in the detector was plotted against the angle at which it entered (measured with respect to the chamber entrance window), the beryllium entering at low angles and low energy due to its heavier mass and the helium at higher angles and energies.

Figure 4.8 illustrates a typical angle versus energy plot for each of the 12 lampshade detectors. In this figure a line has been drawn through the two regions created by helium particles entering the detector. These two regions originate from the same resonance in ^{14}C but are separated due to oscillations in the angular distribution. The large area below this line is due to the beryllium particles.

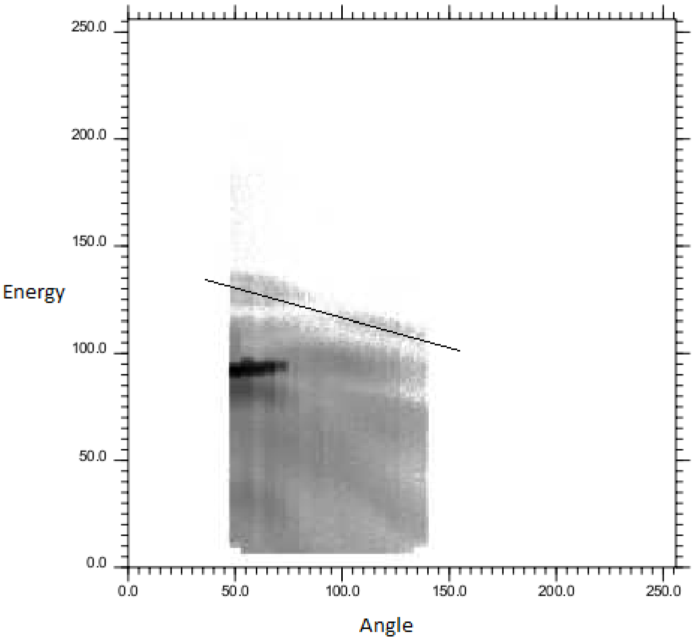

Figure 4.8: This plot shows the energy versus angle data from the one of the lampshade detectors. The α-particles enter the detector at higher energies and therefore are shown at the top of the plot. The mass below the helium comprises of ^{10}Be. The black line that runs through the helium data is where the periodicity was measured. All units are arbitrary.

The pattern created by the α-particles on the line shown in Figure 4.8 is dependent upon the spin of the particular state that is being displayed. Different spins will create patterns with different periodicities. This creates a method of identifying the spin of a state by comparing the periodicity of actual data to data created by a simulation where the spin is specified.

4.4.1 Monte Carlo Simulations

Simulations were created that mimicked the physics of the experiment utilising both *dedx* and a random number generator. The simulations produced an energy versus angle graph similar to those for the real data but only showing the information for the α-particles. In the monte carlo simulation the passage of the beam was simulated in steps of 1mm. At each step a resonant scattering probability was calculated using a Lorentzian distribution in which the excitation energy, width and spin were defined. If a resonance was populated then the emission of an α-particle was simulated including the particles energy loss in the gas and detection in the silicon array. The simulated events were reconstructed using the same code that analysed the experimental data. As mentioned the output of the simulation was a graph similar to Figure 4.8, the experimental data. Figure 4.9 displays the results of the analysis on the simulated data, there is a line drawn on in the same location as the previous graph.

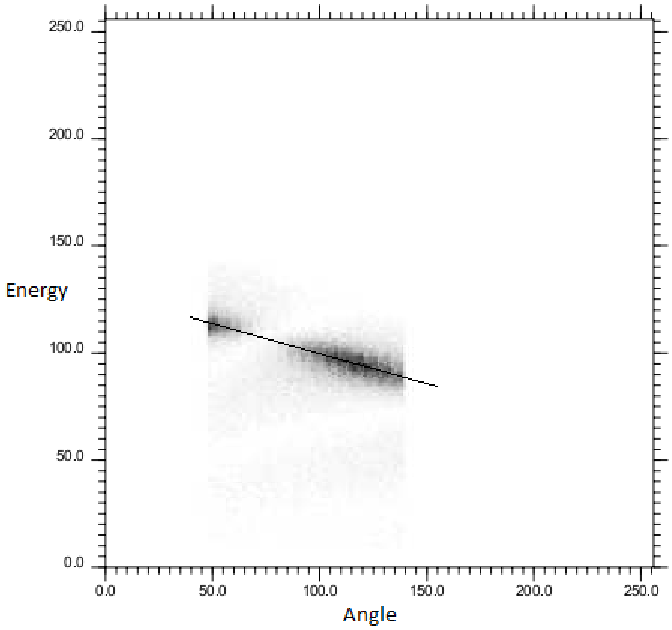

Figure 4.9: This is again an energy versus angle plot but for simulated data. Only ^{4}He data are plotted and the black line where the periodicity is measured is the same as in Figure 4.8. The simulated data was run through the same analysis as the measured data to produce this plot. All units are arbitrary.

To assign a spin to the state the data along the lines in Figures 4.8 and 4.9 is compared for each of the different spin simulations. The simulation, and its associated spin, with the closest match to the real data leads to the assignment of that spin to the state. Figures 4.10, 4.11 and 4.12 demonstrate this comparison process. These figures show the comparison process for the three states that could be identified in this manner.

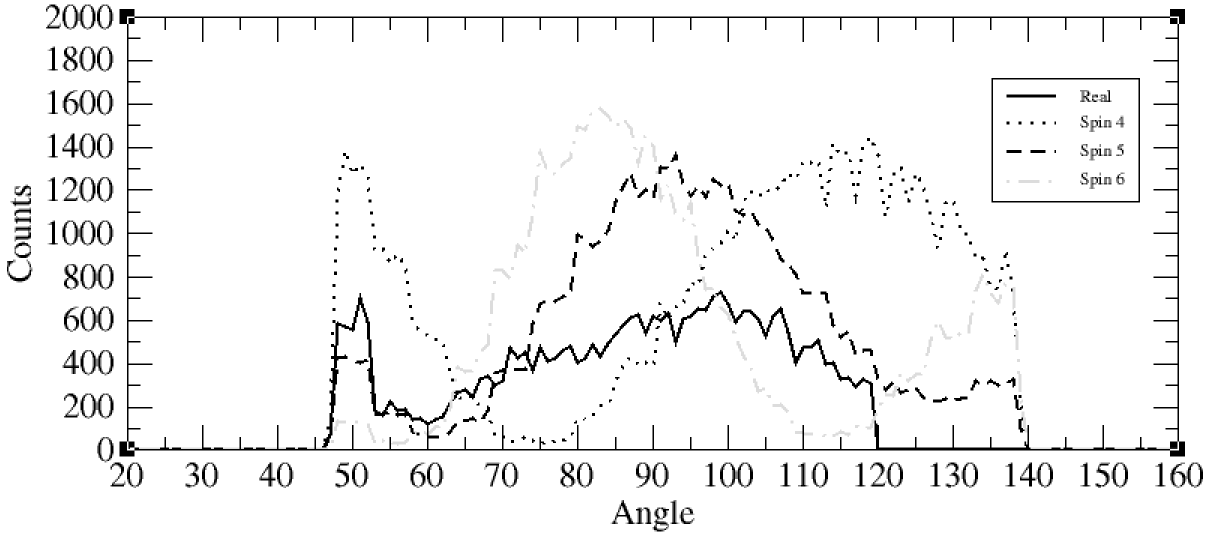

Figure 4.10: The comparison of the periodicity of the ^{4}He for the 18.80 MeV state. The figure compares the measured data against simulated data for spins 4,5 and 6. It appears that the spin 5 simulation fits the data the closest therefore this state was assigned a spin of 5

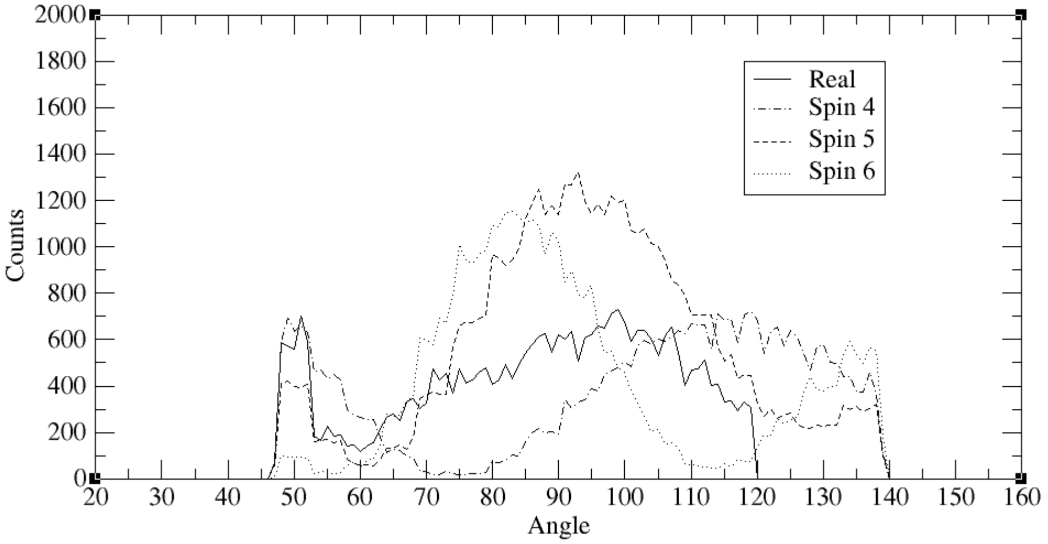

Figure 4.11: The comparison of the periodicity of the ^{4}He for the 19.76MeV state. The figure compares the measured data against simulated data for spins 4,5 and 6. Again it appears that this state is a spin 5 state.

Unfortunately this method of spin assignment can only be used on states that are well

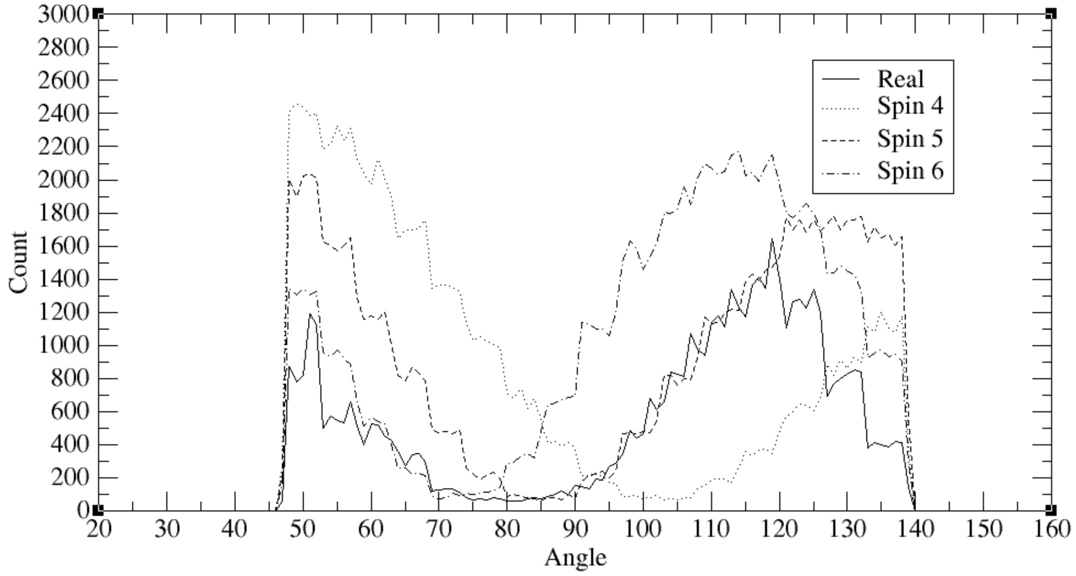

Figure 4.12: The comparison of the periodicity of the ^{4}He for the 20.66MeV state. The figure compares the measured data against simulated data for spins 4,5 and 6. Although slightly ambiguous, this state was determined to have a spin of 6.

defined singlets, cases in which there are isolated resonances. The interference from other states disturbs the periodicity making a clear comparison to simulated data extremely difficult. Due to this, only three of the states could have their spins identified uniquely using this method. As the ^{10}Be beam and the target ^{4}He are in their natural 0^{+} states it is assumed that the resultant states will be of natural parity. Table 4.2 shows the spins and assumed parities that were assigned by utilising the angular correlation method.

4.5 R-matrix Calculations

Using the spectral data obtained from the zero degree monitors and the spin assignments from the angular correlations an attempt was made to calculate additional information on the states in ^{14}C using the R-matrix method. To achieve this the software was programmed with information about the reaction. The reaction channel taking into account elastic reaction contributions to the spectrum was entered into the calculations. The information already gathered on the spectrum was input into the calculations and information on the

Table 4.2: Excited states of ^{14}C with spin assignments determined by angular correlations

Excitation Energy / MeV	Excitation Energy - Q-value / MeV	FWHM / MeV	Spin
14.54 ± 0.03	2.53	0.92 ± 0.08	
15.11 ± 0.02	3.10	1.98 ± 0.28	
15.35 ± 0.01	3.34	0.37 ± 0.07	
15.51 ± 0.04	3.50	0.36 ± 0.1	
15.91 ± 0.09	3.90	0.64 ± 0.22	
16.22 ± 0.01	4.21	0.75 ± 0.07	
17.50 ± 0.01	5.49	0.59 ± 0.04	
17.98 ± 0.03	5.97	1.23 ± 0.23	
18.80 ± 0.02	6.79	0.56 ± 0.04	
18.86 ± 0.003	6.85	0.48 ± 0.01	5^-
19.76 ± 0.01	7.75	0.37 ± 0.02	5^-
20.66 ± 0.01	8.65	0.37 ± 0.04	6^+

remaining states was estimated. The information estimated included the resonance energy, spin, parity, angular momentum and the reaction channel strength on the resonance.

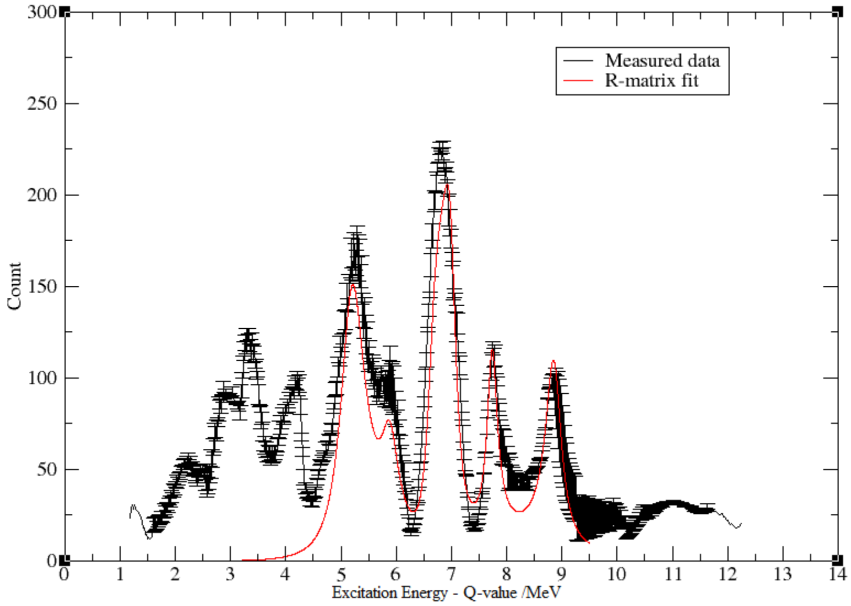

Figure 4.13: The black line represents the measured data in the spectrum of ^{14}C. The red line is a fit made using R-matrix calculations. The x-axis is the excitation energy minus the 12.011 Q-value.

Figure 4.13 is an example of a fit to the data created by the R-matrix calculations.

Table 4.3: Excited states of ^{14}C with additional spins found using R-matrix analysis.

Excitation Energy / MeV	Excitation Energy - Q-value / MeV	FWHM / MeV	Spin
14.54 ± 0.03	2.53	0.92 ± 0.08	
15.11 ± 0.02	3.10	1.98 ± 0.28	
15.35 ± 0.01	3.34	0.37 ± 0.07	
15.51 ± 0.04	3.50	0.36 ± 0.1	
15.91 ± 0.09	3.90	0.64 ± 0.22	
16.22 ± 0.01	4.21	0.75 ± 0.07	
17.50 ± 0.01	5.49	0.59 ± 0.04	(3^-)
17.98 ± 0.03	5.97	1.23 ± 0.23	(4^+)
18.80 ± 0.02	6.79	0.56 ± 0.04	
18.86 ± 0.003	6.85	0.48 ± 0.01	5^-
19.76 ± 0.01	7.75	0.37 ± 0.02	5^-
20.66 ± 0.01	8.65	0.37 ± 0.04	6^+

However, as there were only three states that had a predetermined spin assignment it was not possible to fully match the R-matrix spectrum to the data spectrum. There was not enough initial data to compensate for the multitude of unknown variables created by the large number of states. However it was possible to fit two more states using the R-matrix analysis, shown in Table 4.3.

4.6 Discussion

4.6.1 States in ^{14}C

The main purpose of the experiment was to ascertain if there were any molecular like rotational bands in ^{14}C. A plot of the energies of the excited states compared to J(J+1) was produced similar to that in Section 2.2. The results can be seen in Figure 4.14.

There were not enough data points to plot the two parity bands separately, therefore both were plotted together to provide an average. However, the results would still give an indication to the any characteristics of the molecular bands. The data were plotted in *xmgrace* where the slope of the graph provided a rotational parameter of 109 ± 2 keV.

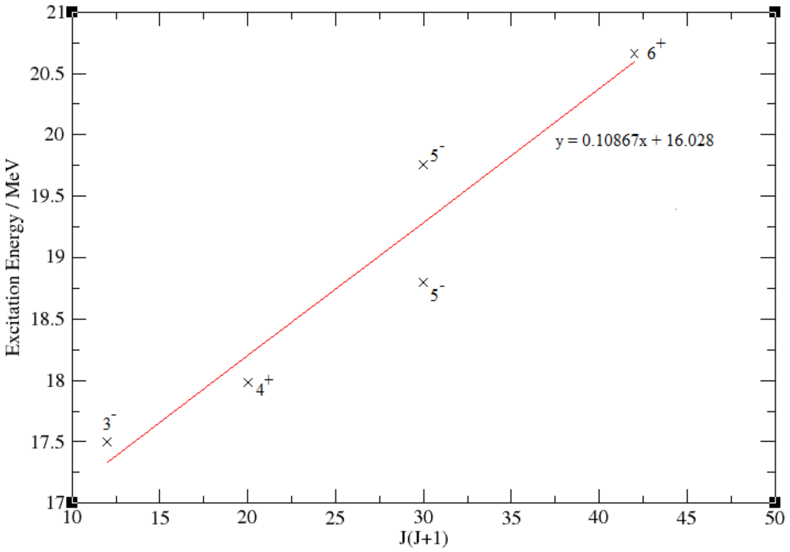

Figure 4.14: The five states that have been assigned a spin have been plotted on a graph comparing their energies with J(J+1). Here the data indicates a possible molecular band.

The intercept gives an indication of where the band-head is located, in this case 16.028 ± 0.24 MeV.

The classical calculations for two touching spheres of mass 10 and 4 are shown in Table 4.4. A range of calculations were performed for different values of r_0, the range of the nuclear force. We can see from this table that the calculated parameters are slightly higher than that of the measured data.

Table 4.4: The rotational parameters of two touching spheres of mass 10 and 4 at different ranges of the nuclear force.

r_0 (fm)	$\hbar^2/2I$ (keV)
1.2	231.9
1.3	197.6
1.4	170.3
1.5	148.4

However, if a slight gap is added between the two spherical masses the rotational parameters are reduced. Table 4.5 shows the calculated rotation parameters for two spheres, of mass 10 and mass 4, at a surface separation of 2 fm. Again the values have been calculated for a selection of nuclear force ranges. At a nuclear force range of $\mathrm{r}_0 =$ 1.4 the calculated rotational parameter $\hbar^2/2I = 107.7$ keV, almost exactly the same as the measured data.

Table 4.5: The rotational parameters of two spheres of mass 10 and 4 at different ranges of the nuclear force. Here the spheres are positioned 2 fm apart.

r_0 (fm)	$\hbar^2/2I$ (keV)
1.2	136.7
1.3	120.9
1.4	107.7
1.5	96.6

Furthermore, the parameters for the ^{14}C ground state, assuming a spherical nucleus, are shown in Table 4.6. At the same nuclear force range of 1.4 fm we see that the rotational parameter for the ground state is $\hbar^2/2I = 328$ keV. This is over three times that of the measured data indicating that the nucleus is exhibiting a very deformed structure.

Table 4.6: The rotational parameters for the ground state of ^{14}C, assuming a spherical nucleus. at different ranges of the nuclear force.

r_0 (fm)	$\hbar^2/2I$ (keV)
1.2	446.2
1.3	380.2
1.4	327.8
1.5	251.0

4.6.2 Comparison with previous work

Table 4.7 shows a comparison of data collected during this experiment with information gathered previously on states in ^{14}C. Here it is possible to see that some of the states discovered during this experiment correspond to states previously discovered. However, it is also possible to see that the characteristics of these states do not always agree. For this reason it would be prudent to continue examination of the ^{14}C.

Table 4.7: Energy levels above 11.66 MeV in ^{14}C which have been experimentally explored. The states final column of the table shows states which have been observed to α-decay. These have been compiled from measurements of ^{7}Li(^{9}Be,^{10}Be+α)[89], ^{14}C(^{13}C,^{10}Be+α)[90] and ^{14}C(^{14}C,^{10}Be+α)[91].

This Work		[92, 93]			2n Transfer [56]		^{13}C(p,n) [94]		^{9}Be(^{7}Li,d) [56]		States which α-decay [89, 90, 91, 95]	
E_x (MeV)	J^π	E_x (MeV)	J^π	Ref.	E_x (MeV)	J^π	E_x (MeV)	J^π	E_x (MeV)	J^π	E_x (MeV)	Ref.
		11.666	4^-	[93]	11.66	4^-	11.7	4^-	11.66	4^-		
		11.73	5^-	[93]	11.73	4^+			11.73	4^+		
		11.9(3)	(1^-)	[92]								
		12.20	1^-	[92]								
		12.61	2^-	[92]					12.58	(3^-)		
		12.863		[93]					12.86			
		12.963	(3^-)	[93]	12.96(4)	3^-	12.96		12.96			
		(13.50)		[93]								
		13.7	2^-	[92]	13.7(1)		13.56					
					14.0(1)				14.03		14.3(1)	[91]
14.54												
		14.63	(1^-)	[92]	14.67(5)	6^+			14.67	6^+		
		14.717	4^+	[92]								
		14.91	(1^+)	[92]	14.87(4)	5^-	14.87	5^-	14.87	5^-	14.8(1)	[89, 90, 91]
15.11												
		15.20	4^-	[93]					15.18	(5^-)		
15.35		(15.37)		[93]								
		15.44		[93]					15.40	(2^+)		
15.51		15.56	3^-	[92]							15.55(10)	[89, 91]
		15.8	(1^-)	[92]	15.75(8)							
15.91		15.91	4^+	[92]							15.9	[90]
		(16.02)		[93]								
16.22												
		16.43		[93]	16.4(1)	(6^+)			16.43	6^+	16.43(10)	[89, 90, 91]
		(16.57)		[93]					16.53	(2^+)		
		16.715	(1^+)	[93]	16.72(5)	(6^+)			16.72	(1^+)		
		17.30	4^-	[93]			17.3	4^-	17.30	4^-	17.3(1)	[91]
17.50	(3^-)	(17.5)	(1^+)	[93]	17.5(1)				17.52	(2^+)		
17.98	(4^+)	17.95		[93]					17.91	(2^+)		
		18.10		[93]					18.03	(7^-)	(18.1)	[91]
							18.53	(4^-)	18.39		18.5(1)	[89, 90]
					18.6(1)	4^-			18.60		18.6(1)	[91]
18.8												
18.86	5^-											
									19.14		(19.07(1))	[89, 90, 91]
											(19.3(1))	[91]
19.76	5^-				19.8(1)	2^+			19.73	(2^+)	19.83(1)	[89, 90, 91]
		20.4		[93]					20.02		(20.3(1))	[91]
20.66	6^+								20.75		20.6(1)	[89, 91]
									21.00			
					21.4(2)				21.41		21.43(1)	[89, 90, 91]
		22.1		[93]	22.5(3)						22.45(3)	[89, 91]
					23.5		23.2				(23.15(1))	[89, 91]
		24.3		[93]							24.0(3)	[89]
		24.5		[93]								

Chapter 5

Summary and Outlook

For a few decades now there has been a multitude of experimental and theoretical work performed on molecular-like nuclear structures, α-cluster cores with valence neutrons. Much of the experimental work on these molecular-like nuclear structures to date has focussed on the examination of neutron rich beryllium isotopes. So far, rotational bands have been identified in ^{9,10,11}Be. The search for molecular bands has recently shifted to the neutron rich carbon isotopes where multiple bands have been proposed. This thesis presents the results of an experiment designed to explore the excitation function of ^{14}C in an effort to provide information on resonant states potentially linked to molecular bands.

The ^{4}He(^{10}Be,^{10}Be)^{4}He reaction was used to explore the excitation function of ^{14}C. Twelve states were identified of which three could be given a spin assignment via angular correlation analysis. A further two states were assigned a spin after a R-matrix analysis was performed on the excitation function. The five states with spin assignments were compared and an energy versus J(J+1) plot was constructed. This plot indicated a molecular band with the nucleus deformed compared to the ground state.

5.1 Future Work

Current experiments have made progress in identifying and characterising states in ^{14}C. However it is clear that much more work is required to characterise the structure of all those states. In ^{14}C there have been some states which have been identified as strong candidates for molecular clusters. A lot of these states have had their partial widths determined and are only awaiting a spin assignment for definitive evidence of cluster structure. However, further experimentation is required to examine the low energy region of the excitation function produced in this work. This is required to resolve the resonances in the 13 to 16 MeV region and assign spins. However, the TTIK ^{4}He(^{10}Be,^{10}Be)^{4}He reaction would not be sufficient to resolve these resonances due to the broadening of the resonance caused by the thick target. An option would be to reverse the set-up, use a ^{4}He beam and a ^{10}Be target. Unfortunately ^{10}Be targets are very uncommon and this experiment would require many measurements and very small energy changes negating the purpose of using TTIK.

A further stage of experimentation would be to consider the heavier carbon isotopes to see if the molecular like structures persist. It would also be prudent to examine the heavier nuclei such as oxygen and neon. Measurements have already been made of neutron rich magnesium nuclei using the same TTIK methods, using a magnesium beam and a helium target.

Appendix A

Published Papers

This appendix contains a paper published detailing the work included in this thesis. The paper was published in the conference proceedings for the Rutherford Centennial Conference in Manchester 2011.

Study of states in ^{14}C via the ^{10}Be(^{4}He,^{4}He)^{10}Be reaction

J D Malcolm[1], M Freer[1], N I Ashwood[1], N Curtis[1], T Munoz-Britton[1], C Wheldon[1], V A Ziman[1], W N Catford[2], S Brown[2],G Wilson[2], N Soic[3], D Bardayan[4], S D Pain[4], N L Achouri[5], K Chipps[6] and K Crzywacz-Jones[7]

[1] School of Physics and Astronomy, University of Birmingham, Edgbaston, Birmingham, B15 2TT, UK
[2] School of Electronics and Physical Sciences, University of Surrey, Guildford, Surrey, GU2 7XH, UK
[3] Rudjer Boskovic Institute, Department of Experimental Physics, Bijenicka 54, HR-10000 Zagreb, Croatia
[4] Physics Division, Oak Ridge National Laboratory, Oak Ridge, Tennessee, USA
[5] Laboratoire de Physique Corpusculaire, ISMRA and Universite de Caen, IN2P3-CNRS, 14050 Caen Cedex, France
[6] Rutgers University, New Jersey, USA
[7] School of Physics and Astronomy, University of Tennessee, Knoxville, TN 37996, USA

E-mail: `jxm354@bham.ac.uk`

E-mail: `M.Freer@bham.ac.uk`

Abstract. A study of the ^{10}Be(^{4}He,^{4}He)^{10}Be reaction has been performed at ^{10}Be beam energies of 25.0, 27.0, 29.0, 32.0, 34.0, 38.0, 40.0, 42.0, 44.0 and 46.0 MeV. The measurements were to explore possible molecular rotational bands in ^{14}C. Three states at excitation energies of $E_x = 18.8$, 19.76 and 20.66 MeV have been measured and their spins have been determined to be 5^-, 5^- and 6^+, respectively.

1. Introduction

From previous work [1, 2] it is well known that ^{8}Be has a well defined α-α cluster structure. The ground state of ^{8}Be is, however, unbound as the α-α interaction is weak and the Pauli principle causes a repulsive core. The introduction of one more neutron into the system, to produce ^{9}Be, has the effect of adding enough binding energy to stabilise the system. In this case the neutron orbits the α cores in a delocalised region. Extending this system to add another neutron to create ^{10}Be produces a system where there are π and σ molecular bonds binding the core [3]. There is now strong evidence supporting the molecular α cluster structure in these isotopes [4, 5].

The same principles can be applied to carbon where the nucleus can be thought of as a three α particle configuration. In neutron-rich carbon nuclei, such as ^{13}C and ^{14}C, the valence neutrons reside in delocalised molecular orbits around the core. The extra neutrons again have the effect of increasing the binding energy and creating a more stable system. It is expected that there are three possible configurations of the nucleus in ^{14}C: a triangular configuration with the valence neutrons forming σ bonds between two of the α particles, a symmetrical linear configuration where the neutrons are spaced between the α particles (α-n-α-n-α) and an asymmetric configuration where both neutrons are between two α particles (α-$2n$-α-α). The final configuration should give rise to two rotational bands with opposite parity.

In an attempt to study the potential prolate and oblate molecular band nature of ^{14}C the spins and partial decay widths of resonances in ^{14}C were measured.

2. Experimental Details

The resonant scattering reaction ^{10}Be(^{4}He,^{4}He)^{10}Be was studied at beam energies of 25.0, 27.0, 29.0, 32.0, 34.0, 38.0, 40.0, 42.0, 44.0 and 46.0 MeV. This was performed at the Holyfield Radioactive Ion Beam Facility (HRIBF) at the Oak Ridge National Laboratory (ORNL), USA. In the experiment the ^{10}Be beam was incident on gaseous ^{4}He, which filled the reaction chamber at a pressure of 720 torr, providing a range of interaction energies as the beam was slowed by the gas. The gas was contained in the chamber by a 5 micron Havar window. The Q-value for the break-up of ^{14}C into the constituent isotopes, ^{10}Be and ^{4}He, is -12.011 MeV.

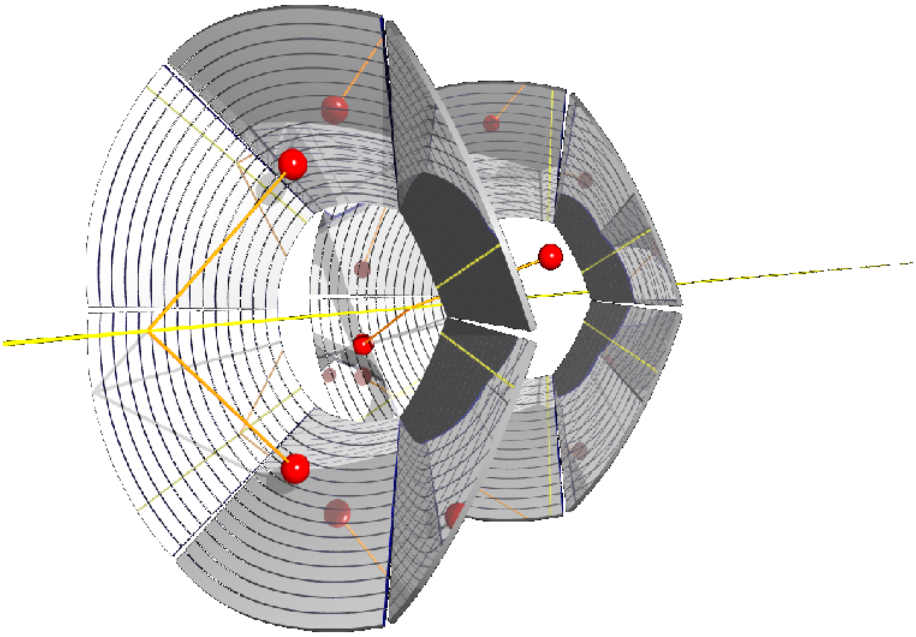

Figure 1. Schematic of the two 'lampshade' detectors.

Three sets of detectors were utilised in the experiment, two 'lampshade' detectors (shown in Fig. 1), each made from six silicon strip detectors, and a zero degree monitor. The lampshades were positioned 175 and 434 mm (to the back of the detectors) from the window with the silicon strips tilted at an angle of 46° to the beam axis. The twelve silicon strip detectors were 500 microns thick and segmented into 16 strips each, creating 96 channels per lampshade. For beam energies below 38 MeV the zero degree monitor consisted of two silicon surface barrier detectors (160 microns each) behind a 46 micron Mylar foil absorber. At 38 MeV and above the zero degree monitor was made from three surface barrier detectors (160 microns each) behind a 144 micron Mylar absorber. These were positioned 336 mm from the window.

The detectors were calibrated using α particles from ^{241}Am and ^{244}Cm, and the elastic scattering of the ^{10}Be beam from a gold target.

3. Analysis and Results

Calculations were made to correct for energy loss in the Havar window and energy loss of the beam as it traversed through the helium gas. The zero degree monitor was used for particle identification using E-ΔE. The energy deposited in the front detector is compared to that in the back detector, shown in Fig. 2, allowing the recoil ^{4}He to be identified.

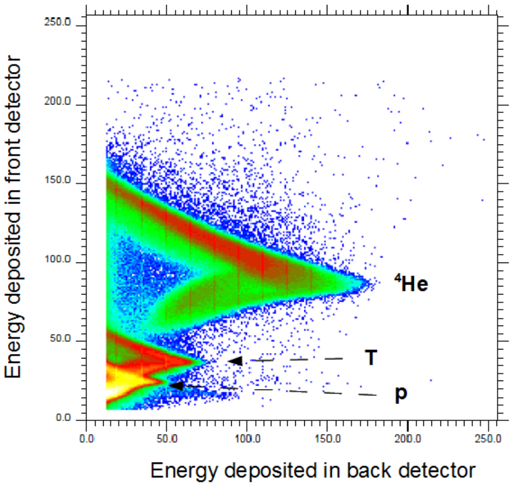

Figure 2. Particle identification plot for the zero degree monitors. Units are arbitrary

Using the monitor and correlating the data from the multiple beam energies a spectrum (Fig. 3) showing the states in ^{14}C can be constructed. The lampshade detectors were used to determine the spins of the states identified by the zero degree monitors. Both the ^{4}He and the ^{10}Be particles were detected by the lampshades in opposite silicon detectors.

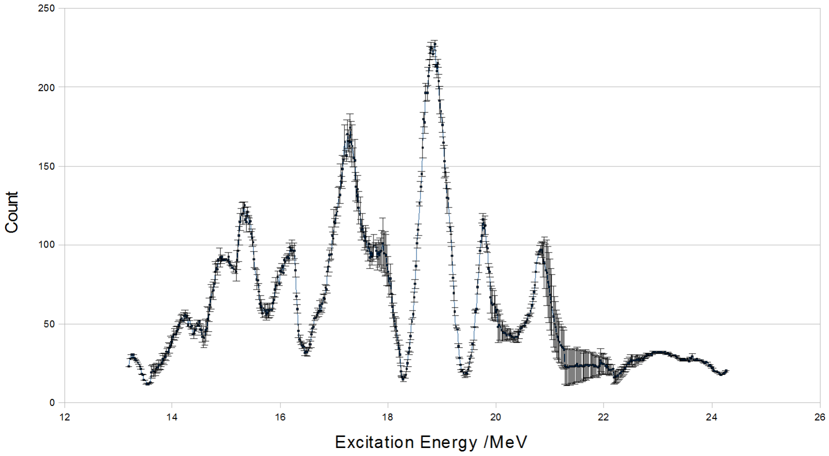

Figure 3. Normalised excitation energy spectrum of ^{14}C from the zero degree monitors.

The energy deposited in a detector was plotted against the angle to produce a two dimensional plot shown in Fig. 4. Resonances appear on the plot periodically along a line as shown in the figure. Once the resonance had been identified its spin was determined by comparing the periodicity of the data with simulated data. A range of spins were compared with the resonances shown in the two dimensional plots until a match was acquired.

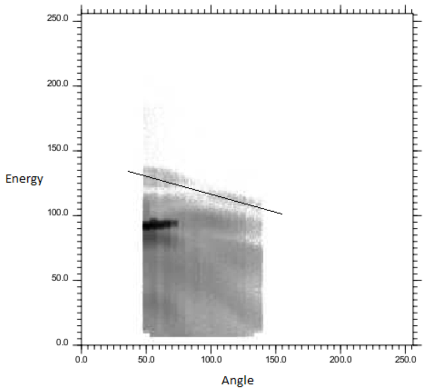

Figure 4. Real data from the lampshade detectors. Units are arbitrary

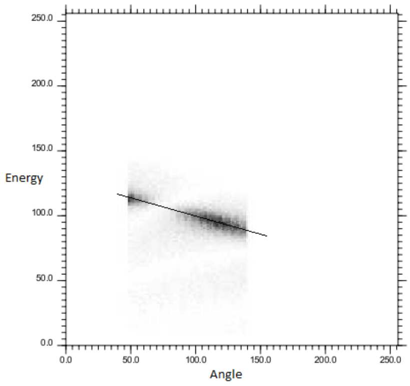

Figure 5. Simulated data for the lampshades. Units are arbitrary.

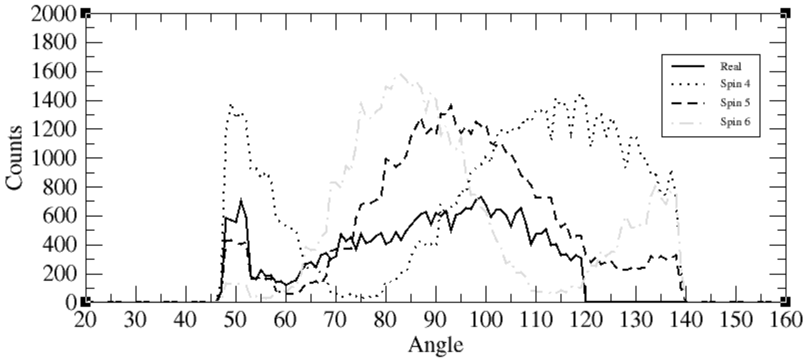

Figure 6. Comparison of real data with simulated data of different spins.

Fig. 6 is an example of the comparison process that each of the resonances underwent. As spin is increased the periodicity of the angular distribution is also increased. By matching the periodicity of the real data to that of the simulated data allowed for identification of the spin of the states. Via this method three of the resonances determined in the spectrum of ^{14}C could have their spins identified. These are the resonances at excitation energies, E = 18.8, 19.76 and 20.66 MeV which have spins of 5^-, 5^- and 6^+ respectively.

4. Summary and Future Work

The ^{10}Be(^{4}He,^{4}He)^{10}Be reaction has been studied at various ^{10}Be beam energies ranging from 25 to 46 MeV. A spectrum showing clear energy states in ^{14}C has been created and the spins of some of those states has been determined. The unknown spins of the other resonances shown in Fig. 3 will be calculated using R-Matrix analysis. Once the spins of the states have been deduced possible rotational bands may become evident.

References

[1] Buck B, Friedrich H and Wheatley C 1977 *Nucl. Phys.* A **275** 246

[2] Hiura J and Tamagaki R 1972 *Suppl. Prog. Theor. Phys.* **52** 25

[3] Kanada-En'yo Y, Horiuchi H and Dote A 1999 *Phys. Rev.* C **60** 064304

[4] von Oertzen W 1997 *Z. Phys.* A **357** 355

[5] Freer M *et al* 1999 *Phys. Rev. Lett.* **82** 1383

List of References

[1] M. Freer, H. Fujita, Z. Buthelezi, J. Carter, R. W. Fearick, S. V. Förtsch, R. Neveling, S. M. Perez, P. Papka, F. D. Smit, J. A. Swartz, and I. Usman. 2^+ excitation of the ^{12}C hoyle state. *Phys. Rev. C*, 80:041303, 2009.

[2] J. J. Thomson. Cathode Rays. *Phil. Mag.*, (44):293, 1897.

[3] E. Rutherford. The Scattering of α and β Particles by Matter and the Structure of the Atom. *Phil. Mag.*, (21):669–688, 1911.

[4] J. Chadwick. The Existence of a Neutron. *Proc. Roy. Soc. Lond. A*, A(136):692–708, 1932.

[5] H. A. Bethe and R. F Bacher. Nuclear Physics A. Stationary States of Nuclei. *Rev. Mod. Phys.*, (8):82–229, 1936.

[6] H. A. Bethe. Nuclear Physics B. Nuclear Dynamics, Theoretical. *Rev. Mod. Phys.*, (9):69, 1937.

[7] J. A. Wheeler. Molecular Viewpoints in Nuclear Structure. *Phys. Rev.*, (52):1083–1106, 1937.

[8] J. A. Wheeler. On the Mathematical Description of Light Nuclei by the Method of Resonating Group Structure. *Phys. Rev.*, (52):1107–1122, 1937.

[9] L. R. Hafstad and E. Teller. The Alpha-Particle Model of the Nucleus. *Phys. Rev.*, (54):681–692, 1938.

[10] D. M. Dennison. Excited States of the O^{16} Nucleus. *Phys. Rev.*, (57):454–456, 1940.

[11] G. Gamow. *Proc. Roy. Soc. A*, (126):632, 1930.

[12] G. Gamow. *Contitution of Atomic Nuclei and Radioactivity.* Oxford University Press, 1931.

[13] K. S. Krane. *Introductory Nuclear Physics.* John Wiley and Sons, Inc., 1988.

[14] M. Freer. The clustered nucleus, cluster structures in stable and unstable nuclei. *Reports on Progress in Physics*, 70(12):2149, 2007.

[15] Noboru Takigawa Kiyomi Ikeda and Hisashi Horiuchi. The systematic structure-change into the molecule-like structures in the self-conjugate 4n nuclei. *Prog. Theor. Phys. Suppl.*, E68:464–475, 1968.

[16] Kiyomi Ikeda, Noboru Takigawa, and Hisashi Horiuchi. The Systematic Structure-Change into the Molecule-like Structures in the Self-Conjugate $4n$ Nuclei. *Progress of Theoretical Physics Supplement*, E68:464–475, 1968.

[17] Tz. Kokalova, 2012. Private communication.

[18] K. A. Erb, R. R. Betts, S. K. Korotky, M. M. Hindi, P. P. Tung, M. W. Sachs, S. J. Willett, and D. A. Bromley. Resonant and average behavior of the ^{12}C+^{12}C total reaction cross section: $5.6 \leqslant E_{c.m.} \leqslant 10.0$ MeV. *Phys. Rev. C*, 22:507–514, 1980.

[19] K. Nagatani, T. Shimoda, D. Tanner, R. Tribble, and T. Yamaya. Reaction ^{12}C(^{16}O, α)^{24}Mg leading to nuclear molecular resonances. *Phys. Rev. Lett.*, 43:1480–1482, 1979.

[20] T. M. Cormier. Resonances in Heavy-Ion Nuclear Reactions. *Annual Review of Nuclear and Particle Science*, 32(1):271–306, 1982.

[21] N. Curtis, N. M. Clarke, B. R. Fulton, S. J. Hall, M. J. Leddy, A. St. J. Murphy, J. S. Pople, R. P. Ward, W. N. Catford, G. J. Gyapong, S. M. Singer, S. P. G. Chappell, S. P. Fox, C. D. Jones, D. L. Watson, W. D. M. Rae, and P. M. Simmons. Association of the ^{12}C+^{12}c breakup states in ^{24}Mg with the quasimolecular resonances. *Phys. Rev. C*, 51:1554–1557, 1995.

[22] Sven Gsta Nilsson, Chin Fu Tsang, Adam Sobiczewski, Zdzislaw Szymanski, Slawomir Wycech, Christer Gustafson, Inger-Lena Lamm, Peter Mller, and Bjrn Nilsson. On the nuclear structure and stability of heavy and superheavy elements. *Nuclear Physics A*, 131(1):1 – 66, 1969.

[23] S Marsh and W. D. M. Rae. The Structure of ^{24}Mg Using the Cranked Cluster Model. *Phys. Lett. B*, 180:185–190, 1986.

[24] G. Leander and S.E. Larsson. Potential-energy surfaces for the doubly even n = z nuclei. *Nuclear Physics A*, 239(1):93 – 113, 1975.

[25] D.M. Brink. Course 36. In C.L. Bloch, editor, *Proc. Int. School of Physics Enrico Fermi (Varenna, 1965)*, page 247. New York: Academic, 1966.

[26] B R Fulton and W D M Rae. Fission of light nuclei. *Journal of Physics G: Nuclear and Particle Physics*, 16(3):333, 1990.

[27] J Cseh and W Scheid. On the relation between cluster and superdeformed states of light nuclei. *Journal of Physics G: Nuclear and Particle Physics*, 18(8):1419, 1992.

[28] Cindro, N. Resonances and nuclear molecular configurations in heavy-ion reactions. *Ann. Phys. Fr.*, 13(4):289–324, 1988.

[29] N. I. Ashwood, J. T. Murgatroyd, N. M. Clarke, M. Freer, B. R. Fulton, A. St. J. Murphy, S. P. G. Chappell, R. L. Cowin, G. K. Dillon, D. L. Watson, W. N. Catford, N. Curtis, M. Shawcross, and V. Pucknell. Evidence for a highly deformed band in ^{12}C+^{16}O breakup of ^{28}Si. *Phys. Rev. C*, 63:034315, 2001.

[30] C J Metelko, M Freer, N Curtis, J T Murgatroyd, S M Singer, D J Henderson, D J Hofman, and A H Wuosmaa. Resonances in ^{28}Si populated in the ^{12}C(^{20}Ne,^{28}Si*)α reaction. *Journal of Physics G: Nuclear and Particle Physics*, 29(4):697, 2003.

[31] N. Curtis, A. St. J. Murphy, N. M. Clarke, M. Freer, B. R. Fulton, S. J. Hall, M. J. Leddy, J. S. Pople, G. Tungate, R. P. Ward, W. N. Catford, G. J. Gyapong, S. M. Singer, S. P. G. Chappell, S. P. Fox, C. D. Jones, D. L. Watson, W. D. M. Rae, P. M. Simmons, and P. H. Regan. Evidence for a highly deformed band in ^{16}O+^{16}O breakup of ^{32}S. *Phys. Rev. C*, 53:1804–1810, 1996.

[32] Jun Hiura and Ryozo Tamagaki. Chapter ii. typical realization of alpha-particle model aspects in beryllium region. *Progress of Theoretical Physics Supplement*, 52:25–88, 1972.

[33] B. Buck, H. Friedrich, and C. Wheatley. Local potential models for the scattering of complex nuclei. *Nuclear Physics A*, 275(1):246 – 268, 1977.

[34] F. Hoyle. Nuclear reactions occurring in very hot stars. i. the synthesis of elements from carbon to nickel. *Astrophys. J. (Suppl.)*, 1:121–46, 1954.

[35] M. Freer, S. Almaraz-Calderon, A. Aprahamian, N. I. Ashwood, M. Barr, B. Bucher, P. Copp, M. Couder, N. Curtis, X. Fang, F. Jung, S. Lesher, W. Lu, J. D. Malcolm, A. Roberts, W. P. Tan, C. Wheldon, and V. A. Ziman. Evidence for a new ^{12}C state at 13.3 mev. *Phys. Rev. C*, 83:034314, 2011.

[36] P. Chevallier, F. Scheibling, G. Goldring, I. Plesser, and M. W. Sachs. Breakup of ^{16}O into ^{8}Be+^{8}Be. *Phys. Rev.*, 160:827–834, 1967.

[37] F. Brochard, P. Chevallier, D. Disdier, V. Rauch, G. Rudolf, and F. Scheibling. ^{12}C(α,^{8}Be)^{8}Be reaction in the energy range $E_\alpha = 17-33$ mev. *Phys. Rev. C*, 13:967–975, 1976.

[38] Sven Aberg, Ingemar Ragnarsson, Tord Bengtsson, and Raymond K. Sheline. A unified approach to particle-holes and rotations in the spectrum of ^{16}O. *Nuclear Physics A*, 391(2):327 – 349, 1982.

[39] W. Bauhoff, H. Schultheis, and R. Schultheis. Alpha cluster model and the spectrum of ^{16}O. *Phys. Rev. C*, 29:1046–1055, 1984.

[40] T. Tomoda and A. Arima. Coexistence of shell structure and cluster structure in ^{20}Ne. *Nuclear Physics A*, 303(12):217 – 253, 1978.

[41] M. M. Hindi, J. H. Thomas, D. C. Radford, and P. D. Parker. Cluster structure of 8p-4h states in ^{20}Ne. *Phys. Rev. C*, 27:2902–2922, 1983.

[42] W. von Oertzen, Martin Freer, and Yoshiko Kanada-Enyo. Nuclear clusters and nuclear molecules. *Physics Reports*, 432(2):43 – 113, 2006.

[43] M. Freer, R.R. Betts, and A.H. Wuosmaa. Relationship between the deformed harmonic oscillator and clustering in light nuclei. *Nuclear Physics A*, 587(1):36 – 54, 1995.

[44] W. D. M. Rae. Clustering phenomena and shell effects in nuclear structure and reactions. *Itn. J. Mod. Phys. A*, 3(6):1343–1372, 1988.

[45] Martin Freer. Molecules in nuclei. *Comptes Rendus Physique*, 4(45):475 – 487, 2003.

[46] P McEwan and M Freer. Characterization of molecular structures in the deformed harmonic oscillator. *Journal of Physics G: Nuclear and Particle Physics*, 30(4):447, 2004.

[47] N. Itagaki and S. Okabe. Molecular orbital structures in ^{10}Be. *Phys. Rev. C*, 61:044306, 2000.

[48] N. Itagaki, S. Hirose, T. Otsuka, S. Okabe, and K. Ikeda. Triaxial deformation in ^{10}Be. *Phys. Rev. C*, 65:044302, 2002.

[49] N. Itagaki and K. Hagino. Low-energy photodisintegration of ^{9}Be with the molecular orbit model. *Phys. Rev. C*, 66:057301, 2002.

[50] N. Itagaki, S. Okabe, K. Ikeda, and I. Tanihata. Molecular-orbital structure in neutron-rich c isotopes. *Phys. Rev. C*, 64:014301, 2001.

[51] N. Itagaki, W. von Oertzen, and S. Okabe. Linear-chain structure of three α clusters in ^{13}C. *Phys. Rev. C*, 74:067304, 2006.

[52] N. Itagaki, T. Otsuka, K. Ikeda, and S. Okabe. Equilateral-triangular shape in ^{14}C. *Phys. Rev. Lett.*, 92:142501, 2004.

[53] Yoshiko Kanada-En'yo and Hisashi Horiuchi. Structure of light unstable nuclei studied with antisymmetrized molecular dynamics. *Progress of Theoretical Physics Supplement*, 142:205–263, 2001.

[54] Y Kanada-En'yo, H Horiuchi, and A Dot. Structure of excited states of unstable nuclei studied with antisymmetrized molecular dynamics. *Journal of Physics G: Nuclear and Particle Physics*, 24(8):1499, 1998.

[55] Y. Kanada-En'yo, H. Horiuchi, and A. Doté. Structure of excited states of ^{10}Be studied with antisymmetrized molecular dynamics. *Phys. Rev. C*, 60:064304, 1999.

[56] W. von Oertzen, H. G. Bohlen, M. Milin, Tz Kokalova, S. Thummerer, A. Tumino, R. Kalpakchieva, T. N. Massey, Y. Eisermann, G. Graw, T. Faestermann, R. Hertenberger, and H.-F. Wirth. Search for cluster structure of excited states in ^{14}C. *The European Physical Journal A - Hadrons and Nuclei*, 21:193–215, 2004.

[57] M. Milin and W. von Oertzen. Search for molecular bands in ^{13}C. *The European Physical Journal A - Hadrons and Nuclei*, 14:295–307, 2002.

[58] W. Galati, J. D. Brandenberger, and J. L. Weil. Scattering of neutrons by carbon from 3 to 7 mev. *Phys. Rev. C*, 5:1508–1529, 1972.

[59] F. Hinterberger, G. Mairle, U. Schmidt-Rohr, P. Turek, and G.J. Wagner. Single nucleon pick-up from 12c and 14n with 52 mev deuterons. *Nuclear Physics A*, 106(1):161 – 176, 1967.

[60] Donald G. Fleming, Joseph Cerny, Creve C. Maples, and Norman K. Glendenning. ^{15}N(p, t)^{13}N and ^{15}N(p, ^{3}He)^{13}C reactions and the spectroscopy of levels in mass 13. *Phys. Rev.*, 166:1012–1029, 1968.

[61] H. Ohnuma, N. Hoshino, O. Mikoshiba, K. Raywood, A. Sakaguchi, G.G. Shute, B.M. Spicer, M.H. Tanaka, M. Tanifuji, T. Terasawa, and M. Yasue. The ^{12}C(d, p)^{13}C reaction at E_d = 30MeV and positive-parity states in ^{13}C. *Nuclear Physics A*, 448(2):205 – 220, 1986.

[62] M. Yasue, M.H. Tanaka, T. Hasegawa, K. Nisimura, H. Ohnuma, H. Shimizu, K. Ieki, H. Toyokawa, M. Iwase, J. Iimura, H. Yoshida, T. Nakagawa, A. Sato, T. Niizeki, J. Takamatsu, Y. Takahashi, T. Tohei, H. Orihara, T. Suehiro, S.I. Hayakawa, K. Ogawa, M. Igarashi, and R.J. Peterson. Structure of ^{14}C studied by the ^{14}C(p,d)^{13}C reaction. *Nuclear Physics A*, 509(1):141 – 160, 1990.

[63] Charles H. Holbrow, H. G. Bingham, R. Middleton, and J. D. Garrett. Identification of analog pairs in ^{13}C and ^{13}N by means of the ^{10}B(^{6}Li, ^{3}He)^{13}C and ^{10}B(^{6}Li, t)^{13}N reactions. *Phys. Rev. C*, 9:902–909, 1974.

[64] C. Meynadier, J.F. Allard, M. Amiel, H. Beaumevieille, B. Chambon, and C. Morand. Etude des reactions ^{11}B(^{3}He, p)^{13}C et ^{20}Ne(^{3}He, p)^{22}Na A $E_{^3He} \leq 3$ MeV. *Nuclear Physics A*, 161(1):305 – 320, 1971.

[65] R.R. Wu, R.L. Dangle, M.M. Duncan, J.L. Duggan, P.D. Miller, and Lin Jung. A study of the ^{11}B(^{3}He, p)^{13}C reaction at 12, 10, 8, 6 and 4 MeV. *Nuclear Physics A*, 199(1):23 – 30, 1973.

[66] J. A. Macdonald, Joseph Cerny, J. C. Hardy, H. L. Harney, A. D. Bacher, and G. R. Plattner. Analyzing powers for two-nucleon transfer reactions in the 1p shell. *Phys. Rev. C*, 9:1694–1704, 1974.

[67] J. D. Brown, E. R. Jacobsen, and K. W. Kemper. Search for a 21.4-MeV state in ^{13}C and (p,π^+) production mechanisms. *Phys. Rev. C*, 44:2581–2583, 1991.

[68] X. Aslanoglou, K. W. Kemper, P. C. Farina, and D. E. Trcka. Location of major α strength in ^{13}C at 10.75 mev. *Phys. Rev. C*, 40:73–76, 1989.

[69] F. D. Snyder and M. A. Waggoner. Study of ^{9}Be(^{7}Li,p), ^{9}Be(^{7}Li,d), ^{9}Be(^{7}Li,t), and ^{9}Be(^{7}Li,α) reactions from 5.6 to 6.2 MeV. *Phys. Rev.*, 186:999–1012, 1969.

[70] D. Kurath. Alpha-structure amplitudes for the 1p shell. *Phys. Rev. C*, 7:1390–1395, 1973.

[71] S.F. Collins, G.G. Shute, B.M. Spicer, V.C. Officer, I. Morrison, K.A. Amos, D.W. Devins, D.L. Friesel, and W.P. Jones. A study of the ^{13}C(p, p') reactions at 135 MeV. *Nuclear Physics A*, 380(3):445 – 464, 1982.

[72] S.F. Collins, G.G. Shute, B.M. Spicer, V.C. Officer, D.W. Devins, D.L. Friesel, and W.P. Jones. The spectroscopy of ^{13}C by inelastic proton scattering. *Nuclear Physics A*, 481(3):494 – 530, 1988.

[73] D. J. Millener, D. I. Sober, H. Crannell, J. T. O'Brien, L. W. Fagg, S. Kowalski, C. F. Williamson, and L. Lapikás. Inelastic electron scattering from ^{13}C. *Phys. Rev. C*, 39:14–46, 1989.

[74] G. Wittwer, H.G. Clerc, and G.A. Beer. Properties of electromagnetic transitions in ^{13}C. *Physics Letters B*, 30(9):634 – 636, 1969.

[75] R. J. Peterson, J. R. Shepard, and R. A. Emigh. Isoscalar and isovector transition amplitudes in A=13. *Phys. Rev. C*, 24:826–840, 1981.

[76] C. Lee, D. D. Caussyn, N. R. Fletcher, D. L. Gay, M. B. Hopson, J. A. Liendo, S. H. Myers, M. A. Tiede, and J. W. Baker. α-particle decay of states in ^{11}C, ^{13}C, and ^{15}N near decay threshold. *Phys. Rev. C*, 58:1005–1012, 1998.

[77] K.P. Artemov. Effective method of study of α-cluster states. *Sov. J. Nucl. Phys*, 52:408, 1990.

[78] V. Z. Goldberg, G. V. Rogachev, W. H. Trzaska, J. J. Kolata, A. Andreyev, C. Angulo, M. J. G. Borge, S. Cherubini, G. Chubarian, G. Crowley, P. Van Duppen, M. Gorska, M. Gulino, M. Huyse, P. Jesinger, K.-M. Källman, M. Lattuada, T. Lönnroth, M. Mutterer, R. Raabe, S. Romano, M. V. Rozhkov, B. B. Skorodumov, C. Spitaleri, O. Tengblad, and A. Tumino. Investigation of the α-cluster structure of ^{22}Ne and ^{22}Mg. *Phys. Rev. C*, 69:024602, 2004.

[79] N. M. Clarke. Computer Code dedx. unpublished.

[80] A. M. Lane and R. G. Thomas. R-matrix theory of nuclear reactions. *Rev. Mod. Phys.*, 30:257–353, 1958.

[81] G. Breit and E. Wigner. Capture of slow neutrons. *Phys. Rev.*, 49:519–531, 1936.

[82] http://www.phy.ornl.gov/hribf/.

[83] http://www.phy.ornl.gov/hribf/accelerator/fac-layout.shtml.

[84] N Curtis, 2012. Private communication.

[85] A. Galindo-Uribarri, J.R. Beene, M. Danchev, J. Doup, B. Fuentes, J. Gomez del Campo, P.A. Hausladen, R.C. Juras, J.F. Liang, A.E. Litherland, Y. Liu, M.J. Meigs, G.D. Mills, P.E. Mueller, E. Padilla-Rodal, J. Pavan, J.W. Sinclair, and D.W. Stracener. Pushing the limits of accelerator mass spectrometry. *Nuclear Instruments and Methods in Physics Research Section B: Beam Interactions with Materials and Atoms*, 259(1):123 – 130, 2007. Accelerator Mass Spectrometry;Proceedings of the Tenth International Conference on Accelerator Mass Spectrometry.

[86] http://www.phy.ornl.gov/hribf/equipment/sidar/.

[87] S. J. Bennett and S. J. Hall. Computer Code SUNSORT. unpublished.

[88] O.B. Tarasov and D. Bazin. Lise++: Radioactive beam production with in-flight separators. *Nuclear Instruments and Methods B*, 266:4657–4664, 2008.

[89] N. Soić, M. Freer, L. Donadille, N. M. Clarke, P. J. Leask, W. N. Catford, K. L. Jones, D. Mahboub, B. R. Fulton, B. J. Greenhalgh, D. L. Watson, and D. C. Weisser. ^{4}He decay of excited states in ^{14}C. *Phys. Rev. C*, 68:014321, 2003.

[90] D.L. Price, M. Freer, S. Ahmed, N.I. Ashwood, N.M. Clarke, N. Curtis, P. McEwan, C.J. Metelko, B. Novatski, S. Sakuta, N. Soic, D. Stepanov, and V. Ziman. Alpha-decay of excited states in 13c and 14c. *Nuclear Physics A*, 765(34):263 – 276, 2006.

[91] D. L. Price, M. Freer, N. I. Ashwood, N. M. Clarke, N. Curtis, L. Giot, V. Lima, P. Mc Ewan, B. Novatski, N. A. Orr, S. Sakuta, J. A. Scarpaci, D. Stepanov, and V. Ziman. α decay of excited states in ^{14}C. *Phys. Rev. C*, 75:014305, 2007.

[92] D. A. Resler, H. D. Knox, P. E. Koehler, R. O. Lane, and G. F. Auchampaugh. Structure of ^{14}C via elastic and inelastic neutron scattering from ^{13}C: Measurement and R -matrix analysis. *Phys. Rev. C*, 39:766–782, 1989.

[93] F. Ajzenberg-Selove. Energy levels of light nuclei A = 13–15. *Nuclear Physics A*, 523(1):1 – 196, 1991.

[94] E. Korkmaz, S. E. Vigdor, W. W. Jacobs, T. G. Throwe, L. C. Bland, M. C. Green, P. L. Jolivette, and J. D. Brown. ^{12}C(p$\rightarrow$, $\pi^{\pm}$) reactions at T_p=200 Mev. *Phys. Rev. C*, 40:813–831, 1989.

[95] P. J. Haigh, N. I. Ashwood, T. Bloxham, N. Curtis, M. Freer, P. McEwan, D. Price, V. Ziman, H. G. Bohlen, Tz. Kokalova, Ch. Schulz, R. Torabi, W. von Oertzen, C. Wheldon, W. Catford, C. Harlin, R. Kalpakchieva, and T. N. Massey. Measurement of α and neutron decay widths of excited states of ^{14}C. *Phys. Rev. C*, 78:014319, 2008.